Drying and Wetting of Capillary Porous Materials: Insights from Imaging and Physics-based Modeling

Habilitationsschrift

von Dr.-Ing. Abdolreza Kharaghani

geb. am 23. August 1980 in Teheran

zur Verleihung des akademischen Grades

Doktor-Ingenieur habilitatus
(Dr.-Ing. habil.)

genehmigt von der Fakultät für Verfahrens- und Systemtechnik
der Otto-von-Guericke-Universität Magdeburg am 05. Februar 2020

Gutachter:

Prof. Dr.-Ing. habil. Evangelos Tsotsas	Otto-von-Guericke-Universität Magdeburg
Prof. Majid Hassanizadeh	Utrecht University
Prof. Dr.-Ing. habil. Stefan Heinrich	Hamburg University of Technology

Acknowledgment

This habilitation thesis covers a major part of my academic work at the Chair of Thermal Process Engineering at Otto-von-Guericke University Magdeburg. I would like to acknowledge a couple of people who made this work possible:

I would like to express my sincere gratitude to Prof. Evangelos Tsotsas for giving me the opportunity to continue the research activity on pore network modeling. His persistent support has significantly contributed to develop this field.

I would like to thank Prof. Majid Hassanizadeh and Prof. Stephan Heinrich for agreeing to review and evaluate this work.

Additional thanks go to the pore network modeling team members, both former (MSc. Yujing Wang, Dr.-Ing. Yu Sun, Dr. Rui Wu, Dr.-Ing. Alireza Attari Moghaddam, Dr.-Ing. Kieu Hiep Le, and MSc. Yasaman Jabbari) and present (MSc. Arman Rahimi, MSc. Thai Son Pham, MSc. Xiang Lu and MSc. Faeez Ahmad, MSc. Hafiz Tariq Mahmood). It was, and still is, a pleasure to work with you guys and to explore together the amazing and challenging field of pore network modeling. I would especially like to thank Dr.-Ing. habil. Thomas Metzger for his contributions to the development of our basic pore network models. I would also like to thank Prof. Marc Prat and Dr. Christoph Kirsch for their continuous scientific collaborations with us.

Our several research projects have been financed as a part of the graduate school on Micro-Macro-Interactions in Structured Media and Particulate Systems sponsored generously by German Research Foundation (DFG). I would like to express my sincere gratitude to DFG for financial aid. Furthermore, I would like to extend my thanks to Alexander von Humboldt Foundation as well as our industrial collaborators for their financial support.

Finally, I would like to thank my mother and my family, who have supported and encouraged me in many crucial situations, right up to this degree.

Zusammenfassung

Ziel dieser Habilitationsschrift ist es, die konvektive Trocknung von kapillarporösen Materialien grundlegend zu untersuchen. Darüber hinaus sollen einige wichtige Aspekte behandelt werden, die für den Benetzungsprozess und die Zweiphasenströmung ohne Phasenübergänge (d.h. Drainage und Imbibition) in solchen Materialien relevant sind. Für diese Untersuchungen wurden verschiedene experimentelle Techniken sowie diskrete und kontinuierliche Modellierungsansätze angewendet.

Die optische Visualisierung wird eingesetzt, um die Eigenschaften des Trocknungsprozesses in einfachen und doppelten Hele-Shaw-Zellen zu messen. Beide Zelltypen bestehen aus einer einzigen Schicht monodisperser kugelförmiger Glaskugeln, die zwischen transparenten Glasplatten eingelagert sind. Im Gegensatz zu den Einzelzellen bestehen die Doppelzellen aus zwei miteinander verbundenen Bereichen, die mit kleinen und großen, hydrophilen und hydrophoben, getrennten und gesinterten Partikeln gefüllt sind. Alle Zellen sind mit destilliertem Wasser gesättigt und werden bei Raumtemperatur getrocknet. Basierend auf zweidimensionalen optischen Bildern werden die Nass- und Trockenbereiche bestimmt. Die zeitliche Entwicklung dieser Regionen zeigt deutlich, wie Kapillareffekte von der Porenstruktur, der Benetzbarkeit der festen Oberfläche und der mittleren Heterogenität abhängen.

Die Flüssigkeitseindringung und Phasenverteilung in transparenten Mikromodellen wird in Echtzeit durch optische Fotografie untersucht. Die Mikromodelle sind quasi-zweidimensionale Netzwerke aus Polydimethylsiloxan (PDMS) oder Silikon. Die PDMS-Mikromodelle werden fr Trocknungs- und Zweiphasenströmungsexperimente verwendet, während die Silikon-Netzwerke für Benetzungsmessungen eingesetzt werden. Aus diesen Experimenten wurden wichtige physikalische Effekte (z.B. der sogenannte kapillare Ventileffekt) erkannt, die dann in Porennetzmodelle integriert wurden. Die Übereinstimmung zwischen Porennetzwerksimulationen und Mikromodellmessungen ist besser, wenn der kapillare Ventileffekt in den Modellen berücksichtigt wird.

Trocknungsversuche mit zufälligen Packungen monodisperser kugelförmiger Partikel wurden mithilfe von mikrotomographischen Röntgenaufnahmen in situ durchgeführt. Die Schüttgutbetten sind mit getrennten oder gesinterten Glaskugeln gefüllt und entweder mit destilliertem Wasser oder mit einer Salzlösung gesättigt. Die dreidimensionale Entwicklung der Flüssigkeitsverteilung über die Zeit wird durch eine Reihe von Momentaufnahmen vom Beginn des Trocknungsprozesses bis zum Ende visualisiert. Auf dieser Grundlage werden fast alle Details der Struktur der flüssigen Phase in der Packung aufgezeigt. Es wird beobachtet, dass bei geringer Sättigung die flüssige Phase über ein Netzwerk von Flüssigkeitsringen, die an den Kontaktstellen zwi-

schen den Partikeln gebildet werden, mit der Packungsoberfläche verbunden bleibt. Diese Kapillarringe werden durch ringförmige Objekte approximiert und dann in ein Porennetzmodell integriert. Porennetzwerksimulationen zeigen, dass Kapillarringe eine wichtige Rolle bei der Trocknung spielen können, da sie die Trocknung durch Etablierung gesättigter Luftbedingungen in entleerten Poren beschleunigen können, auch wenn sie nicht hydraulisch miteinander verbunden sind.

In weiteren Arbeiten im Zusammenhang mit der Benetzung werden die Schichtporosität und die Porengrößenverteilung von trockenen Fasermaterialien aus hochauflösenden Röntgenbildern bestimmt. Auch stationäre Flüssigkeitsverteilungen in diesen Verbundstrukturen werden aus den Bildern abgeleitet. Es werden Porennetzmodelle erstellt, die für solche realen Materialien repräsentativ sind. Mit diesen Modellen wird die Verteilung der Flüssigkeit auf die Schichten berechnet. Die Porennetzwerksimulationen stehen in guter Übereinstimmung mit den Messwerten.

Porennetzwerkmodelle, die Algorithmen für die Benetzung und für die Trocknung kombinieren, werden entwickelt, um die zeitliche Entwicklung eines Flüssigkeitströpfchens auf einem porösen Partikel zu simulieren. Diese Modelle werden durch den Transport und die Ansammlung einer gelösten Spezies erweitert. Durch diese Erweiterungen wird das Anwendungsspektrum von Porennetzmodellen erweitert. Es steht nun ein diskretes Porennetzwerkmodell zur Verfügung, das den Einfluss von Prozesszustand, Produktstruktur und Formulierungseigenschaften auf den Imprägnierungs- und Trocknungsprozess vorhersagen kann.

Neben der Erkenntnis über die Physik von zweiphasigen Strömungsprozessen (mit und ohne Phasenübergänge) in porösen Materialien durch diskrete Porennetzwerksimulationen können diese Simulationen auch notwendige Informationen zum Aufbau von Kontinuumsmodellen und deren Validierung liefern. Zu diesem Zweck werden in dieser Arbeit einige Wege zur formalen Verbindung der diskreten und kontinuierlichen Modellierungsansätze vorgestellt. Porennetzwerksimulationen spielen dabei die Rolle numerischer Experimente und werden genutzt, um eine Reihe makroskopischer Parameter der Kontinuumsmodelle vorherzusagen. Dazu gehören klassische Parameter, die für den Flüssigkeitstransport verantwortlich sind (wie die intrinsische Permeabilität, die relative Flüssigkeits- und Gaspermeabilität oder die Dampfdiffusionsfähigkeit) sowie lokale Gleichgewichtseigenschaften (Kapillardruck und Desorptionsisotherme). Neue Interpretationen für Phänomene, die für die Trocknung poröser Medien relevant sind (z.B. der nicht lokale Gleichgewichtseffekt für die Dampfphase), werden ebenfalls vorgeschlagen.

Schließlich werden die Geschwindigkeitsprofile in der Flüssigphase während der Trocknung eines porösen Mediums berechnet und analysiert. Das aus

Porennetzwerksimulationen ermittelte momentane, volumengemittelte Geschwindigkeitsfeld führt zu Stufengeschwindigkeitsprofilen. Im Gegensatz dazu führt eine einfache Massenbilanz im Kontinuumsansatz zu einem linearen Geschwindigkeitsprofil in vertikaler Richtung. Schließlich wird die Kopplung zwischen dem externen und internen Stoffaustausch bei der Trocknung poröser Medien überprüft. Diese Arbeit wird durch die Erkenntnis motiviert, dass Porennetzwerksimulationen unvergleichlich detaillierte Informationen über die Phasenverteilung an der Oberfläche poröser Medien liefern können. Die zeitliche Entwicklung von Flüssigkeitsclustern und Gasclustern an der Oberfläche wird ebenfalls durch Porennetzwerksimulationen charakterisiert. Die relativen Anteile dieser Cluster am Gesamtmassenstrom durch die Oberfläche werden damit quantifiziert. Auf dieser Grundlage wird die Qualität eines bestehenden Analysemodells beurteilt.

Abstract

This habilitation thesis aims to study the convective drying of capillary porous materials on the fundamental level. It also seeks to cover some important aspects relevant to the wetting process and the two-phase flow without phase transitions (i.e. drainage and imbibition) in such materials. The studies are conducted by means of various experimental techniques along with discrete and continuum modeling approaches.

Optical shadowscopy visualization is employed to measure the characteristics of the drying process in single and dual Hele-Shaw cells. Both cell types consist of a single layer of mono-disperse spherical glass beads sandwiched between transparent glass plates. Contrary to single cells, dual cells are comprised of two connected regions filled with small and large, hydrophilic and hydrophobic, separate and sintered particles, respectively. All cells are saturated with distilled water and dried at room temperature. Based on two-dimensional optical images wet and dry regions are determined. The time evolution of these regions clearly show how capillary effects depend on the pore structure, solid surface wettability and medium heterogeneity.

The fluid invasion and phase distributions in transparent micromodels are investigated in real time by optical photography. The micromodels are quasi-two-dimensional networks made of PDMS or silicon. The PDMS micromodels are used for drying and two-phase flow experiments, whereas the silica networks are employed for wetting measurements. From these experiments, important physical effects (such as the capillary valve effect) are unveiled and then incorporated into pore network models. Agreements between pore network simulations and micromodel measurements are better when the capillary valve effect is accounted for in the models.

Drying experiments with random packings of mono-disperse spherical particles are carried out using in situ X-ray microtomographic imaging. Packed beds are filled with separate or sintered glass beads and saturated with either distilled water or with a salt solution. The three-dimensional evolution of the liquid distribution over time is visualized via a series of snapshots from the onset of the drying process until the end. On this basis, almost all details of the structure of the liquid phase in the packing are revealed. It is observed that at low saturation the liquid phase remains connected to the packing surface through a network of liquid rings formed at contact points between particles. Capillary rings are approximated by annular objects and then incorporated into a pore network model. Pore network simulations show that capillary rings can play an important role in drying as they can accelerate the drying by establishing saturated air conditions in emptied pores even if they are not hydraulically interconnected.

In studies related to wetting in this thesis, the layer porosity and pore size distributions of dry fibrous materials are determined from high resolution X-ray images. Steady-state liquid distributions in these composite structures are also deduced from the images. Pore network models are constructed which are representative of such real materials. Using these models the distribution of liquid among the layers is computed. Pore network simulations are found to be in good agreement with the measured results.

Pore network models that combine the algorithms of wetting and drying are developed to simulate the time evolution of a liquid droplet deposited on a porous particle. These models are extended by transport and accumulation of a dissolved species. As a result of these extensions, the range of applications of pore network models is widened. A discrete pore network model is now available that can predict the influence of process condition, product structure, as well as formulation property on the impregnation-drying process.

In addition to gaining new insights on the physics of two-phase flow processes (with and without phase transitions) in porous materials by discrete pore network simulations, they can also provide necessary input to construct continuum models and to validate them. For the latter purpose, some routes for formally connecting the discrete and continuum modeling approaches are presented in this thesis. Pore network simulations play the role of suitable numerical experiments and they are exploited to predict a set of macroscopic parameters of the parametrized continuum models. These include classical parameters responsible for fluid transport (intrinsic permeability, relative liquid and gas permeabilities, vapor diffusivity) and local equilibrium properties (capillary pressure and desorption isotherm). New interpretations for phenomena relevant to porous media drying (such as the non-local equilibrium effect for the vapor phase) are also suggested.

Moreover, the velocity profiles in the liquid phase during the drying of a porous medium are computed and analyzed. The instantaneous volume-averaged velocity field determined from pore network simulations leads to step velocity profiles. By contrast, a simple mass balance in the continuum framework results in a linear profile in vertical direction. Finally, the coupling between the external and internal mass transfer in drying porous media is revisited. This study is motivated by the fact that pore network simulations can provide unequaled information on the phase distribution at the porous medium surface. The evolution of liquid clusters and gas clusters at the porous medium surface over time is characterized by means of pore network simulations. The relative contributions of these clusters to the total mass flux at the surface are thus quantified. On this basis, the quality of an existing analytical model is assessed.

Notation

A	cross section area, area	m^2
c	concentration	mol/m^3
D	binary diffusion coefficient of salt in water	m^2/s
D	moisture transport coefficient	m^2/s
F	force	N
g	acceleration of gravity	m/s^2
H	height	m
h	capillary rise	m
h	ring thickness	m
J	rate	kg/s
j	flux	kg/m^2s
k_{abs}	absolute permeability	m^2
k_{eff}	effective permeability	m^2
$k_{r\ell}$	relative permeability	-
L	throat length, characteristic length	m
M	mass	kg
$\widetilde{M}$	molar mass	kg/kmol
$\dot{M}_v$	evaporation rate	kg/s
$\dot{M}_w$	liquid flow rate	kg/s
$\dot{m}_v$	drying rate (or evaporation flux)	kg/s^2s
m	mass	kg
$\boldsymbol{n}$	(unit) normal vector	-
p	pressure	Pa
$\dot{Q}$	heat rate	J/s
R	radius of curvature	-
R	particle radius	m
$\widetilde{R}$	gas constant	J/K mol
r	pore, throat, or ring radius	m
$\overline{r}$	mean radius	m
S	saturation	-
T	temperature	K or °C
t	time	s
u	velocity	m
V	volume	m^3
X	moisture content	kg/kg
x	displacement	m
W	width	m

Greek symbols

α	half-filling angle	$^\circ$
Γ	sink or source	kg/m^{3}s
δ	vapor diffusivity	m^2/s
δ	evaporation coefficient	-
ϵ	porosity	-
ε	boundary layer thickness	m
ζ	dimensionless height	-
η	dynamic viscosity	Pa s
θ	contact angle	$^\circ$
κ	local mean curvature	-
λ	heat transfer coefficient	W/(m^2K)
μ	dynamic viscosity	Pa s
ν	kinematic viscosity	m^2/s
$\dot{\nu}$	normalized drying rate	-
ρ	density	kg/m^3
σ	surface tension	N/m
σ_0	standard deviation of throat radius	m
ϕ	opening half-angle	$^\circ$
φ	relative humidity	-

Subscripts/superscripts

a	advancing
abs	absolute
c	capillary
c	control volume (or REV volume)
con	condensation
cr	critical
cv	control volume
eff	effective
eq	equilibrium
evp	evaporation
g	gas
irr	irreducible

ℓ	liquid
min	minimum
net	network
r	ring
$r\ell$	relative
s	surface
sat	saturation
$surf$	surface
v	vapor
w	water
x, y, z	space variables
$*$	equilibrium
∞	bulk air

Dimensionless numbers

Ca	Capillary number	$\mu u/\sigma$
Re	Reynolds number	$\rho u/\nu$
Sc	Schmidt number	ν/δ
Sh	Sherwood number	$\beta L/\delta$

Abbreviations

CD	convective drying
CM	continuum model
CRP	constant rate period
CVE	capillary valve effect
CVD	convective vacuum drying
Exp	experiment
FD	freeze drying
FRP	falling rate period
GDL	gas diffusion layer
HI	hydrophilic
HO	hydrophobic
IDP	initial drying period
LHP	loop heat pipe
MRI	magnetic resonance imaging
MW	microwave
NLE	non-local equilibrium

PDE	partial differential equation
PDMS	polydimenthylsiloxane
PMMA	polymethylmethacrylate
PNM	pore network model
PSD	pore size distribution
REV	representative elementary volume
RF	Resorcinol-formaldehyde
RFP	receding front period
Sim	simulation
VMD	vacuum microwave drying
US	ultrasound

Contents

Chapter 1

Introduction and Overview

This habilitation thesis summarizes a selection of my research results obtained since my PhD thesis, defended on March 2010.

Biographical sketch since the PhD

My PhD thesis covers two major research topics: (i) the influence of liquid phase distribution on damage and deformation of compact particle aggregates during convective drying. For this purpose, the solid and liquid phases have been coupled via discrete element method and regular pore network model. (ii) The development of both two-dimensional and three-dimensional irregular pore network models for drying of an aggregate made of mono-sized spherical particles. The irregular pore network structure has been generated by Voronoi tessellation of the aggregate and the isothermal pore network drying model is generalized to the irregular structure.

Right after my PhD graduation, I started my postdoctoral project with the topic on modeling of capillary forces in convective drying of highly porous aggregates (e.g. gels). In this project we developed a simulation tool – based on a volume-of-fluid approach – that can adequately predict the evolution of the liquid distribution in a drying particle aggregate. We also carried out drying experiments with RF gels that confirm and extend literature work, especially with respect to the influence of aging. In order to assess the simulation tool, we conducted drying experiments with glass beads using X-ray microtomography, see [A] and [a].

Since January 2012 I have been leading a research team on pore network modeling and drying. In this team a major part of our activities is devoted to the development of discrete pore network models for drying of capillary porous products. We use these models to study kinetics and quality of drying products. Our vision is to bring these models to the level that can be

employed as industrial tools to optimize the real production process and the product performance. Assessing and validating the prediction quality of the pore network models by experiments is also a part of our activities in the team. For this purpose, we use optical visualizations and X-ray micro-tomography to measure time-dependent fluid distributions in micromodels, unconsolidated miniature cells and glass bead beds. We have also developed pore network models for describing the wetting, drainage and imbibition processes in capillary porous materials. A relatively new activity in the team is to compute the macroscopic continuum parameters by exploiting discrete pore network simulations. Based on this activity we aim to develop non-local-equilibrium continuum models for drying or wetting of capillary porous products.

1.1 Background and Challenges

Drying and wetting of porous materials is not only common in everyday experience, but also central to several various environmental and industrial applications. Therefore, these processes are extensively tackled from the standpoints of soil scientists, hydrologists, and engineers, often using sophisticated experimental setups and advanced mathematical tools brought from their own area of expertise. Within the engineering realm, these processes are applied either individually or in combination. Drying as an important unit operation exists in many manufacturing processes in chemical, agricultural, food, pharmaceutical, plastics, ceramics, pulp and paper industries. Wetting of porous materials is crucial for different industrial processes, ranging from oil recovery and chromatography to food processing, agriculture, heterogeneous catalysis. The simultaneous wetting and drying processes occur, for example, during agglomeration of primary particles or catalytic impregnation of porous carriers in spray fluidized beds.

Drying and wetting of (unsaturated) porous materials have motivated many studies and is still a very active research area. The studies show that the porous materials under drying or wetting can exhibit surprisingly complex behaviors even in a controlled situation. These complex behaviors are due to several simultaneous transport mechanisms that occur as inside a porous material as between the material and surrounding atmosphere. The classical mathematical description of these mechanisms is carried out by using continuum models which require spatially averaged parameters. On the other hand, the structural and morphological information of a porous medium as well as physical mechanisms controlling fluid transport are accounted for in discrete pore network models.

1.2 Porous Media

Porous materials are composed of a solid skeleton (often called matrix or frame) and an interconnected network of pores (voids) filled or partially filled with fluids (liquid and/or gas). These materials generally appear in a wide spectrum of natural situations and of engineering applications. Porous stones (sandstones), sandy soils, building materials (fire bricks, tiles, plaster), fibrous materials (such as the ones used for insulation or in the gas diffusion layer of proton exchange membrane fuel cells), porous wicks of many devices (capillary evaporators, vaporizers for volatile perfume or insect repellent liquids in a room, etc.), various fresh and processed foods and vegetables, and many pharmaceutical dosage forms, among others are examples of porous media.

It is difficult to give a consistent classification of porous media in solid materials. A useful attempt, at classification based on pore size, has been made by Prat [1]: capillary porous media (often called non-hygroscopic porous media in literature) refers to porous materials in which the pore size is typically in the micrometer range (up to, say, sizes in the order of 100 μm). In a capillary porous medium the maximum amount of water that the interior solid surface adsorbs (bound water) is negligible compared to the capillary water (freely mobile water) available in the pore space volume of the medium (see Fig. 1.1). Thus water in a capillary porous medium is spatially allocated by capillary forces as a result of direct contact between liquid water and the medium. A reasonably good example of capillary porous materials are bricks and paper stocks as well as a random packing of particles with an average size larger than 1 μm (up to a few hundreds of μm). On the other hand, in hygroscopic porous media the pore sizes are all smaller than about 100 nm. This implies that a significant portion of water in a hygroscopic porous medium is bonded (bound) to its solid matrix through chemical, physico-chemical or physical forces. Cement paste and many food products such as potato and rice are examples of hygroscopic materials. This distinction is particularly important when drying of porous materials is concerned (see Sec.1.3). Based on this classification, the drying rate of a hygroscopic porous medium drops right after the onset of the drying process, whereas the drying rate remains (nearly) constant for a certain period of time during drying of a capillary porous medium. This classification might however be ambiguous with regard to its relevance to drying. Because the constant drying rate period is observed during drying of wood as a hygroscopic porous material. In the specific kind of porous materials such as concrete, pore sizes are typically in both the capillary range and the hygroscopic range; such materials are called partially hygroscopic-capillary porous media.

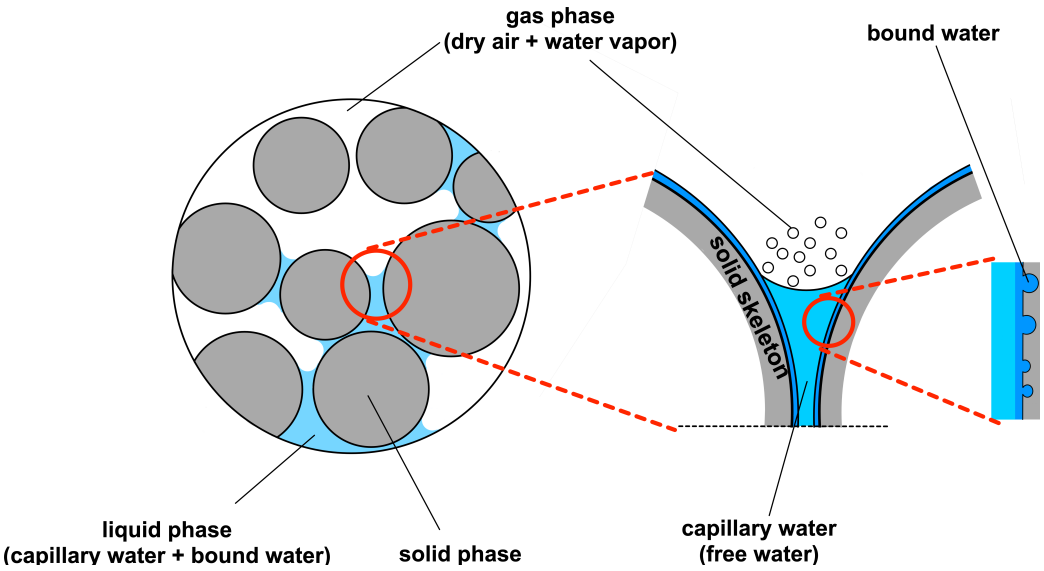

Figure 1.1: Schematics representation of a multiphase porous medium.

Porous media can also be classified according to the ratio of their thickness to lateral dimensions. A porous material is referred to as a thin porous medium if its thickness is much smaller than its lateral dimensions. The thickness of such a medium is only around one order of magnitude larger than its mean pore size [2]. Examples of thin porous media can be found in many emerging industrial and domestic applications, such as filters, fuel cells, batteries, biomedical porous coatings, printing papers, automotive catalysts, and hygiene products (e.g. diapers and wipes). This relatively new distinction is of paramount importance for both mathematical modeling and experimental measurements.

In this thesis, transport phenomena in a rigid porous medium is studied. Rigid means that the spatial morphology of the solid matrix remains unchanged in the course of a process. Thus, swelling porous media as well as those that may undergo morphological changes due to a physico-chemical interactions between the pore surface and fluids are not studied in this thesis.

1.3 Drying Kinetics

Convective drying is conceived as separation of volatile liquids (usually water) from moist materials by evaporating the liquid and sweeping away the generated vapor from the material surface. This is a thermal separation pro-

cess and the heat required for evaporation – that is at least vaporization enthalpy – is carried by the drying agent (usually air). This process actually involves not only heat transfer, but also the external (or gas-side) and the internal (or intraparticle) mass transfer as well as thermodynamic phase change, that is, evaporation or condensation.

The drying kinetics of a wet solid sample is determined experimentally. During each laboratory experiment the air conditions (i.e., the total pressure, the temperature, the relative humidity, and the air velocity) are kept nearly constant. This condition is obtained by maintaining a very high air/sample ratio, so that the changes in air properties as a result of drying itself are negligible. The relationship between the drying rate (dS/dt or dX/dt) and the overall saturation (S) or the average moisture content (X) results in a curve which characterizes the drying kinetics of the porous sample [3, 4]. Drying curves that are determined under typical room conditions are commonly presented in two ways as shown in Figs. 1.2 and 1.3. Figure 1.2 is usually considered for situations with technical applications [5], whereas the drying curve shown in Fig. 1.3 is rather common in fundamental studies. The latter description of the drying curve can be simplified with the distinction between only two periods: the first period corresponds to both the initial drying period (IDP) and constant rate period (CRP) and the second period is characterized by both the falling rate period (FRP) and receding front period (RFP).

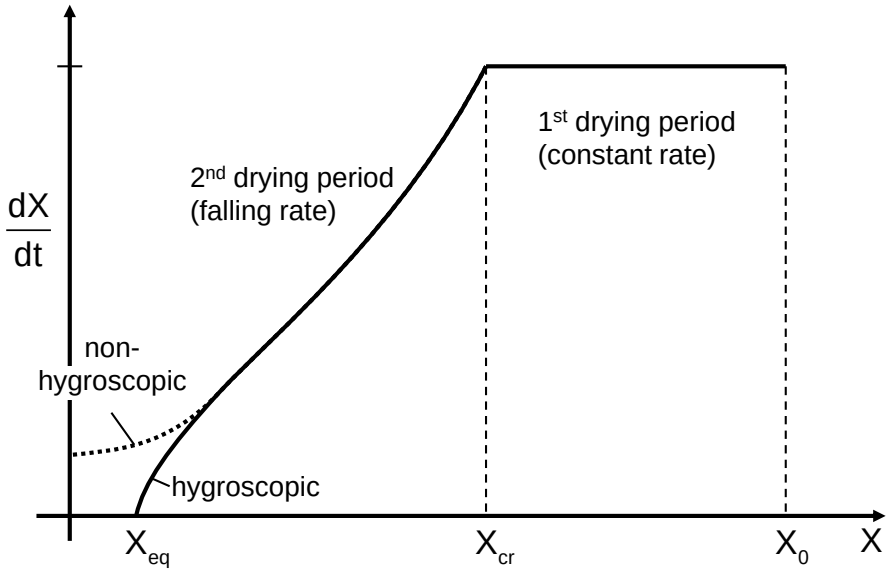

Figure 1.2: Drying rate curve. X_0 is initial moisture content, X_{cr} critical moisture content, and X_{eq} equilibrium moisture content.

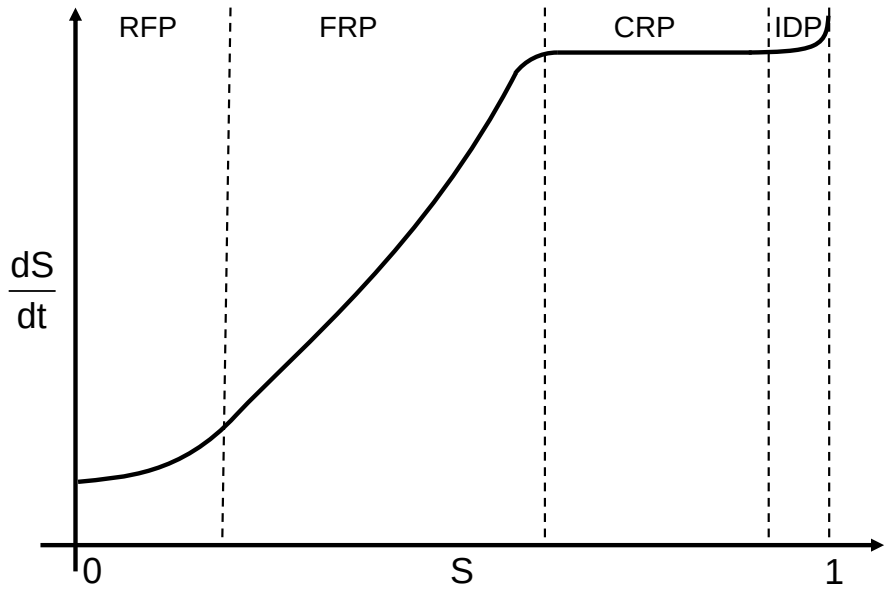

Figure 1.3: Scheme of a drying rate curve for a capillary porous medium. Four representative periods are shown: initial drying period (IDP), constant rate period (CRP), falling rate period (FRP), and receding front period (RFP).

The first period known as IDP or surface evaporation regime is characterized by the evaporation of the most external mass of liquid. This period is associated with the invasion of surface pores until the gas phase touches the bottom of the sample for the first time, i.e., breakthrough. This very first period cannot usually be seen in drying curves, which are determined from gravimetric drying experiments. Because the mass of liquid evaporated in this period is very small compared to the total mass of liquid initially available in the sample. However, this sharp drop in the drying curve (or in the corresponding saturation profiles) can be observed if non-invasive experimental techniques (e.g. X-ray microtomography or nuclear magnetic resonance) are used [6]. Because these techniques can give access to the spatial distribution of moisture in both the interior and near the surface of the drying sample. In this thesis, the IDP is characterized by three-dimensional pore network simulations – see Chapter 4.

In CRP, liquid is brought to the porous medium surface by capillary forces through hydraulic connections among pores. This process is rapid enough to balance the rate of liquid removal at the surface. The drying rate essentially remains constant and, roughly speaking, the medium surface behaves like a liquid surface with the saturated vapor pressure in the surrounding gas phase. During this period, the drying rate is controlled by the external conditions and the medium attains the wet bulb temperature.

The end of the CRP and thus the transition toward the FRP occurs at the critical moisture content, where the capillary forces can no longer bring enough liquid to the medium surface (viscous forces dominate capillary forces) and the liquid surface breaks into patches and the averaged vapor pressure at the surface drops below the saturation value. Drying is thus mainly governed by mass transfer through the dry pore space. The critical moisture content depends on the drying rate of the first period, the dimensions of the medium and its inner pore structure. During the FRP, the moisture content of the solid approaches the equilibrium value for hygroscopic materials or goes down to zero for capillary porous solids. At the equilibrium moisture content, a hygroscopic material, which is surrounded at least partially by air, neither gains nor looses moisture – see sorption isotherm in Chapter 2. The temperature of the medium gradually rises to the temperature of the bulk air. A dry region near the open side of the medium and a liquid-vapor zone away from it develops in the RFP.

Drying curves can be used for practical scenarios in which the air/sample mass ratio is more realistic compared to that in lab experiments. They can be used to determine the time required to dry a bed of agglomerates or a thin layer of slurry. For such purposes drying experiments with a small sample should be conducted under controlled conditions for several different external conditions. Then by applying certain transformations on the variables of the drying curve, a single characteristic curve can be constructed. This curve is often referred to as the normalized drying curve. If the normalization is done successfully, the results of all drying experiments, which are obtained under different external conditions, lie on the same single curve. This curve can then be used to calculate the drying time. This method was introduced by van Meel [7] and since then it has widely been applied in the original form or in modified forms by many authors, e.g. [8].

It may worth to remark that drying is often used interchangeably with drainage, because in both processes a wetting liquid is displaced with a non-wetting gas. An asymmetric aspect of these processes is that mass transfer is a key element in drying, whereas drainage is a pure mechanical process.

1.4 Drying Theories of Porous Media

As in other fields dealing with fluids in porous media, three main approaches have been used to derive mathematical models for the drying process in porous media (see Fig. 1.4): At the effective medium scale, a continuum approximation is used for the partially saturated porous medium and the distributions of the state variables (i.e. temperature, moisture content, and

pressure) are described as functions of space and time. The dynamics, i.e. the time evolution of these distributions, is given by a set of partial differential equations (PDEs) [9, 10]. While classical and extremely useful, and in spite of many studies [11, 12], the continuum models (CMs) we have at our disposal are inadequate for various reasons. Like any other continuum model, these CMs require a priori knowledge of medium-specific macroscopic transport parameters, which are averages of corresponding microscopic properties and are often determined by laborious experiments. On the other hand, the microscopic models, which are able to resolve the sub-pore scale morphology and physics, are far from being practical, either computationally or analytically. In microscopic models, the liquid-gas interface motion is tracked over time in every single sub-pore element, e.g. in a single voxel, see [13] and [a]. In-between these two model hierarchies (macroscopic and microscopic), the mesoscale discrete pore network models (PNMs) have been developed extensively since recent years [1]. A PNM considers the medium at the pore scale, where the void space is represented by a network of pores. Micro or nanofluidics models used in each pore give rise to a large system of ordinary differential equations with degrees of freedom at each node of the pore network.

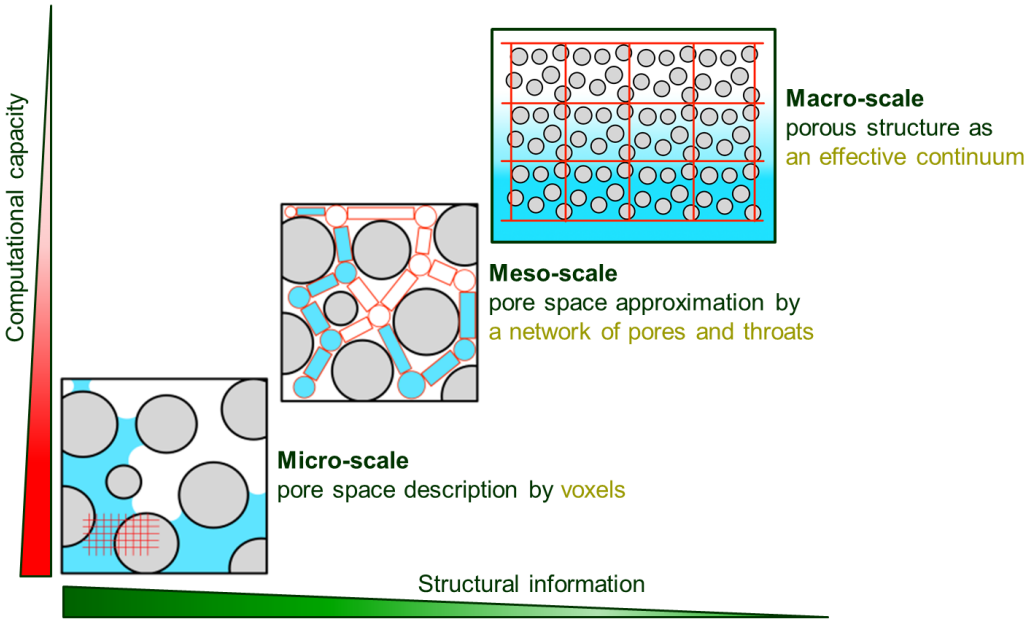

Figure 1.4: Three model hierarchies defined based on the spatial scale.

1.4.1 Continuum Models

The history of continuum models (CMs) for drying dates back to the 1950s. As often cited, Philip and De Vries in 1957 [14] as well as Luikov in 1966 [15] were the first who proposed a CM for the transport of moisture in rigid homogeneous porous media during drying from purely phenomenological or formal considerations. This model is based on the diffusion equation that accounts for the effects of capillary flow, vapor transport, and the coupling with heat transfer. In 1975, Luikov derived the macroscopic equations governing the heat and mass transfer by volumetric summation of transport equations of each phase based on the corresponding Darcy-scale macroscopic flux relationships [16]. In such a formulation Darcy-scale parameters are assumed to exist and to be known a priori.

Developing the macroscopic transfer equations for each phase from microscopic balance equations has become more familiar as scientists attempt to come to grips with the complexity and uncertainty in natural and engineered systems. Whitaker [9] derived these macroscopic equations by virtue of formal up-scaling (homogenization) procedure in 1977 [10, 17]. This procedure is applied for a representative elementary volume (REV), which may contain many pores in each coordinate direction. This model involves constitutive laws (often called closure relations) which require the local values of the effective material properties, such as the diffusivity, permeability, and thermal conductivity. These effective parameters are the averages of corresponding microscopic properties of the REV, and can ensure only partial compensation of the micro-scale information. It is often a challenging task to determine properly the values of these parameters because they depend on both the pore structure characteristics and the pore-level physical processes involved.

This advance CM has widely been used with the aim of predicting the distributions of the moisture, liquid pressure, gas pressure, and temperature fields in porous media during drying. The set of equations governing this model have been presented and discussed in many references, e.g., [1, 9, 11, 18]. A simple version of Whitaker's model and a route to formally connect its effective parameters to mesoscopic pore network simulations are recalled and outlined in Chapter 4.

The strengths of the CMs for drying are manifold: it is relatively easy to provide proper boundary conditions for the PDEs governing the system. These PDEs can be solved with reasonable computation overhead by using well-established mathematical tools. Simulation results obtained from the solution of the PDEs can directly be compared with macroscopic lab data [16]. This traditional view to porous media drying, however, is incomplete. For example, the assumption of local equilibrium regarding the partial water

vapor pressure is not valid. The mass transfer at the interface between the porous medium surface and the bulk air is poorly modeled. Moreover, cluster formations and secondary capillary effects (liquid films, liquid rings, etc.) cannot be described by the classical CMs.

1.4.2 Pore Network Models

Pore network models (PNMs) are based on an explicit representation of the void space within a porous medium as a network of pores interconnected by constrictions called throats. The pores and throats often have prescribed shapes but are random in their size providing disorder of the real pore space – the "geometry" of the porous medium. The pores and throats are connected to each other as required – the "topology" of the porous medium. All relevant transport equations for both dispersed and continuous phases and for the corresponding interfaces in a partially saturated porous medium are modeled directly at the pore network level using fundamental physical laws and exploiting the concepts of percolation theory, fractal concepts and scaling theory [19, 20, 21]. This description ensures important features, such as description of the gas phase breakthrough and gradient-free average saturation profiles during the early stage of the drying process. Pore network simulations also provide access to all details of the liquid structure in a porous medium during drying. This feature enables to distinguish between isolated liquid clusters (which are not connected to each other or to the boundary of the two-phase region with liquid-filled pores) and the percolating liquid cluster (which spans the entire two-phase region of the drying material). These attributes are however neglected and out of reach in the continuum models. In fact, the physics and the structure at pore scale are more or less "hidden" in the effective parameters of the continuum models.

PNMs were originally developed to describe immiscible displacement in porous media (e.g., for secondary oil recovery) and later tailored to simulate the drying process. Pioneering work on pore network modeling of drying has been done by Prat [22, 23]. Since this first work, the pore network modeling of drying can be claimed to have continuously improved and extended not only by Prat's group, but also by other prominent research groups. Prat's group has studied the fundamentals of physical and geometrical effects relevant to porous media drying, such as liquid viscous and gravity effects [24], heat transfer [25], pore shape [26], etc. Yiotis and his co-authors have also contributed to the development of drying PNM, addressing the liquid and gas viscous effect [27], for instance. The Chair of Thermal Process Engineering at Otto-von-Guericke University (OvGU) has started its research activities on the pore network modeling of drying since 2003. In this Chair, the ini-

tial focus was to investigate the impact of pore structure, that is, pore size distribution, spatial correlation of pore size, and coordination number of the network on drying kinetics of porous materials [28]. Later, other relevant physical effects such as gravity and liquid viscous effects [29], heat transfer [30], as well as solid-fluid interaction [31] were taken into account. Further model and application extensions achieved recently on the pore network modeling of drying is discussed in Chapter 4. Next section in this chapter is devoted to description of the wetting process and a brief review of the state of the art of porous media wetting modeling.

1.5 Wetting Kinetics

Wetting (or rehydration) is the reverse process of drying, during which a wetting liquid (usually water) intrudes into a porous material and replaces a non-wetting gas (usually air) confined in the material. This fluid-displacement phenomenon is governed by the interplay of venerable capillary (or suction) forces at the phase interface and the viscous drag forces within each phase. This process is also referred to as spontaneous imbibition. It is however called forced imbibition if the process is driven purely mechanically, e.g. by means of a pump. In latter case the flow rate of the wetting phase is constant and imposed externally, whereas in spontaneous imbibition it adjusts itself in order to balance viscous and capillary forces and is therefore a varying quantity.

The kinetics of liquid uptake into porous samples can be determined experimentally. During each experiment the porous sample is carefully brought in contact with a fixed bath of viscous liquid. Typically, one facet of the sample is plugged into the (large) water bath to a certain depth. Then, the capillary rise of liquid into the sample is determined either visually from the lateral side by using a high-speed video camera or gravimetrically by following the liquid mass penetrated into the sample. Finally the distance which has become wet by the liquid phase (H) or the overall sample saturation (S) is read at various times (t). The relationship between S and t (or H vs. t) results in the wetting (or spontaneous imbibition) kinetics curve [32, 33].

Figure 1.5 shows schematically the wetting kinetics of a porous sample under constant initial and boundary conditions. The time variation of the overall saturation can be explained as follows: right upon contact of the sample with the surface of the liquid bath ($t = 0$), the liquid is forced into the sample by capillary action. As a result, the interface between wet and dry regions develops in the sample. This interface is called the wetting front. At the beginning the front propagates fast and slows down over time due to

the increasing length of the distances connecting the wetting front with the liquid bath. The process continues until the sample is fully saturated with the liquid, i.e. $S = 1$. Since wetting essentially occurs within a very short time window, it is often assumed that evaporation has a negligible impact on the variation of the liquid volume in the sample. The role of air trapping during the wetting process is often neglected. However, air can be trapped within the pore structure of the medium leading to pressure build-up ahead of the wetting front.

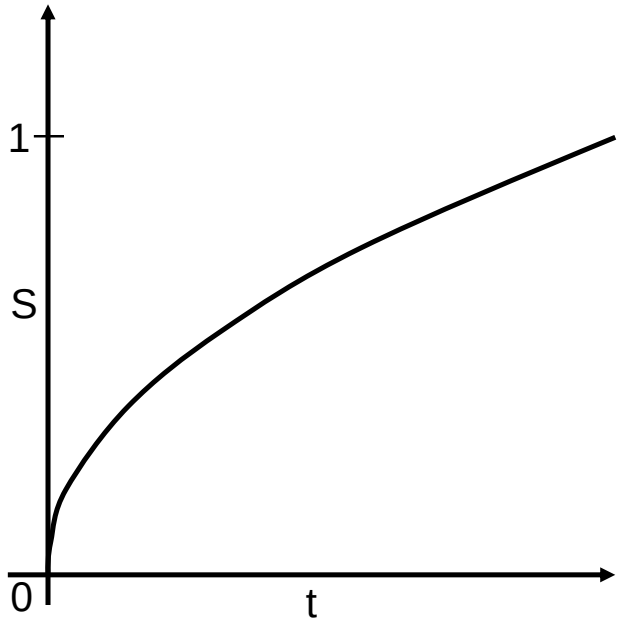

Figure 1.5: The time variation of the overall saturation $S(t)$ during the spontaneous liquid uptake into a dry porous medium. This curve can also be shown as $H(t)$.

Three characteristic regimes may be distinguished for wetting of a porous medium by a liquid. The very beginning of the wetting process is the inertial regime, in which the liquid invades into the pore space in a rather ballistic manner. Such a turbulence regime might be relevant in the case where the contact time between the liquid and medium is very short, as in printing. In this regime the height of the front scales linearly with the elapsed time t. The duration of this regime can be estimated by the scaling model. Next regime is the Lucas-Washburn with the "classic" square-root-of-time-behavior, where capillary and viscous forces prevail. Last regime occurs at the very late period of wetting, during which gravitational forces significantly affect the process dynamics [34].

1.6 Wetting Theories of Porous Media

Approaches for modeling the wetting process in partially saturated porous media can generally be defined based on the spatial scales, which are schematically shown in Fig. 1.4. As mentioned previously, each of these modeling approaches has its own strengths and weaknesses. A porous medium is treated as a continuum within which the dynamics of the wetting process is described based on the simplified laws of hydraulics. In this traditional viewpoint, both the medium structure and the fluid properties are homogenized completely. This loss of information is partially compensated by the introduction of the effective properties appearing in classical continuum models, which are developed based on first principles [35, 36]. If the exact position and shape of the fluid-fluid interfaces in the porous medium and the sub-pore scale physics during the wetting process are of interest, they can be provided by the micro-scale methods, such as direct numerical simulations using molecular dynamics [37, 38], lattice-Boltzmann method [39, 40], volume-of-fluid [41, 42], and full morphology methods [43, 44]. The micro-scale methods are however computationally too expensive and, hence, less appropriate for applications at the product scale. Nevertheless, they can serve as benchmarks to somehow assess both the macroscopic continuum models and mesoscopic pore network models. Like in drying, the core idea in pore network modeling of wetting is to represent the complex pore space by a network of pores with a size distribution and to describe relevant transport phenomena as discrete events in individual pores. Since the pore network models are able to account for the pore heterogeneity within relatively large sample volumes, they are also considered as a suitable numerical experiment to identify the effective transport properties of wetting porous structures [45].

1.6.1 Continuum Models

More than a century ago Bell and Cameron [46], Lucas [47], and Washburn [48] described the dynamics of liquid penetration into a confined porous medium as a capillary rise problem with a law, which is often called the classical Lucas-Washburn equation (or cylindrical tube model). Based on this equation the overall saturation (or liquid column height) in a porous medium varies with $\sqrt{t}$. This power law behavior is independent of the microscopic details of the medium. It is valid down to nanoscopic pore sizes [49] and particularly robust with regard to the geometrical complexity of the medium [50]. Despite the fact that this equation is widely used, there are wetting circumstances that do not obey the Lucas-Washburn behavior, such as when the wetting fluid is non-Newtonian (e.g. ink) or when the porous medium

property changes during wetting (e.g. swelling of the paper fibers) [51].

In the analysis of the wetting process by the help of the Lucas-Washburn equation, a flat front is assumed between the liquid and gas phases inside a porous medium. This means that the saturation in the wet and dry regions of the medium is, respectively, unity and null. However, it has been observed that in some circumstances, such as in highly heterogeneous porous media [52], the wet and dry regions are separated by a partially saturated region at the front vicinity, i.e. a two-phase transition zone. In this situation, the Lucas-Washburn law may not accurately predict the wetting dynamics. This limitation was overcome by Richards in 1931 [53]. His model, which is referred to as the Richards equation, is able to describe the wetting process in porous structures in which a two-phase region has been developed. Richards derived his equation from combining the mass conservation law with Darcy's law and from assuming the gas phase to be stationary. The resulting equation is a diffusion-type model. This does not mean that the Richards equation describes a diffusion process, it only makes clear that this equation behaves mathematically as a (non-linear) diffusion equation.

Although these continuum models can satisfactorily describe the overall kinetics of the wetting process, they assume that both the pore structure and liquid distribution can be homogenized for a description with constant parameters or smoothly varying functions and variables. Therefore, these models cannot describe wetting behavior of porous materials with non-uniform or anisotropic pore structures. These models are not suited for percolation phenomena with fractal and discontinuous liquid clusters. Such a situation occurs when uptake capacity of porous materials is smaller than liquid amounts. These models cannot properly describe the wetting of a porous medium with size much larger than its pore sizes (as for thin porous layers), because the two scales cannot be distinguished. Both the Lucas-Washburn and Richards equations are revisited and also assessed against pore network simulations of wetting in Chapter 4.

1.6.2 Pore Network Models

As in drying, the original intention behind description of wetting phenomena by pore network modeling was to account for both the structural details of porous media and relevant pore-scale physics. During wetting the fluid transport dynamics through a network is determined with the relevant physics implemented on a pore-to-pore basis. The flow in each pore is of Poiseuille type, and the advancement of the overall wetting front is driven by the pressure difference as well as by local fluid mass conservation at each pore junction in the network. This algorithm accounts for all relevant physics

and can simulate dynamic behavior of the wetting process. Therefore, a pore network model developed based on this algorithm is referred to as the dynamic pore network model. The most consequence of this model is that a characteristic time-scale of the process can be calculated. A much simpler version of this dynamic model – both conceptually and algorithmically – is also developed by ignoring all viscous effects; this model is referred to as the quasi-static pore network model. Though simple, it can still be useful in appropriate contexts. For instance, a quasi-static pore network model can be used to simulate capillary pressure curves, which are intended to be a probe of pore structure.

It should be noted that the dynamic pore network models are classified into two cases with regard to the relative importance of capillary and viscous effects. If capillary effects are dominant, the liquid displacement resembles an invasion pattern similar to that obtained from quasi-static simulations. This limiting case of the dynamic pore network model is expected when the liquid flow rate is very low. An important point is that even at a very low value of rate, the wetting front can still exhibit dramatic differences from quasi-static simulations in the same porous medium. Because of this reason, a direct comparison of the two methods (quasi-static vs. dynamic) in the limiting case of a very low flow rate must be prevented.

Since the pioneering work of Fatt for prediction of capillary pressure-saturation curves [54], pore network modeling of wetting has been advanced further in two main directions. Efforts are mainly made to either incorporate the structural and/or physical effects into pore network models [55, 56] or to determine the single-phase and two-phase flow parameters of porous media [45, 57, 58, 59]. Among others, Thompson [55] studied wetting kinetics and phase distribution in several model fibrous materials under different boundary conditions. How the structure of the wetting front evolves during liquid penetration into a porous medium with elongated pores is studied by exploiting pore network simulations in [60]. Blunt and his co-workers in several publications calculated single- and two-phase flow parameters of different samples from pore-network simulation results, e.g., see [61]. For a comprehensive review on recent developments in the pore network modeling of wetting, the reader may refer to [62].

We have also developed a pore network model for wetting of porous structures. Our original intention was to predict the liquid phase distribution in wet wipes, which are used in home and personal care [63]. An extended version of this model, which combines wetting with drying, is now available that can be used to study particle-droplet interactions in fluidized bed processes at the pore level. Also, an assessment of the continuum models is made by means of pore network simulation results. All these applications

and progresses are discussed in Chapter 4.

A final remark is that pore network models could describe real phenomena that occur in a porous medium during the drying or wetting or any other process. However, they cannot directly be used in most industrial applications. This is because the maximum number of pores that can be typically considered with the available pore network models do not exceed 10^3, which is several orders of magnitude smaller than the number of pores typically present in real-size pore structures. The industrial need for such simulation tools would definitely arise when the high-performance computing pore network modeling codes have developed. Then, they could be utilized, for example, to optimize a porous product with respect to its process properties.

1.7 The Contribution of This Thesis

In this thesis, several aspects of the drying and wetting processes in capillary porous media are investigated. For this purpose, both experimental methods and mathematical models are employed. On the experimental side, two visualization techniques are described that are utilized in our research projects to monitor the dynamics of the drying and wetting processes in various systems. On the modeling side, discrete pore network and continuum models are developed to simulate the liquid-gas interface dynamics during these processes.

Some important physical properties of wet solid and of wet air are briefly recapitulated in Chapter 2. Understanding of the physical laws used to quantify these properties are prerequisites for modeling transport events that occur during drying and wetting of porous media.

In Chapter 3 packed beds of glass beads and microfluidic networks are described. These model systems are chosen on purpose, because the view is that one must be able to measure drying or wetting for these relatively simple systems prior to considering materials common in engineering applications (fibrous materials, formulated particles, bricks, etc.). To measure the drying or wetting kinetics of these model systems, optical and X-ray microtomographic techniques are used. The application of these techniques depends on the level of information and insights that one seeks. For instance, if the overall kinetics of the drying or wetting process is of interest, the optical technique may be sufficient. However, if the explicit spatio-temporal resolution of the solid, liquid, and gas phase in a particle packing is an objective, X-ray microtomography shall be used.

Discrete pore network models as well as the classical continuum models for drying and wetting are described in Chapter 4. The pore network

models are developed at the Chair of Thermal Process Engineering at the OvGU, while the classical continuum models are adopted from the literature and then parametrized. Focus in this chapter is not to explain every single component of the pore network models and the numerical techniques used to solve the equations governing these models. Instead, this chapter provides achievements made in incorporating new physical effects (e.g. capillary valve effect, secondary capillary structure, etc) into the existing pore network models as well as model extensions to solute transport and solidification. Another major focus is to introduce and apply approaches for determination of the volume-averaged transport parameters of a capillary porous medium. For this purpose both top-down and bottom-up routes are employed. The validity of the predicted parameters are directly assessed by applying them to the respective continuum models. The research results reported in this chapter shed light on existing and emerging knowledge relevant to advanced modeling of drying and wetting processes. Thereby, they could pave the way for future research.

Chapter 5 summarizes the main results presented in this thesis, and also highlights future recommendations.

Other contributions not in this thesis

Several papers are not mentioned in this thesis, because as the title of the thesis already portrayed, the physics of pore-scale phenomena in partly saturated porous media is the key topic. I briefly describe these results below.

Convective drying of highly porous particle aggregates I worked as a postdoctoral fellow on this research project, which was defined within the Priority Program 1273 "Colloid Process Engineering". In this project, we synthesized several resorcinol-formaldehyde (RF) hydrogel samples by sol-gel polycondensation of resorcinol (R) with formaldehyde in the presence of sodium carbonate as a catalyst (C). The mechanical effects (cracks and shrinkage) induced by convective drying in RF gels with three different R/C ratios and three different aging times were investigated. It was found that decreasing R/C ratio dramatically increases the degree of shrinkage and also that longer aging slightly reduces the degree of shrinkage [A]. In order to gain a better understanding of the pore-scale phenomena during drying, we produced aggregates of sintered glass beads as a model system, for which we investigated the liquid distribution during drying at the pore scale using X-ray microtomography [A]. To simulate the liquid distribution at the microscopic scale in such highly porous model particle aggregates during drying, we developed a computational tool based on the volume-of-fluid approach.

Prior to full simulations, several test problems were solved numerically in order to show that the algorithm can adequately predict the liquid relaxation into capillary equilibrium, e.g. the relaxation of a flat meniscus confined in a cylindrical solid tube containing a spherical solid particle and the relaxation of a cubic liquid block between two spherical particles. Such test problems could verify the correctness of our simulation approach. The impact of the solid wettability on the equilibrium liquid phase distributions in a real (sintered) particle aggregate [A] and a numerically generated particle aggregate with large openings [a] were studied numerically. The results show that the capillary effects are more noticeable for smaller equilibrium contact angle: small pores remain saturated for a longer time, while large pores dry out earlier.

Characterization of soft material agglomerates This was the topic of our own PhD researcher, Reihaneh. In this project, maltodextrin agglomerates were produced in a lab-scale batch fluidized bed granulator. Based on X-ray images several descriptors were developed in order to characterize the three-dimensional morphology and internal structure of the produced agglomerates at the microscopic scale. Contrary to insoluble hard material agglomerates (e.g. glass beads), maltodextrin primary particles are soft and may thus deform and overlap as they go above the glass transition temperature during the agglomeration process, yielding particles of complex structures and irregular shapes. A comprehensive methodology was developed based on the preflooded watershed segmentation of X-ray images to identify the primary particles in maltodextrin agglomerates. Among other descriptors, the radius of gyration and the fractal dimension were calculated. The low value of the fractal dimension, the high value of the porosity and the low value of the sphericity proved that maltodextrin agglomerates produced in a spray fluidized bed exhibit an irregular, open and fluffy structure. The most serious limitation concerning this method is the time and effort necessary for measurements and, especially, for image processing, which limits the number of agglomerates that can be analyzed and assessed. The results obtained in this project have already been published in [b, c, d].

Single and combined drying of hygroscopic plant porous materials We worked with Ángel, who was a PhD researcher visiting the Chair of Thermal Process Engineering at that time, on drying kinetics and microstructural and sensory properties of chokeberries dehydrated by using six different drying protocols comprised of three single drying techniques, i. e., freeze drying (FD), convective drying (CD), vacuum microwave drying (VMD) as well as three serial combinations of drying methods, i. e., CD followed by VMD,

osmotic dehydration followed by VMD, osmotic dehydration followed consecutively by CVD and VMD. The measurement results revealed that single VMD at 360 W was the best option for chokeberry drying. Because this drying method resulted in short drying time (40-70 min), low bulk density (160-215 kg m^{-3}), high porosity ($\approx$ 39%), low hardness (43-55 N), as well as relatively low intensities of sourness ($\approx$ 3.5), bitterness ($\approx$ 3.5), and astringency ($\approx$ 2.0). The samples dried by using FD had the highest value of porosity ($\approx$ 80%). The samples dried by using hybrid CD-VMD exhibited a porosity of $\approx$ 28%. On the other hand, osmotic dehydration coupled with VMD or CVD-VMD increased the sample porosity up to $\approx$ 50%. Osmotic dehydration coupled with VMD enhanced significantly the crispiness of the dried samples. The results obtained in this joint work have been appeared in [e].

In the frame of a research collaboration with Justyna we studied experimentally drying kinetics, microstructural variations as well as rehydration characteristics of raspberry fruit. The samples of raspberries were dehydrated by means of convective drying (CD) assisted simultaneously by ultrasound (US) with power of 100 W and by microwave (MW) with power of 100 or 200 W. The hybrid drying processes were as follows: CD-US_{100}, CD-US_{200}, CD-MW_{100} and CD-MW_{100}-US_{200}. We have found out that the combination of high airborne ultrasound and microwave with convective drying, i. e. CD-US_{200} and CD-MW_{100}, shortens dramatically drying time by $\approx$ 55-80% and reduces energy consumption up to $\approx$ 60% as compared to CD method. The shortest drying time was observed for the samples dried by the combination of the three drying processes, i. e. CD-MW_{100}-US_{200}. The highest porosity ($\approx$ 80%) and the best rehydration capacity ratio ($\approx$ 2.2) were obtained for the samples dried by CD. Detail of this work can be found in [f, g]. Together with Justyna we conducted another study on intermittent drying of red beetroots [h].

In a research collaboration with Seddik, who was working at Unilever at that time, we investigated the porosity profiles of some vegetables (mushroom, eggplant, zucchini) that were obtained from the corresponding X-ray microtomographic images. It was observed that neglecting the volume of regions in fresh vegetables, which are initially filled with air, can lead to an error in prediction of the porosity profiles. Thus, two mechanisms can contribute to the evolution of the profiles during the drying process: the volume change of regions initially filled with air (shrinkage mechanism) and the volume change of regions initially filled with water (collapse mechanism). These two mechanisms can occur simultaneously either in parallel or in series and hence can influence the porosity profiles of dried samples. More discussion on this topic is reported in [i].

Microencapsulation of functional oils by spray drying Samira was a PhD researcher visiting the Chair of Thermal Process Engineering. We studied the incorporation of walnut oils into several different coating materials (skim milk powder, skim milk powder+Tween 80, skim milk powder+maltodextrin) by means of spray drying method. This study was conducted at the level of a single droplet [j] and the pilot-scale spray dryer [k]. We carried out several single emulsion droplet drying experiments under several well-controlled drying conditions. We found out that an increase in drying air temperature and total solid mass fraction can promote the solid crust formation. In addition to these measurements, we produced microcapsules by using the spray dryer at different inlet drying air temperatures (140, 160, 180°C) and feed atomization pressures (2, 3, 4 bar) in order to determine the optimal drying conditions for maximizing the microencapsulation efficiency. The maximum encapsulation efficiency ($\approx 90\%$) was obtained with the emulsion prepared by combination of skim milk powder and Tween 80 at a drying air temperature of 180°C and a feed atomization pressure of 3 bar. We believe that the insights gained from this study can be used to track the encapsulation efficiency and the lipid oxidation during the drying of droplets and particles containing functional ingredients. An overview of techniques that can generally be used to manufacture microcapsules is provided in [l, m].

A note on references

References to my publications use alphabets, and refer to my list of publications, which can be found in Appendix A. References to other works use numbers, and refer to the bibliography which can be found on page 128.

Chapter 2

Brief Recap of Physical Phenomena in Porous Media

The coexistence of solid, liquid and gas phases in the void space of a partly saturated porous medium gives rise to a variety of interfacial phenomena. Liquid capillarity results from the interplay of different intermolecular forces: The attraction between the liquid molecules (measured by the value of surface tension) and the attraction between the liquid molecules and the pore wall (measured by the value of contact angle). This physical phenomenon leads to liquid transport in pores. When the vapor pressure in the gas phase is high, a continuous liquid film may form in small pores. The vapor pressure in such pores is reduced with respect to the curved liquid surface and thus capillary condensation may take place. The understanding of these physical phenomena is a key ingredient for being successful in developing fascinating models relevant to flow and transport in partly saturated porous media. A thorough description of these phenomena is beyond the focus of the current chapter, yet they are briefly recalled.

2.1 Liquid Properties

2.1.1 Surface Tension

Surface tension σ can be defined based on force or energy standpoints. In terms of force, at the interface between water and air or solid, water molecules are exposed to forces different than that within the bulk water. The cohesive forces between water molecules down into the bulk liquid are shared uniformly with all immediate neighboring molecules via hydrogen bonds. On the other hand, those molecules at the water-air interface lack neighboring

T (°C)	0	20	40	60	80	100
σ (mN/m)	75.7	72.6	69.4	66.1	62.5	58.8

Table 2.1: Surface tension of water (non-wetting fluid is air) at various temperatures.

molecules above, and experience stronger net attractive forces upon their nearest neighbors at the interface. This is because water molecules on the air side of the interface have lower density, with most hydrogen bonds formed at the liquid side. This enhancement of the intermolecular forces at the surface results in a stretched membrane-like water surface with infinitesimal thickness. As a result, internal pressure is created that forces water surface to contract to the minimal area [64].

Surface tension can also be viewed from the interfacial energy standpoint. A molecule in the bulk liquid is in direct contact with a neighbor. This molecule is in a lower state of energy than if it were alone. The interior molecules have as many neighbors as they can possibly have, whereas the molecules at the interface are missing neighbors and thus have a higher level of energy. In order for the liquid to minimize its energy state, the number of higher energy interface molecules must be minimized. The minimized quantity of interface molecules results in a minimized surface area. For this reason, droplets of water tend to be pulled into a spherical shape by the cohesive forces of the surface layer so as to minimize the necessary wall tension of the surface layer.

Surface tension depends on temperature. Usually it decreases linearly as the temperature rises. This is due to the fact that thermal expansion reduces the liquid density and thus the cohesive forces at the surface (as well as inside) of the liquid phase. Table 2.1 gives values of surface tension at different temperatures where the gas phase is air.

Moreover, surface tension can be affected by the substances dissolved in water (e.g. ions or solutes). If the affinity of the ions to water molecules is greater than the affinity of the water molecules to one another, then the ions tend to be drawn into the electrolyte solution leading to enhancement of the surface tension. For instance, NaCl with 1% concentration at room condition increases the surface tension of an aqueous solution by 0.17 mN/m. In contrary, if the cohesive attractive forces between water molecules are greater than their attraction to the solute molecules, then the solute molecules are pushed towards the solution surface where they accommodate more easily. As a result, the surface tension of the solution reduces. Many organic solutes, in particular, detergents (or surfactants) exhibit this effect.

Surface tension of a liquid can be measured by a simple experiment, as shown schematically in Fig. 2.1. The U-shaped wire is plunged into a bulk of liquid and then lifted up. Thus the liquid film inside the U-shaped frame is created. Some masses are placed on the weighing pan B in order to balance it. At this point, when the film is intentionally ruptured, the balance will go down by the B side. The equilibrium can be reached by putting some masses on the side A. The value of these last masses corresponds to the force with which the film tends to close into the liquid. The surface tension is calculated by the force F divided by the width of the film W. The reason for the factor $1/2$ is because the film has two sides, each of which contributes equally to the force. The surface tension can thus be expressed as

$$\sigma = \frac{F}{2W} = \frac{F\Delta x}{2W\Delta x}. \tag{2.1}$$

Note that the second term on the right side of Eq. 2.1 corresponds to the energy needed to move the frame a small step Δx away from the bulk liquid in order to create more film area.

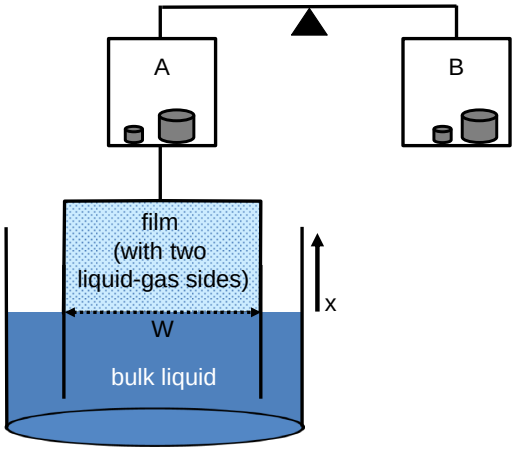

Figure 2.1: Schematic of a simple experiment to measure the surface tension of a liquid.

2.1.2 Contact Angle

When a liquid drop is positioned on a solid substrate surface, between the solid-liquid ($s\ell$) interface and the liquid-gas (ℓg) interface an angle will be formed, which is referred to as the equilibrium (or static) contact angle θ. Two approaches are commonly used to describe the equilibrium contact angle on (smooth and chemically homogeneous) planar surfaces: a force balance

formulation and an interfacial free energy minimization [65]. The former approach regards interfacial tensions as forces required to create a unit length. Hence, the force balance at the contact line of a drop, which takes the shape of a circle under equilibrium condition, requires the sum of the force vectors acting outward and tangential to the solid surface to be equal to counteracting cohesive and viscous forces. The free energy minimization approach considers interfacial energy as energy required to create a unit area, and then calculates changes in surface free energy due to infinitesimal displacement. No matter which approach is used the result is identical, yielding the Young's relation [66]:

$$\sigma cos\theta + \sigma_{s\ell} - \sigma_{sg} = 0. \tag{2.2}$$

The equilibrium contact angle is therefore determined by

$$cos\theta = \frac{\sigma_{sg} - \sigma_{s\ell}}{\sigma}. \tag{2.3}$$

The number $cos\theta$ is called the wetting coefficient of the liquid. Liquids that are attracted to solid surfaces (adhesion) more strongly than to other liquid molecules (cohesion) result in a small contact angle, i.e. $\theta < 90°$. These solid surfaces are called hydrophilic. In contrast, when the cohesive force of the liquid is larger than the adhesive force, the liquid repels the solid and θ is larger than 90°. Such solid surfaces are called hydrophobic.

The definition of contact angle presented here is for the situation where the liquid is static. The contact angle formed between a $flowing$ liquid (advancing or receding) and a solid surface is called dynamic contact angle. The value of the dynamic angle is not constant during flow and it depends on the interplay between capillary and viscous forces [67].

2.2 Interface Curvature and Capillary Pressure

Consider two immiscible fluids, liquid water w and a gas g, in a vessel. At hydrostatic equilibrium and in the absence of body forces, the pressure p_w and p_g, respectively, must be constant for each fluid, i.e. $\Delta p_w = \Delta p_g = 0$. The stress balance at the liquid-gas interface yields the Young-Laplace equation:

$$p_g - p_w = 2\sigma\kappa, \tag{2.4}$$

where κ denotes the local mean curvature of the liquid-gas interface. It can be calculated as

$$\kappa = \frac{1}{2} \nabla \cdot \mathbf{n}_w, \tag{2.5}$$

where $\mathbf{n}_w$ denotes the unit normal vector field on the boundary of the liquid phase domain, pointing out of the liquid phase (which must be constant at hydrostatic equilibrium). Since p_w and p_g are constants, so is the mean curvature of the interface, κ. In differential geometry, the mean curvature is the reciprocal of the radius of the mean curvature R. For a simple geometry of the vessel containing fluids, R and κ can readily be computed. For example, suppose that the vessel is a cylindrical tube of small radius (a capillary), see Fig. 2.2. The meniscus in this tube takes the shape of spherical cap, which satisfies the condition of constant mean curvature. The radius of this spherical cap is computed from the equilibrium contact angle, given by Young's relation (Eq. 2.3), and the capillary radius r, as

$$\kappa = \frac{1}{R} = \frac{cos\theta}{r}. \tag{2.6}$$

According to this equation, the radius of mean curvature R depends on the equilibrium contact angle θ between liquid and the solid wall as well as on the radius of the capillary tube r. On this basis, the mean curvature can be eliminated and the capillary pressure p_c can simply be expressed by the capillary tube radius, the equilibrium contact angle and the surface tension, namely

$$p_g - p_w = p_c = \frac{2\sigma cos\theta}{r}. \tag{2.7}$$

In general, the contact angle of water on clean glass is small, and for mathematical convenience it is often assumed to be $\theta = 0°$ (perfect wetting). For a flat interface ($r \to \infty$) the capillary pressure is nonexistent.

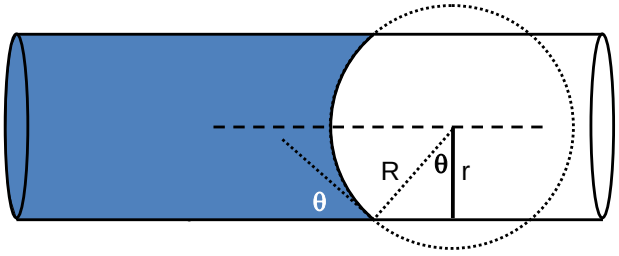

Figure 2.2: Liquid-gas interface confined in a capillary tube with hydrophilic solid surface.

In a partially saturated porous medium with uniform wettability, the value of capillary pressure varies, depending on the saturation and the direction of saturation change which can essentially occur in two ways: Drainage (or drying) that refers to the decreasing saturation of a wetting phase. And,

imbibition (or wetting) that refers to the increasing of wetting-phase saturation. The capillary pressure increases with decreasing the saturation, whereas it decreases with increasing the saturation. The capillary pressure relationships for the drainage and imbibition can differ significantly. This difference is called the capillary pressure hysteresis. Capillary pressure can be positive or negative, depending on wettability and history of fluid displacement: The capillary pressure values are positive for strongly wetting and negative for strongly non-wetting conditions. A negative capillary pressure value pulls together the pore wall that is restraining the liquid. This may lead to a considerable volume deformation of highly disperse systems and porous bodies, or capillary contraction. Thus, for example, the rise in capillary pressure that takes place during drying may lead to considerable shrinkage in capillary porous materials. A positive capillary pressure acts like a valve on the fluid flow, however.

2.3 Capillary Action

In a tapered capillary tube partly filled with a wetting fluid (see Fig. 2.3), the liquid-gas interfaces inside the tube are curved. This fact gives rise to the capillary pressure by which the pressure in the liquid is lowered. Since the gas pressure above these interfaces is constant and equal, the liquid-pressure difference is given by

$$p_{w1} - p_{w2} = p_{c2} - p_{c1} = \frac{2\sigma cos(\theta_2 + \phi)}{r_2} - \frac{2\sigma cos(\theta_1 + \phi)}{r_1}, \qquad (2.8)$$

where ϕ denotes the opening half-angle of the capillary tube. Since the capillary pressure p_{c1} is lower than p_{c2} and hence the liquid pressure $p_{w1} > p_{w2}$, the liquid displaces towards the right meniscus (with shorter radius of curvature) until a new equilibrium state is reached. This effect is referred to as the capillary action or capillary pumping. This effect is only noticeable in small-diameter capillary tubes where body forces are small compared to surface tension forces. Such a situation occurs when the tube is positioned horizontally. However, if this tube is rotated anticlockwise by 90°, the liquid moves vertically downwards due to gravity forces.

2.4 Capillary Rise

When a capillary tube of small cross section is inserted into a water bath, the water creeps upward along the tube wall. A curved meniscus is thus created

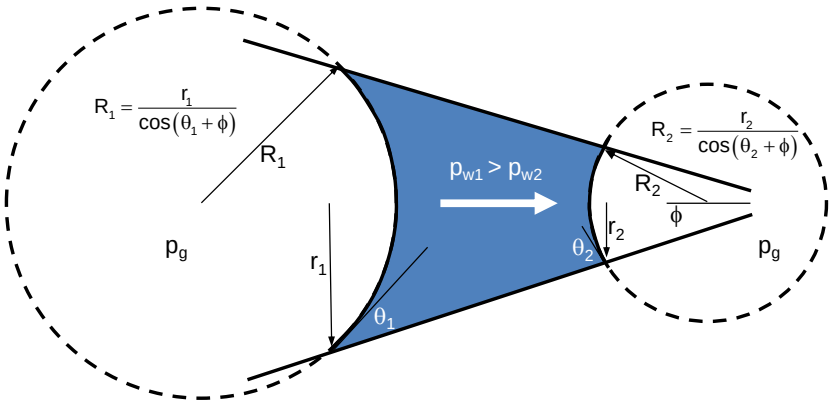

Figure 2.3: Schematic of capillary pumping in a small tube tapered slightly at one end.

whose surface area is larger than the cross-section area of the tube. This enlargement of the curved area is opposed by the surface tension of the water, thereby the water is pulled farther up into the tube. These processes continue from higher level, causing the water to continue rising. The equilibrium height of the capillary rise h in a cylindrical tube of radius r results from the force balance between the capillary force F_c and the gravitational force

$$F_c = p_c \pi r^2 = M_w g = \rho_w h \pi r^2 g, \tag{2.9}$$

where M_w, ρ_w, and g denote the liquid mass, the liquid mass density, and the acceleration of gravity, respectively. Invoking Eq. 2.7, the equilibrium height of the column of liquid is given by

$$h = \frac{2\sigma cos\theta}{r \rho_w g}. \tag{2.10}$$

For water at 20°C in a (soda-lime) glass capillary with $cos\theta = 1$, Eq. 2.10 simplifies to $h(mm) = 15/r(mm)$. Note that if $\theta > 90°$, the capillary rise will be negative, meaning that the molecules of the liquid are more strongly attracted to each other than to the surface. This is readily seen with mercury in a glass container, in which the meniscus is upwardly convex instead of concave.

The mechanism of capillary rise in tubes filled with particles is shown in Fig. 2.4. The pressure at the liquid side of the interface is lower than atmospheric pressure. This pressure difference causes liquid to rise into the capillary medium until the upward capillary force is exactly balanced by the weight of the liquid column, and the system reaches mechanical equilibrium. In the capillary tube with fine particles, small pores can pump water to

distance higher than that in the tube filled with coarse particles ($h_1 > h_2$). At the interface between the fine particle layer and the coarse particle layer big pores serve as barriers and hence they halt further water uptake into the tube (right tube shown in Fig. 2.4). In real porous media the rise height can be of the order of meters depending on the typical pore size.

An excellent treatise on capillarity and the phenomena resulted from this effect can be found in [68].

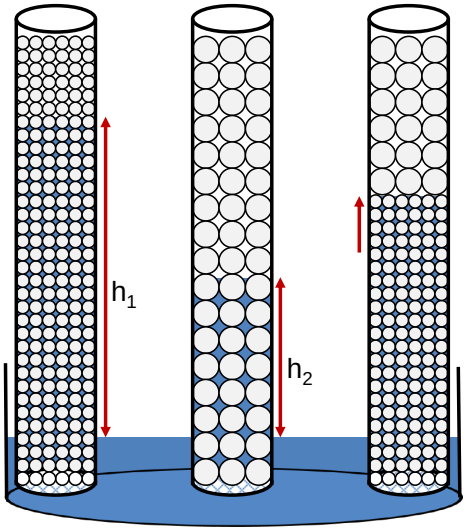

Figure 2.4: Capillary effect illustrated schematically in three small tubes with identical diameter. These capillaries are packed with fine particles (left), coarse particles (middle), as well as a layer of fine particles together with a layer of coarse particles (right).

2.5 Kelvin Effect

In a container filled partly with a liquid and partly with respective vapor at a given temperature, the equilibrium pressure is called the saturation vapor pressure p_v^*. This definition does not require the presence of any other gas molecules in the gas phase. The thermodynamic equilibrium vapor pressure above a *flat* free water-air interface is assumed to be p_v^* at a given temperature. However, the equilibrium vapor pressure in a confined pore space is reduced by the meniscus curvature and thus by the pore radius (see Fig. 2.5). In other words, water vapor molecules in the gas phase above the *curved* interface in the pores are more likely to condense than over a flat water-air interface. This reduction of vapor pressure above the (concave) curved

meniscus of interface is referred to as Kelvin effect and can be described by [69]

$$\frac{p_v}{p_v^*} = exp(-\frac{\widetilde{M}_v}{\widetilde{R}T}\frac{p_c}{\rho_\ell}). \tag{2.11}$$

Assuming that the pore is cylindrical and the pore inner surface is perfectly wetted with liquid ($cos\theta = 1$) results in

$$\frac{p_v}{p_v^*} = exp(-\frac{\widetilde{M}_v}{\widetilde{R}T}\frac{2\sigma}{\rho_\ell r}). \tag{2.12}$$

This equation is known as the Kelvin equation. As can clearly be seen in this equation, the reduction of vapor pressure is only important for capillaries of very small radius, say less than one micrometer. This reduction can lead to the vapor condensation in pores. The radii of pores up to which can be filled by this capillary condensation mechanism depends on the relative humidity of the surrounding gas (see Fig. 2.5). For a relative humidity of 80% wet air fills pores with radii smaller than 5 nm through capillary condensation, for instance. Note that the vapor pressure lowering can also be caused with

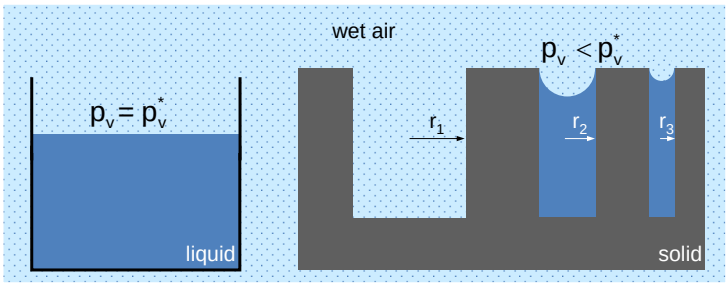

Figure 2.5: Illustration of the equilibrium vapor pressure above a flat free water surface and above curved interfaces inside pores of different radii. Small pores are filled with liquid by capillary condensation. Big pores can be filled at a high relative humidity of the gas phase.

solution of salts or gases in a pure liquid. On the other hand, the equilibrium vapor pressure at a convex interface inside a capillary tube is larger than the saturation vapor pressure at a flat interface. In this case, the sign $(-)$ in Eq. 2.12 changes to $(+)$. Note that the equilibrium vapor pressure at the surface of a liquid droplet is lower than the saturation vapor pressure, because liquid molecules are not bonded to each other and thus evaporation is favored. The vapor pressure inside a bubble is also lower than the saturation vapor pressure, because liquid molecules are strongly attached to each other and hence evaporation occurs hardly.

2.6 Sorption Isotherm

A sorption isotherm provides the residual moisture content (or the equilibrium moisture content) of a solid X as a function of the relative humidity of the agent that surrounds the solid. The relative humidity is defined as the ratio of the actual vapor pressure to the saturation vapor pressure at given temperature T, namely

$$\varphi = \frac{p_v}{p_v^*(T)}. \tag{2.13}$$

Figure 2.6 shows the typical curve of sorption isotherm. As can be seen, the moisture content seems to approach a plateau (shown by dashed line) when the relative humidity increases. This regime corresponds to the situation where the water vapor molecules occupy the inner surfaces of the solid material. Langmuir model can be used to describe the behavior of the sorption isotherm in this regime. Note however that this plateau is not usually reached because of the building up of multiple layers of water molecules on the inner surfaces of the pores. This regime is referred to as multimolecular adsorption and can be described mathematically by BET model. By further increasing vapor pressure, a continuous film of liquid forms in the pores. As a result, the vapor pressure in the small pores reduces due to the curved water surface and capillary condensation takes place (see Sec. 2.5). Sorption isotherm curves are determined experimentally and essentially constitute the fingerprint of a solid system [70].

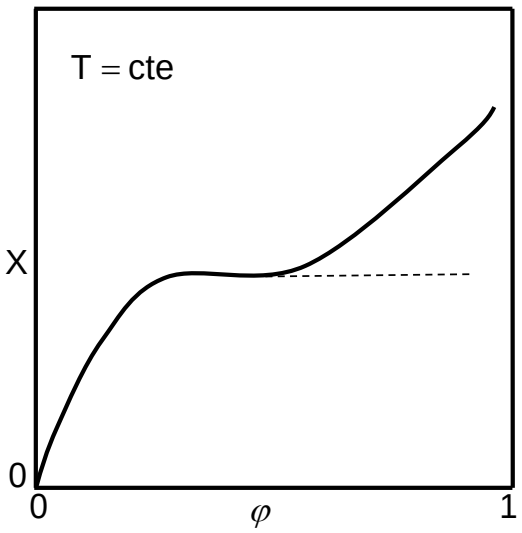

Figure 2.6: Typical sorption isotherm.

Chapter 3

Direct Imaging of Pore-scale Phenomena in Porous Media

Two visualization techniques are applied to monitor drying, wetting, and two-phase flow (i.e. drainage and imbibition) characteristics of three different experimental model systems: (i) packed beds are filled with a single layer of real glass beads resulting in pseudo-two-dimensional transparent single and dual cells. These cells are often called Hele-Shaw particle packing. The dual cells are comprised of two connected regions filled with: small and large, hydrophilic and hydrophobic, individual and sintered particles, respectively. Each of these cells is exposed to convective drying under controlled conditions. Two-dimensional video images of the drying cells are acquired by an optical shadowscopy technique, and wet and dry regions are determined from the images. Drying curves associated to both types of cells are yielded after post-processing of the corresponding data. (ii) Pseudo-two-dimensional transparent micromodels are fabricated from either Polydimethylsiloxane (PDMS) or silicon dioxide. Optical photography is used to acquire the real-time fluid distributions within these micromodels. (iii) A three-dimensional random packing of real glass beads is another model system considered in this study. In this system the dynamics of the drying process is obtained from high-resolution images which are acquired using an X-ray microtomograph. The quantification of the results obtained from these model systems provides valuable information that can enhance the understanding of pore-scale transport phenomena in real complex porous media. At last, the structural properties of fibrous substrates are determined from X-ray tomograms.

3.1 Optical Measurement of the Drying Process

3.1.1 Hele-Shaw Cells

Figure 3.1 shows schematic illustration of two-dimensional single and dual cells of aspect ratio 1 with three sides insulated and top side exposed to air for drying under a controlled condition (directional drying). Each dual cell is divided into two distinct regions arranged vertically and filled with: (i) small and large, (ii) hydrophilic and hydrophobic, and (iii) individual and sintered glass-bead particles. The cells were initially saturated with distilled water. The dry air was supplied at ambient temperature with a constant flow rate 0.65 m^3/h in all experiments. Gravity effects have been minimized in all experiments by placing the drying cell horizontally on the sample holder. Figure 3.2 describes the experimental setup used for studying the particle packing drying. The optical shadowscopy technique is used, in which the cell is placed between a CCD camera and a white plane illuminated by two LED lamps. Images of the cell captured during drying were stored in a computer. The air temperature was monitored with the help of a thermocouple and was found to be 22.5 °C during the experiments.

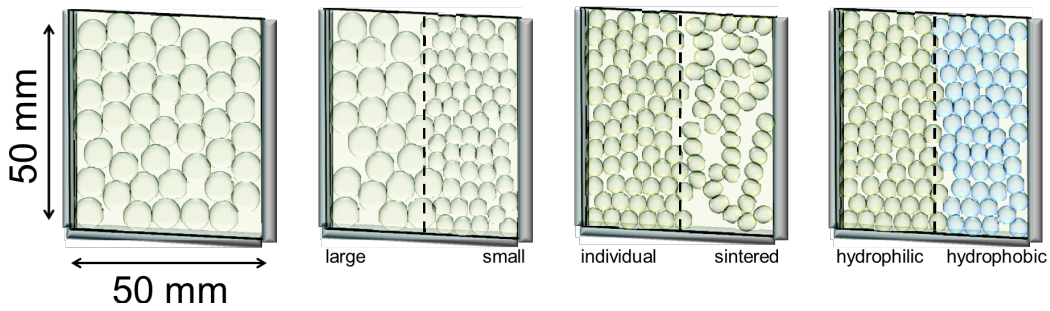

Figure 3.1: Schematic illustrations of a single cell and dual cells filled with small-large, individual-sintered, and hydrophilic-hydrophobic glass beads [B].

As shown in Fig. 3.3, a sequence of image processing steps using Matlab's built-in functions has been developed to discriminate the wet and dry regions and to calculate the liquid saturation from the raw gray values. Note that close matching of the refractive index of water and glass beads allows monitoring the progress of drying. In this study, the refractive index of soda-lime glass beads was 1.52, and 1.33 for water. These refractive indices are not matched well enough so that the glass beads are visible in water. As air

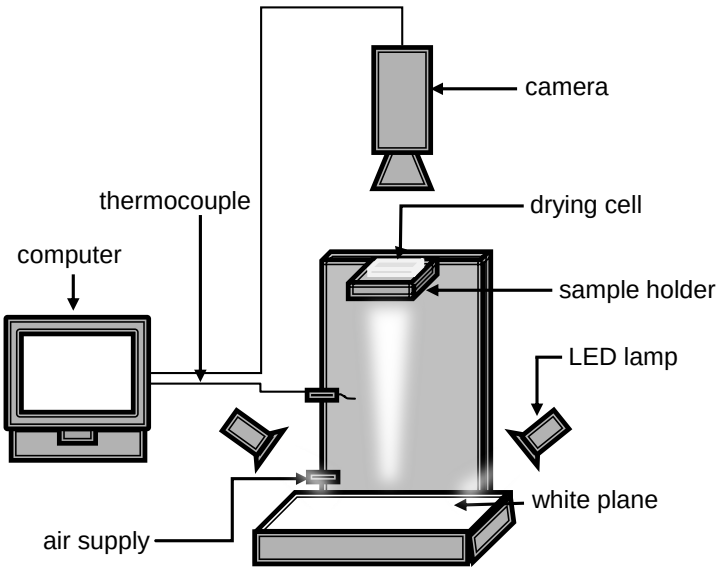

Figure 3.2: Schematic illustration of the shadowscopy setup [B].

invades the particle packing during drying, the borders of the glass beads become optically thicker enabling the identification of dry and wet regions (see Fig. 3.3a). The following algorithm was used to process the gray value images: First, the images were cropped to display only the region containing the glass beads. Then the gray level images were binarized to produce black and white images, by choosing an appropriate threshold value from the gray-level histograms (see Fig. 3.3b). Connected components (objects) in the binary image with fewer white pixels than a predefined threshold were removed. Thus a new binary image was produced, in which the dry region – displayed in black region in Fig. 3.3c – was clearly identified. A morphological close operation (i.e. a dilation followed by an erosion) was then performed on the binary image to segment it into white (wet) and black (dry) regions (see Fig. 3.3d). After color inversion (Fig. 3.3e), the raw and inverted images were combined (see Fig. 3.3f). The liquid saturation S is estimated from the inverted image (see Fig. 3.3e) by dividing the number of black pixels by the total number of pixels in the image; in this example S = 0.77. Note that liquid films cannot be detected by this shadowscopy imaging technique used here and saturations are therefore “apparent” ones, since they do not include all pore water.

Results of drying experiments with a single cell filled with primary glass beads and with dual cells packed with particles of different size distributions and wetting properties are presented here. All particle packings were fully

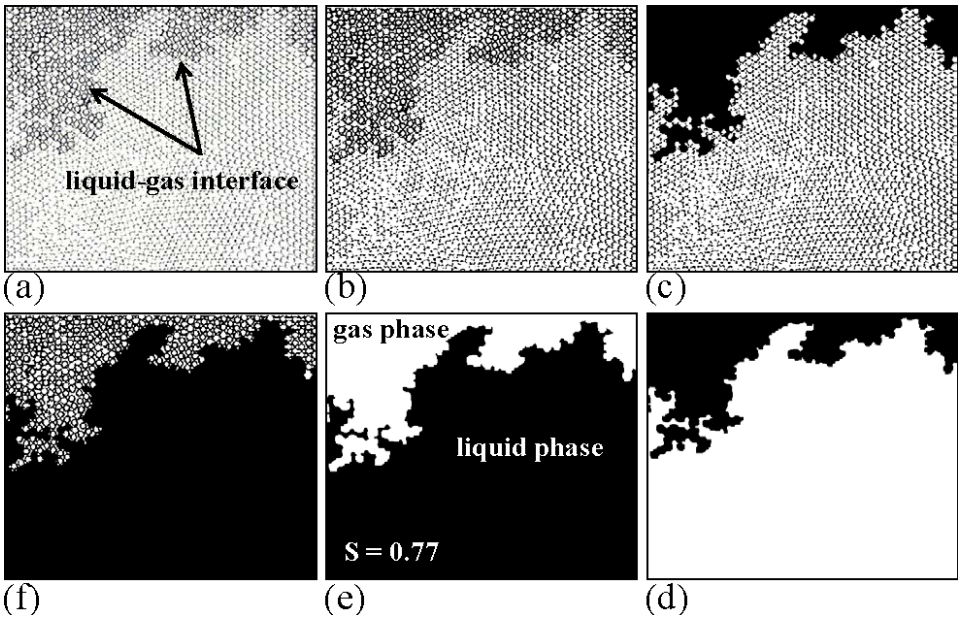

Figure 3.3: Image processing steps: (a) raw gray-value image, (b) binarization, (c) removal of small white objects in the dark region, (d) morphological close operation, (e) inversion and (f) combine (b) and (e). The drying cell is subjected to evaporation at the top and the other sides are sealed [B].

saturated initially, and at room temperature and atmospheric pressure. Liquid evaporation occurred only at the top of particle packing; the remaining faces were impervious to fluids. During the drying process images of the cell were acquired and stored in a computer. Phase distributions over time as well as drying curves determined from the sequence of processed images are presented in this section.

Single drying cell: The first experiment was performed with a single cell packed with particle size diameter 1.25-1.55 mm. Figure 3.4 shows phase distributions of the particle packing at four different liquid saturations. The corresponding drying curves are computed from the sequence of processed images using total variation regularization [71] and shown in Fig. 3.5. As shown in Fig. 3.4, the liquid is transported to the evaporation surface by upward capillary flow during the drying process and is removed continuously via evaporation. As the liquid saturation decreases further, the capillary flow is disrupted and the liquid phase splits up into clusters. Similar results have also been observed in irregular pore network simulations [72]. This drying experiment exhibit a long 1st drying period (constant rate) down to very low values of the "apparent" saturations (see Fig. 3.5). This is probably due to

film flow along the straight walls [73].

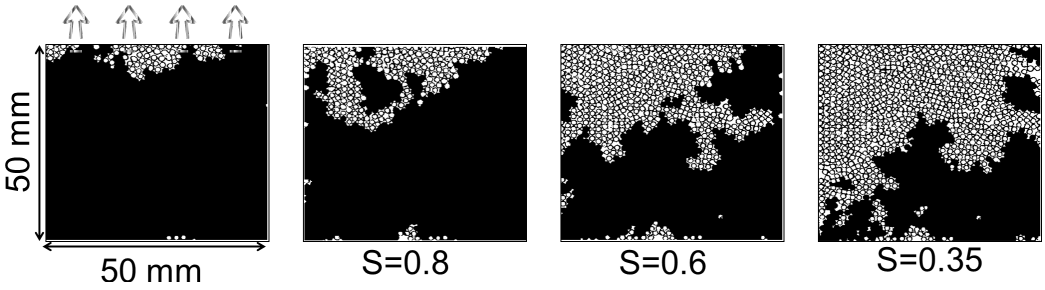

Figure 3.4: Evolution of phase patterns during drying in a single cell [B].

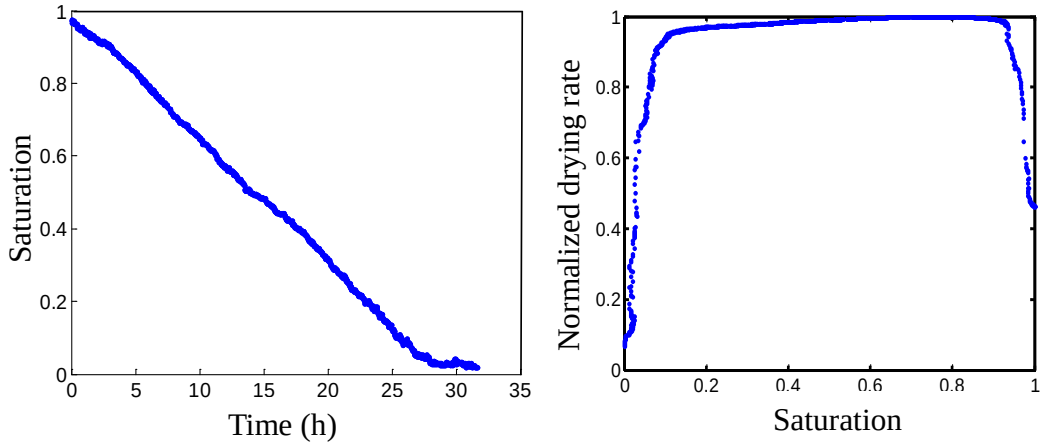

Figure 3.5: Drying curves for a single cell [B].

Dual drying cell: small and large particles: The drying experiment with a dual cell filled with particles of size 1.25-1.55 mm and 0.55-0.65 mm, respectively, is presented here. Figure 3.6 shows the evolution of phase distributions during drying; the corresponding drying curves for each side of the drying cell are displayed in Fig. 3.7. Figure 3.6 indicates that the large particle region is first invaded by air, which is due to low capillary pressure supplying the small particle region with liquid. The large particle region dries out from the left side which is probably due to a loose parallel alignment of the glass plates when two particle sizes are used. Pore network simulations with similar structures are reported in [74]. Figure 3.7 shows the drying curves for each side in this dual cell. One can see that the large particle region acts like a passive valve providing the small particle region with water.

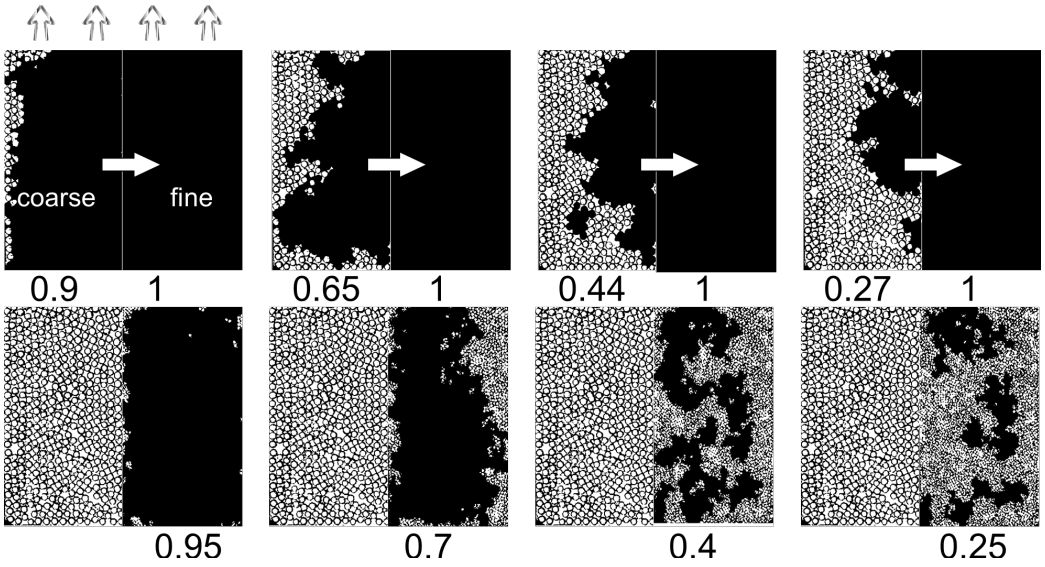

Figure 3.6: Evolution of phase patterns during drying in a dual cell filled with small (right half) and large (left half) particles. Both regions are simultaneously exposed to drying from the top edge. Liquid saturation is given below the images. (Capillary flow is indicated by arrows) [B].

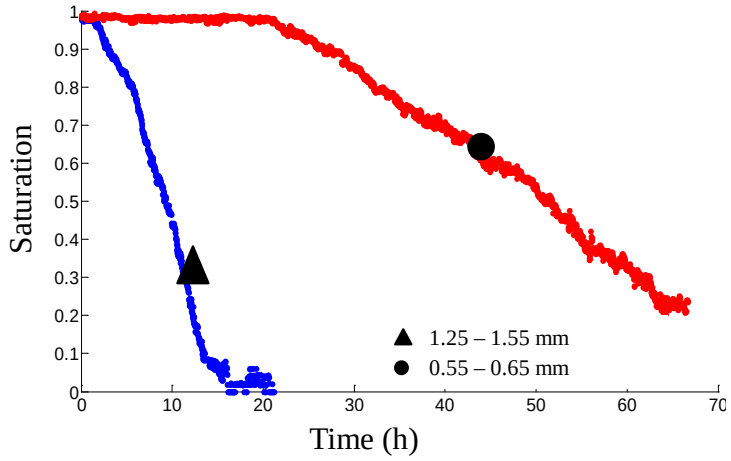

Figure 3.7: Drying curves for each side a dual cell filled with small and large particle regions [B].

Dual drying cell: hydrophilic and hydrophobic particles: Drying experiments were also performed with particles of different surface wettability. Both hydrophilic and hydrophobic glass beads were used with a diameter

range of 0.95-1.05 mm. The originally hydrophilic (HI) glass beads were treated and rendered hydrophobic (HO) following a recipe, presented in [75]. The equilibrium contact angle of water with the particle surface was determined from micro-photographs of a glass bead in contact with a droplet over it. The equilibrium contact angles measured for hydrophilic and hydrophobic particles were about 50° and 105°, respectively. A vacuum pump was used to remove trapped bubbles of air ensuring a complete initial saturation of the HO packing. Figure 3.8 shows the evolution of phase distributions for both HO and HI particle regions that were simultaneously exposed to drying from the top edge. Corresponding drying curves are illustrated in Fig. 3.9. The results indicate that liquid pores in the HO region are invaded by air first while providing liquid to the HI region. Liquid clusters are more compact in the HO region. The two glass plates confining the particle packing were not hydrophobized, so that liquid films were probably not fully suppressed.

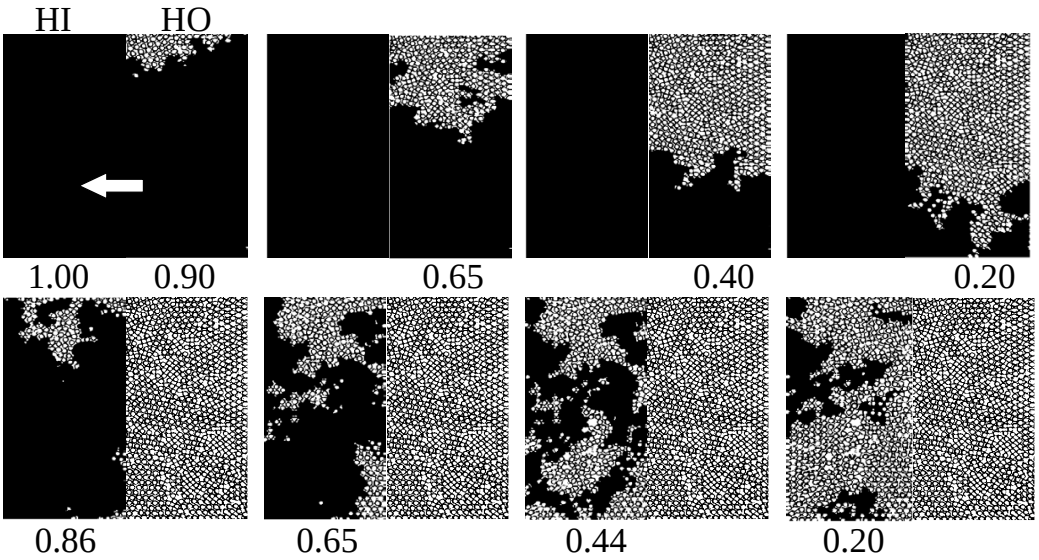

Figure 3.8: Evolution of phase distributions during drying of hydrophobic (HO) and hydrophilic (HI) particle packings in a dual cell. Drying is from the top edge and liquid saturation is given below the images [B].

Dual drying cell: individual and sintered particles: Highly porous model aggregates were prepared by sintering glass beads in a graphite mold. The sintering was performed in an oven at 600°C for 7 minutes. These conditions are chosen depending on the type of glass used: the temperature must exceed the glass transition limit but remain below the crystallization point [b]. The sintered particle structures were then used to create a highly porous

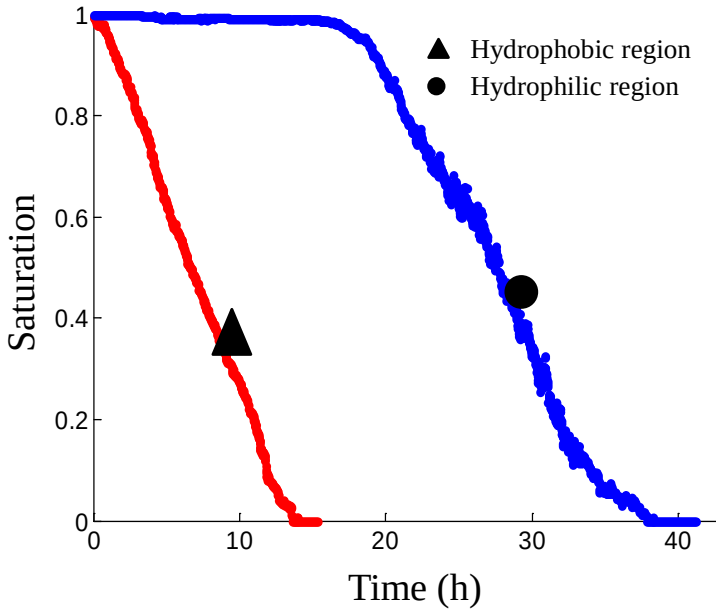

Figure 3.9: Drying curves for a dual cell filled with hydrophobic and hydrophilic regions [B].

packing region in a dual drying cell. Figure 3.10 shows the evolution of phase distributions during drying; the corresponding drying curves are depicted in Fig. 3.11. These results indicate that the large pores located in the highly porous region are invaded by air first while liquid is supplied to the dense region by capillary flow.

3.1.2 Micromodels

Micromodels are pseudo-two-dimensional networks that serve as representation of normally-opaque capillary porous media. These model systems are typically fabricated from materials such as glass, silicon, quartz, polymethylmethacrylate (PMMA) or polydimethylsiloxane (PDMS). These materials are transparent and thus provide the possibility to observe optically the fluid structure, the transient fluid dynamics and the solute transport within the sub-millimeter sized pores. These pores must be small, otherwise the capillary effects will be irrelevant. Most micromodels have an overall size of few centimeters and they are manufactured by several different synthetic methods, such as optical lithography, stereo lithography, soft lithography, wet, dry, and laser or plasma etching. The use of these manufacturing methods depend on the material type. Details of the manufacturing process can be found elsewhere, e.g., see [76, 77]. The micromodels utilized in our research

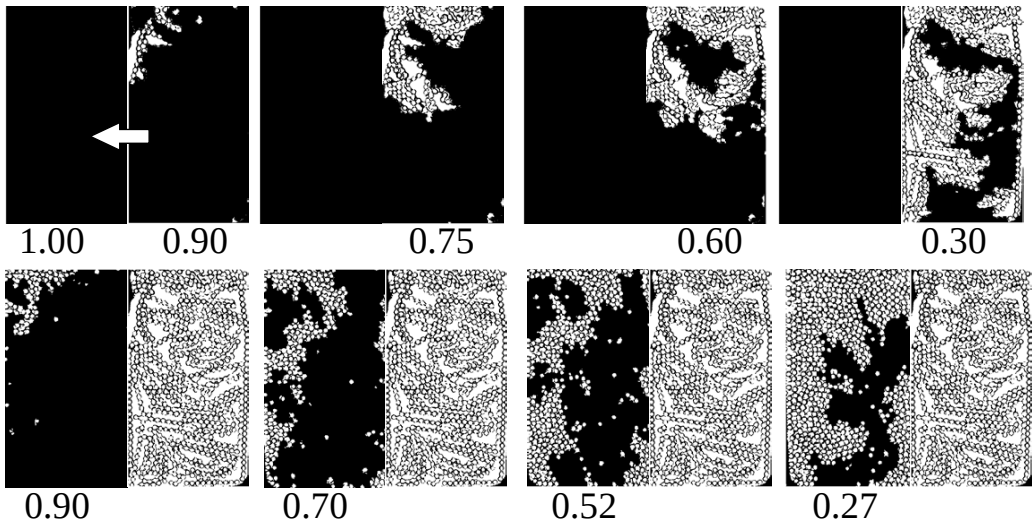

Figure 3.10: Evolution of phase distributions during drying of individual and sintered particle packings in a dual cell. Drying is from the top edge and liquid saturation is given below the images [B].

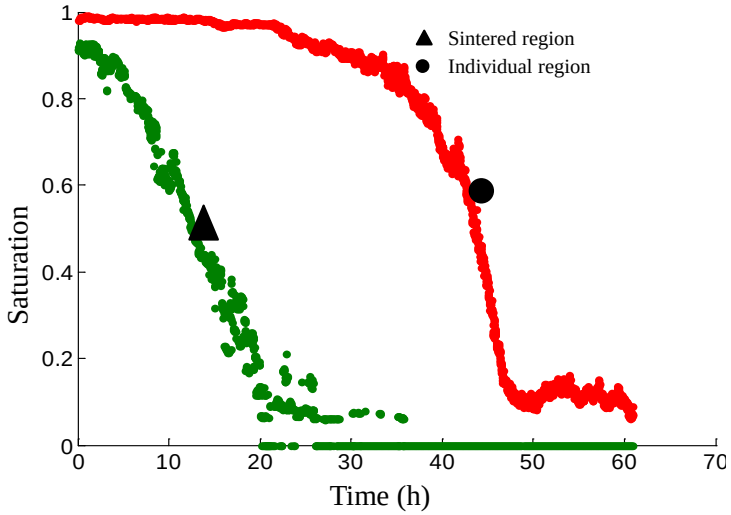

Figure 3.11: Drying curves for a dual cell with individual and sintered regions [B].

projects are made of PDMS or silicon-glass. Each type of these micromodels has their own pros and cons. PDMS micromodels are cheap because they can be manufactured fast in a normal laboratory. However, a master wafer, on which the flow network is formed has to be made in a clean room. This

wafer can be used later for manufacturing several micromodels in a normal lab. Though PDMS micromodels are easy and cheap to construct, fluids in their channels may permeate through the surrounding layer or they may react with the channel walls and the properties of the flow network may thus be altered. For the fabrication of silicone-glass micormodels a well-controlled clean room is required, thereby they are expensive. The high cost for their production is however compensated by the accuracy and roughness of the channels.

Figure 3.12 shows the visualization system which is used to acquire two-dimensional images from the top cover of the micromodels. From these images the average liquid saturation is tracked over time, resulting in process kinetics. This system is comprised of components which are almost identical to those of the shadowscopy setup (see Fig. 3.3). The main difference between these two setups is that the micromodels are illuminated by LED lamps which are placed *above* them. This setup is employed to conduct drying, two-phase flow, and wetting experiments. An overview of the PDMS micromodels used for the drying and two-phase flow visualization experiments is provided in Fig. 3.13. The small dimension of these micromodels allows to track the fluid displacement process in every single pore or throat. For wetting experiments, a silicon-glass micromodel is utilized, see Sec. 3.2. Note that in all experiments micromodels are placed horizontally in order to avoid the effects due to gravitational forces.

The PDMS micromodels consist of square pores and rectangular throats. As can be seen in the zoomed image in Fig. 3.14, four small throats are interconnected to a larger pore with a sharp geometrical expansion at their interfaces. The fluid-fluid-interface displacement in a micromodel with such a pore-throat geometry is optically tracked during the capillary-dominated drainage and imbibition processes. In these experiments, an invading fluid is injected into the micromodel by using a syringe pump. The rate of fluid injection is set to 0.1 μl/min, resulting in a low capillary number (Ca $\approx$ 10^{-8}). This low value of the capillary number indicates that the flow in the micromodel is dominated by capillary forces. Note that the capillary number, which is the ratio of viscous forces to capillary forces, is defined as $Ca = \eta u/\sigma$, where η and u denote the dynamic viscosity and the velocity of the invading fluid, respectively, and σ the surface tension or interfacial tension between the invading and displaced fluids. This number is constant in forced imbibition, whereas it varies during the spontaneous imbibition process. The fluid flow in porous media is driven by capillary forces if the capillary number is small, a rule of thumb says less than 10^{-5}.

In the (primary) drainage measurement (Fig. 3.15), the invading and displaced fluids are water (non-wetting fluid) and air (wetting fluid), respec-

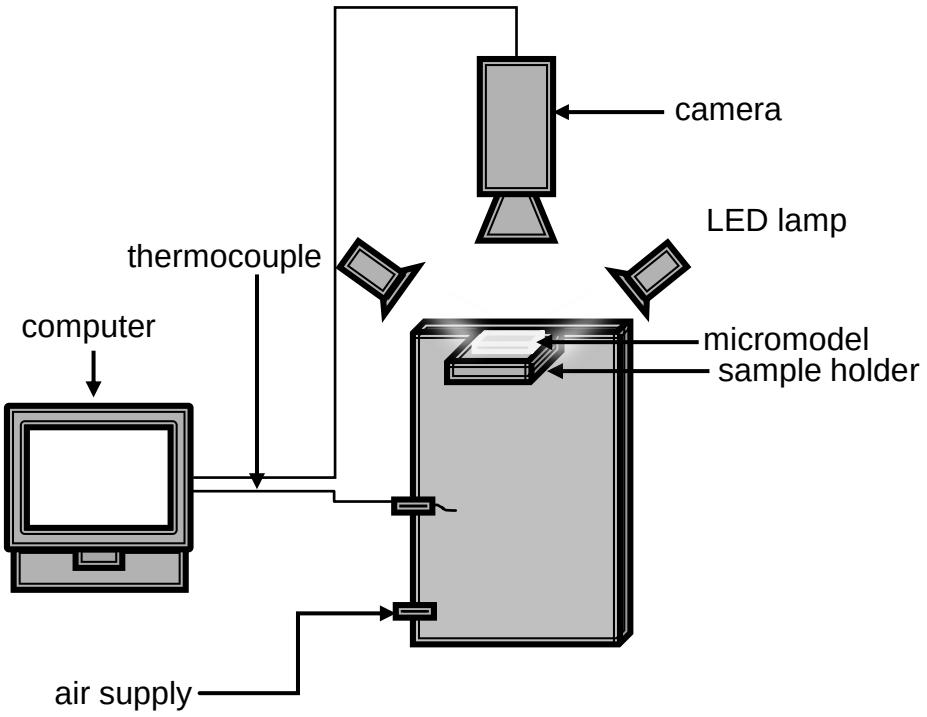

Figure 3.12: Schematic illustration of the photography setup.

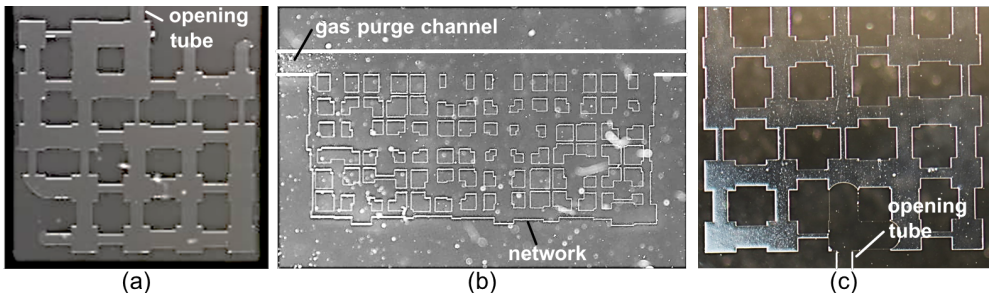

Figure 3.13: PDMS micromodels used for drying (a-b) and two-phase flow (c) experiments.

tively. These fluids create an advancing contact angle of about $\theta_a = 67°$. The equilibrium contact angle θ remains equal to the advancing contact angle as long as the meniscus – and contact line – moves along the throat walls. It however varies when the invading fluid crosses the pore-throat interface. When the meniscus reaches the pore-throat interface the contact angle increases to $\theta = \theta_a + 90°$ and the three-phase contact line immobilizes. With further invasion of the water, the meniscus grows and the equilibrium con-

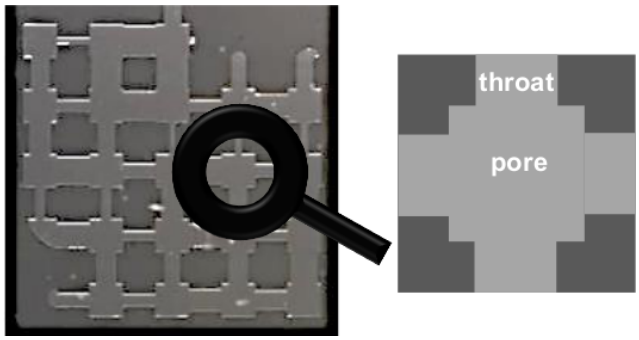

Figure 3.14: Schematic illustration of a pore and its four neighboring small throats in the PDMS micromodel.

tact angle decreases, i.e. $\theta = \theta_a$ and the radius of the meniscus curvature increases. Thus the pressure difference across the meniscus becomes lower than that when the meniscus was in the throat (Fig. 3.16). This action of the fluid invasion into a large pore from its neighboring throat is called burst invasion. Such sudden expansion of a pore cross-section that leads to an increased resistance to the advancement of the invading fluid is referred to as capillary valve effect.

In the (primary) imbibition experiment (Fig. 3.15), the invading fluid is a mixture of water (20% v/v) and alcohol (80% v/v) (wetting fluid) and the displaced fluid is air (non-wetting fluid). The meniscus created at the interface between these two fluids results in an advancing contact angle of about 103°. Similar to the drainage experiment mentioned above, the burst invasion event is observed when the meniscus invades the pore from one of its neighboring throats.

Figure 3.17 shows the time evolution of the invading fluid in a pore and its neighboring throats. During the drainage process, a meniscus refrains from displacement when it reaches the entrance of a pore. At this time the pressure of the invading fluid increases that results in movement of the menisci in the throats neighboring to this pore. These menisci, which are attached to a common pore, grow together until they touch each other. This type of pore invasion is called merge invasion. Both the burst and merge invasion events may occur during the drainage, the imbibition or the drying process. Bear in mind that the initial forces that drive the invading fluid into these micromodels during the drainage and imbibition processes are purely mechanical. Therefore, the burst and merge events have mechanical origin. This situation however is completely different in drying; these events are originated by evaporation, a non-mechanical driving force. These interface-scale events can influence the dynamics of these processes as presented hereafter.

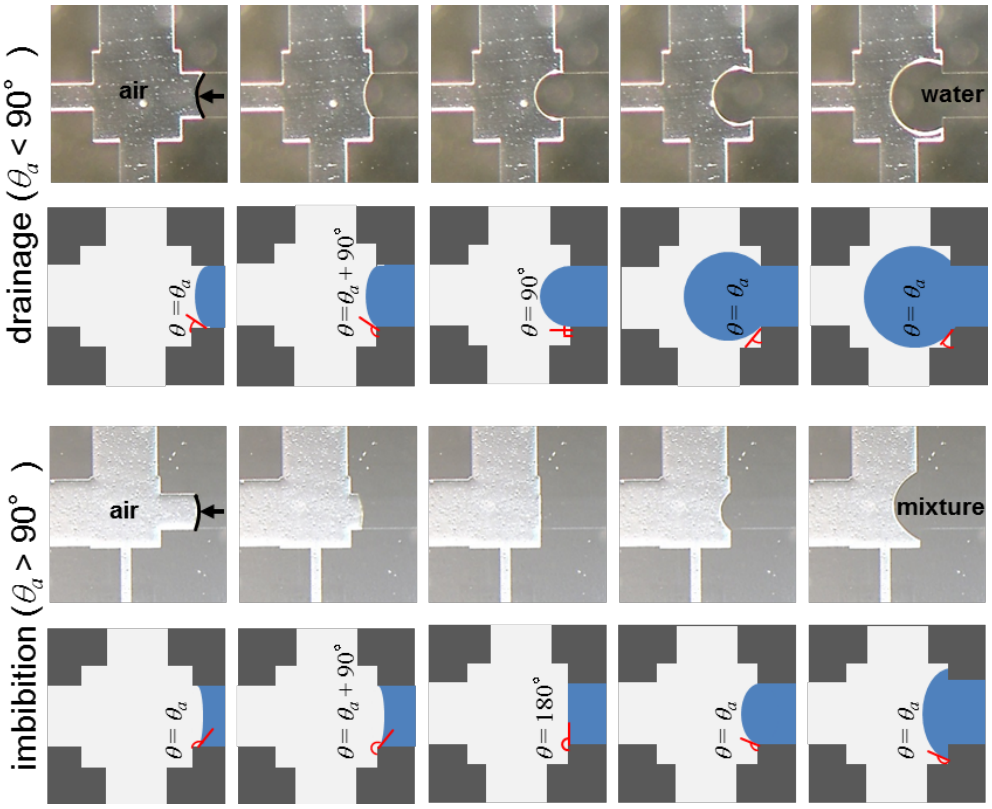

Figure 3.15: Burst invasion during the drainage and imbibition processes. The time sequence of images is from left to right [C].

For drying experiments the small micromodel shown in Fig. 3.13a is used, which is made of 5×5 pores with a side length of 1 mm. The distance between the centers of two neighboring pores is 2 mm. The throat widths are uniformly distributed in the range of [0.14-0.94] mm with an interval of 0.02 mm. The micromodel sides are sealed except the middle pore at the top. This pore is connected to the surrounding environment via a tube of 8 mm length and 0.5 mm width. This special type of boundary condition is applied in order to retain the drying rate low. Under this condition the liquid displacement is dominated by capillary forces. All the pores and throats including the tube have a depth of 0.1 mm. Initially the micromodel is fully saturated with water. Figure 3.18 shows the evolution of the phase distribution in the micromodel during drying. As can be seen, the gas phase preferentially invades the throats and pores in the micromodel. In this micromodel all throats are smaller than the pores. Therefore one would expect that when a throat in a liquid cluster is invaded by the gas phase, its neighboring pore would be emp-

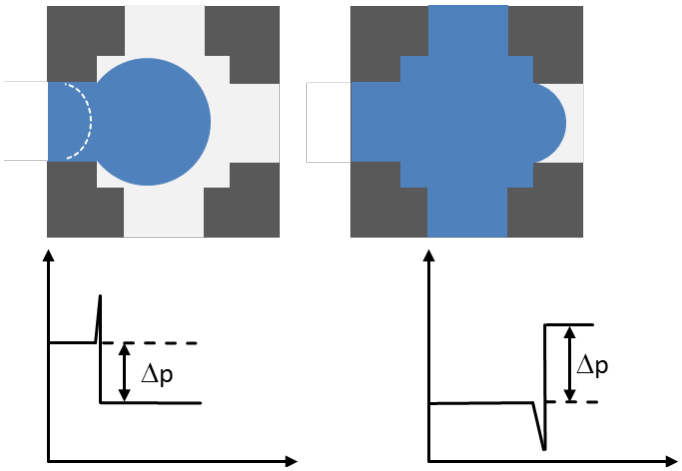

Figure 3.16: Schematic of the variation of the pressure jump at the interface between the fluids. Rapid expansion of the pore cross-section alters the contact angle between the interface and the solid surface and can form a temporary barrier for the invading liquid (left). In the opposite case, the radius of the interface curvature reduces and larger pressure is thus required to move the displaced liquid (right).

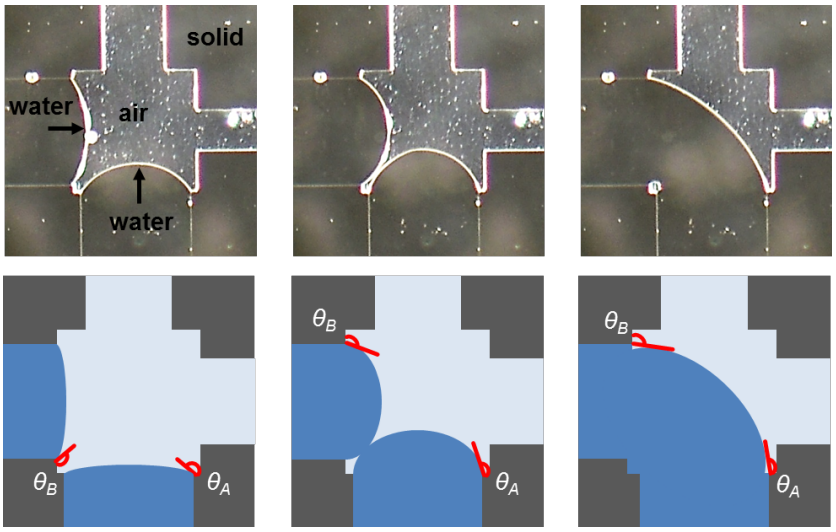

Figure 3.17: Merge invasion during the drainage process. The time sequence of images is from left to right [C].

tied immediately in the next invasion step. If this was the case, one would expect to see many isolated filled throats in the micromodel, because simply throats are more numerous than pores. The phase distributions shown in

Fig. 3.18 contradicts with this classical understanding. The reason for this contrast relies on the fact that the capillary valve effect plays a role during gas invasion. As a result, the threshold pressure of a pore can be larger than that of a throat in this micromodel. This means when a throat is invaded by gas, its neighboring pore may not necessarily be emptied. For this reason only a limited number of liquid clusters is formed during the entire drying process. Note that two effects need to be taken into consideration when analyzing the results in terms of drying time: first, liquid film developed along microgrooves at wall surfaces, which is referred to as the roughness film in literature, can develop. This type of film differs from the corner films. In fact, the corner films cannot form in the PDMS micromodels because of their hydrophobic surface characteristic. In such a solid surface the condition for formation of a corner film cannot be met [78]. Second, although the micromodel is sandwiched between two glass sheets, the liquid can still permeates through the micromodel walls to the surrounding medium. These two effects can lead to the overestimation of the drying time.

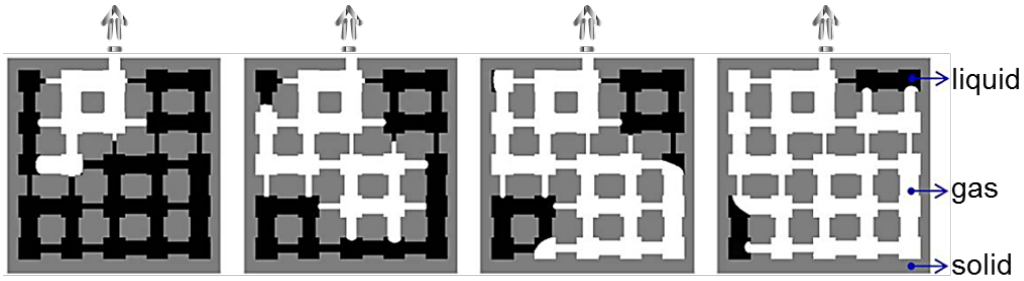

Figure 3.18: Evolution of phase distribution in a PDMS micromodel during drying. The micromodel is open to evaporation through a tube at the top. The time sequence of images is from left to right [D].

Drying experiments with a micromodel bounded with a gas purge channel are carried out. This type of measurement essentially mimics the situation that one may encounter when drying of a cathode gas diffusion layer (GDL) of proton exchange membrane fuel cells is concerned (see Fig. 3.19). In such situation a dry gas is usually pumped into the gas channel in order to evaporate the liquid water in the GDL. The micromodel used here is made of a channel with a length of 4.5 cm and a width of 1 mm. The micromodel dimension is 15×6 square pores. The side lengths of pores are sampled from the uniform distribution [0.12-0.97] mm with an increment of 0.01 mm. The distance between the centers of two neighboring pores is 1 mm. The width of a throat is equal to the side length of the adjacent pore.

The throats and pores as well as the channel have the same depth of 25 μm. The micromodel is covered by a glass sheet to avoid liquid permeation. Ethanol is injected into the channel at a rate of 200 μl/min to saturate the micromodel and the channel. During drying air was injected into the channel at a rate of 0.2 μl/min in order to remove liquid therein. During the air injection process, some amount of ethanol was removed from the surface pores and throats. Therefore, the micromodel is not fully saturated at the onset of the evaporation process. After the channel has been emptied, dry gas flows into the channel with a rate of 474 μl/min. During the gas injection ethanol evaporates and thus the pores and throats empty; the resulting phase distribution is shown in Fig. 3.20. One can see that the gas preferentially invades the pores and throats. Thus liquid splits into clusters of different sizes.

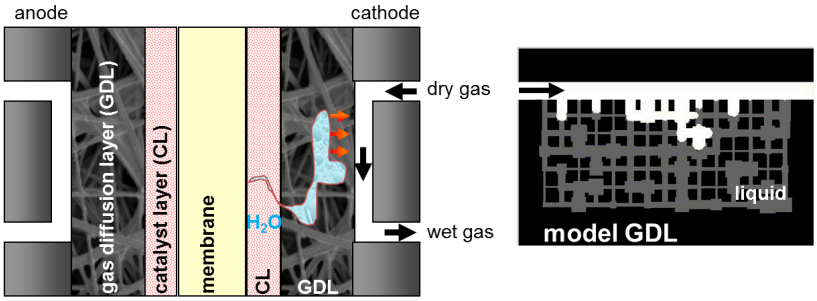

Figure 3.19: Schematic representation of a proton exchange membrane (PEM) full cell. The gas diffusion layer (GDL) of this cell is approximated by a microfluidic network made of PDMS.

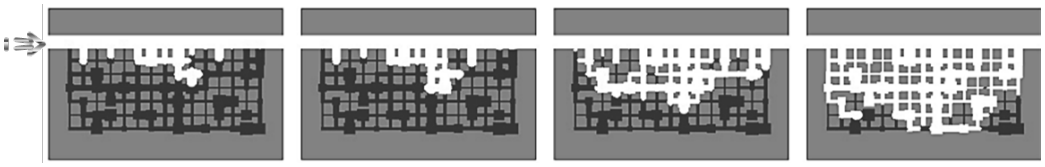

Figure 3.20: Evolution of phase distribution in a PDMS micormodel during drying. The air (in white) flows into the micromodel from left through a gas purge channel. The time sequence of images is from left to right [E].

The drainage and imbibition experiments are conducted with a small micromodel of size 5×4 throats. The throat widths are uniformly distributed in the range [0.14-0.94] mm. The pore located at the middle of the network

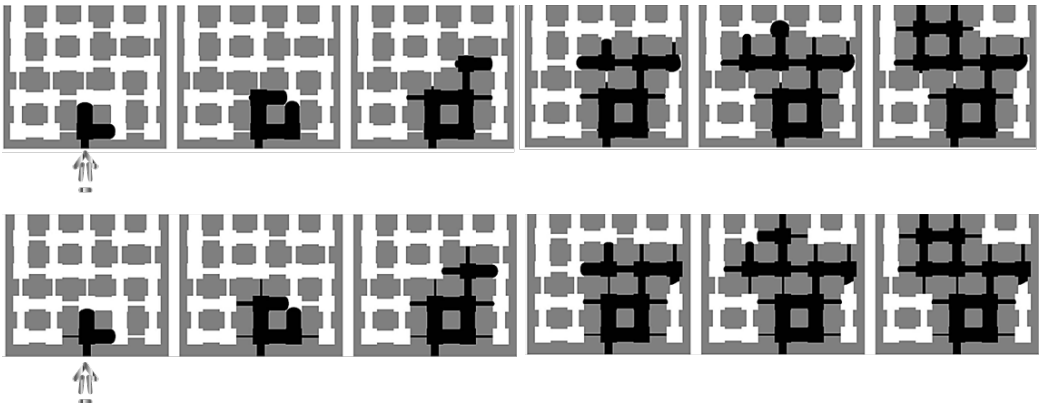

Figure 3.21: Evolution of phase distribution in PDMS micromodels during drainage (top row) and imbibition (bottom row). The miromodels are open to a reservoir through a pore at the bottom. The invading and the displaced fluids are shown in black and white, respectively [C].

bottom is connected to a tube of 0.5 mm wide and 8 mm long. The invading fluid is injected through this tube until the breakthrough time. The side opposite to this tube is open to the surrounding ambient. The other two sides are sealed. The fluid and solid properties are identical to those described in Figs. 3.15 and 3.17. During both the drainage and imbibition processes the phase distribution essentially evolves in a similar way, exhibiting a capillary fingering pattern (see Fig. 3.21). One noticeable difference however is that more throats are invaded in imbibition. This is so because the threshold pressure of the throats is lower than the pores and thus all available throats are invaded prior to the next pore invasion. The experimental results obtained from these micromodels are compared to corresponding pore network simulations in Chapter 4.

3.2 Optical Measurement of the Wetting Process

Wetting (or spontaneous imbibition) experiments are conducted with an etched silicon micromodel of 49 mm × 45 mm. This transparent micromodel is a 50×46 square lattice network of flow channels. This micromodel is not prone to liquid permeation through its walls. The accuracy and roughness of the etched pattern are higher compared to the PDMS micromodels. The lateral faces of this micromodel are sealed to any fluid, whereas the top and

bottom faces are open to surrounding air. All flow channels have a length of 1 mm and a depth of 50 μm. The widths of flow channels are sampled from a normal distribution with a mean value of 155 μm and a standard deviation of $\pm$ 15 μm (see Fig. 3.22). A high-speed camera, capable of capturing 360 frames per second, is utilized to visually observe the real-time fluid distributions within the channels during the liquid imbibition into the network. Typical recording time is about 30 s during which approximately 10000 images are acquired. A wetting fluid is provided through a reservoir installed to the micromodel entrance. The aqueous solution of ethanol with a mass fraction of 80% is used as wetting fluid. A sessile droplet of this solution on a flat glass substrate (the material used for making the micromodel) resulted in an equilibrium contact angle of 22°. To onset the wetting process, an additional amount of the wetting liquid is carefully injected by a syringe pump into the liquid reservoir. The acquired images are analyzed by an image-processing algorithm, which is presented in [63, 79].

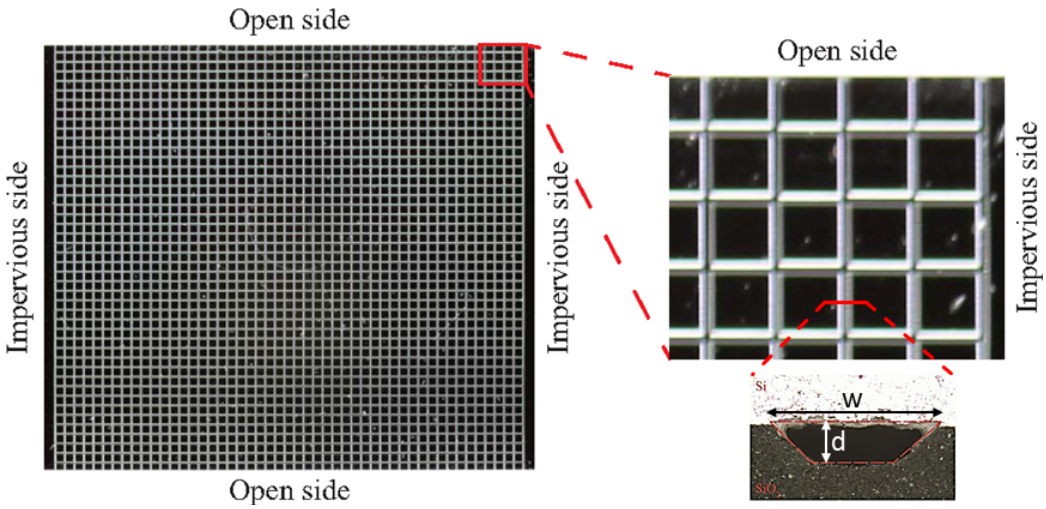

Figure 3.22: A quasi-two-dimensional physical etched micromodel [F].

A sequence of proceeded images is shown in Fig. 3.23. When the open side (here top) of the micromodel is brought into contact with the liquid mixture, the micro channels near the cross-sectional area of the micromodel are invaded by the liquid due to capillary action. The wetting process advances while the interface between wet and dry regions slows down until the micromodel is almost fully saturated with the liquid. The liquid invasion into the micromodel appears to occur in a quasi-steady way with a slightly ramified structure of the advancing wetting front. The width of this two-phase zone

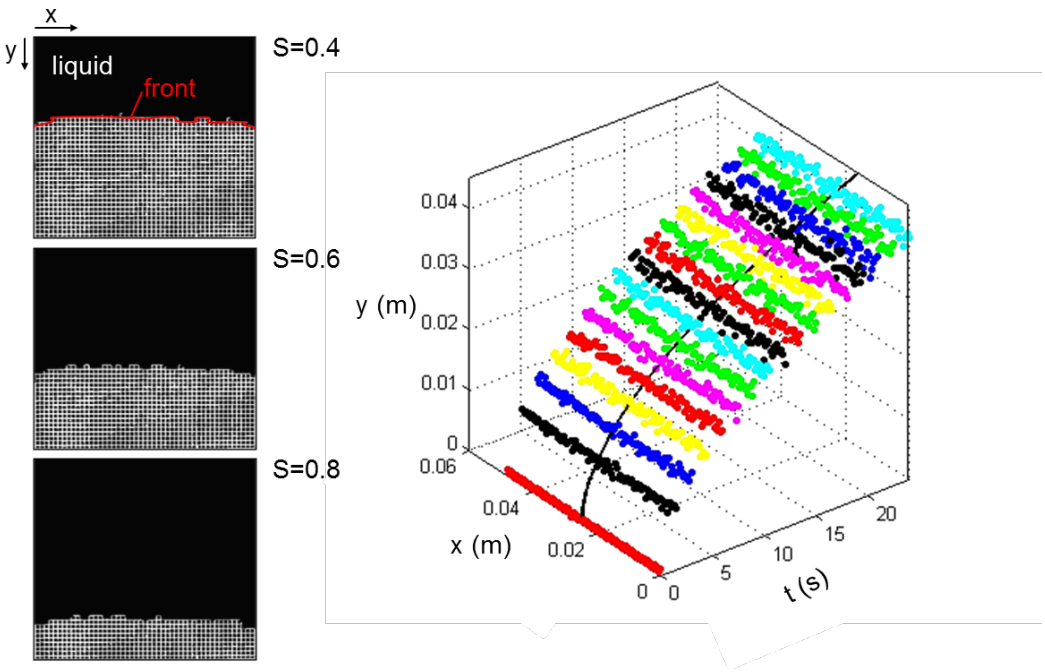

Figure 3.23: Liquid distribution (left) and spatio-temporal variation of the advancing liquid front (right) in the etched micromodel during the wetting process [G].

remains almost constant, as can be seen in Fig. 3.23. The overall wetting kinetics is also determined by tracking the total liquid volume imbibed into the micromodel as a function of time, shown as solid line in Fig. 3.23. The transient behavior of the advancing liquid front follows the classical Lucas-Washburn law; this aspect is discussed in details in Sec. 4.1.7. A similar phase distribution is obtained from the experiments with this micromodel but different mixtures of ethanol and water, see [F] and [63].

3.3 X-ray Tomography Measurement of Particle Packing Drying

Optical methods described in Sec. 3.1 cannot be used for visualization throughout the depth of porous media such as particle packings. The low resolution of these visualization methods also make it difficult to characterize the structure of the liquid phase in a particle packing, even with two dimensions; especially when the liquid is trapped at the wedge-shaped pores located near the

particle-particle contacts. To circumvent these issues, X-ray microtomography technique can be used, among other three-dimensional image techniques such as magnetic resonance imaging (MRI) [80] or synchrotorn X-ray tomography [81].

A laboratory-scale X-ray microtomograph and image analysis technique are utilized to study drying of a three-dimensional particle bed packed with unconsolidated glass beads. Such a particle packing is seen as a better representative of real porous media than etched micromodels. In fact, many real porous products are built from primary particles by means of processes such as agglomeration or sintering. A cylindrical plastic container with an inner diameter of 8 mm is used to generate the packing of glass beads with an approximately height of 8 mm. The glass beads are almost perfect sphere with a mean diameter of 0.8 mm, resulting in a bed porosity of about 38%. Based on the X-ray microtomography principle, an X-ray beam is attenuated as it travels through the material. The attenuation intensity of a material is quantified by the so-called attenuation coefficient that depends on the density, atomic number of the material and on the energy of the beam that passes through the material. The similarity between attenuation coefficients of different materials may produce a lack of contrast between different phases in an image. This problem is very significant especially at lower liquid content of the packing. In order to enhance the contrast of the image and separate the liquid, gas and solid phase clearly during drying, the liquid is doped with the iodide ion in the form of potassium iodide (KI) as the solute tracer. KI was selected since it favors X-ray absorption characteristics and the viscosity and surface tension of the solution remain essentially unchanged. Moreover, the state (crystal or ion in the liquid) of this dissolved salt can be used to track a drying front that traverses the particle packing; for this purpose, a high concentration of aqueous potassium iodide solution (73 wt%) has been used here.

The X-ray cone beam source was generated at 90 kV and 120 μA. For the tomographic reconstruction, 400 raw data was collected while the sample rotation from 0° to 360°. Initially, the whole sample was saturated with KI solution and was mounted on a sample holder inside the X-ray system. Then the tube for air supply is carefully placed above the sample to make sure that the air flow can blow over the open side of the sample and the holder will not touch the channel when it rotates (see Fig. 3.24). Drying starts with air flow velocity of 1 m/s and room temperature of 26°C. These conditions are controlled by a supply line for dry air and a sensor for recording temperature installed in the micro tomographic device. At every 30 min, the air supply was stopped in order to perform one X-ray scan which took around 25 min; this process was repeated until the sample dries out. The sample

stays in the X-ray equipment during the whole drying and scanning process; thereby particle displacement can be prevented at maximum. Measurement and reconstruction software Volex has been used. The output from the reconstruction algorithm is a three-dimensional array of gray level intensities. By adjusting the distance between source, sample and detector, resolution is 4 μm and by grouping detector pixels, effective voxels sizes of 16 μm has been set; the cropped images contain approximately 517×520×436 voxels.

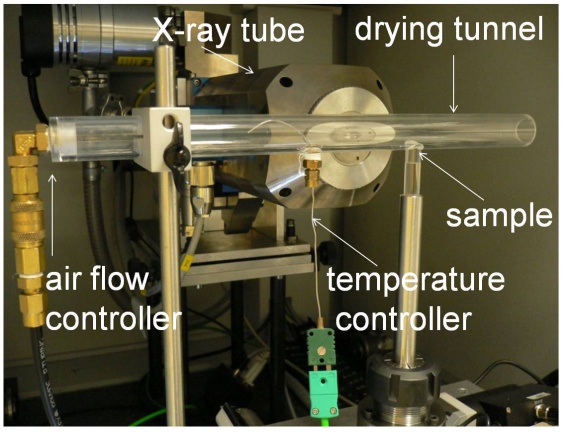

Figure 3.24: Dryer setup inside X-ray tomography device [H].

To improve the image quality and to allow for geometric analysis, several image processing steps need to be performed. First, the original reconstructed gray images were cropped to only consider the areas of interest. Then a median filter was used to smooth edges and to reduce noises. Segmentation of the gray images into the respective phases (solid, liquid and air) was done by choosing appropriate threshold values from gray-level histograms. The gray-level histogram represents the three phases as three peaks. In order to separate the solid, liquid and gas phases, two threshold values of the attenuation coefficient were found to binarize the gray level images into black and white images. It was not necessary to apply a specific threshold value for each segmentation process at various liquid contents. The volume and number of liquid clusters were determined by the algorithm which is based on labeling of connected liquid voxels. Details on image processing algorithms can be found [82].

The spatiotemporal distribution of the liquid phase from the onset of the drying process down to a very low average liquid content, i.e. 1.7%, is obtained from the high-resolution reconstructed X-ray images. Each three-dimensional X-ray image is cut into several two-dimensional slices, from which the liquid content is calculated as a ratio of the liquid volume to the

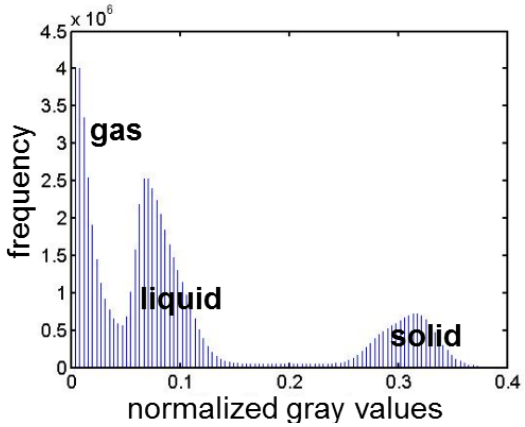

Figure 3.25: A histogram of normalized gray values of a model glass bead packing [H].

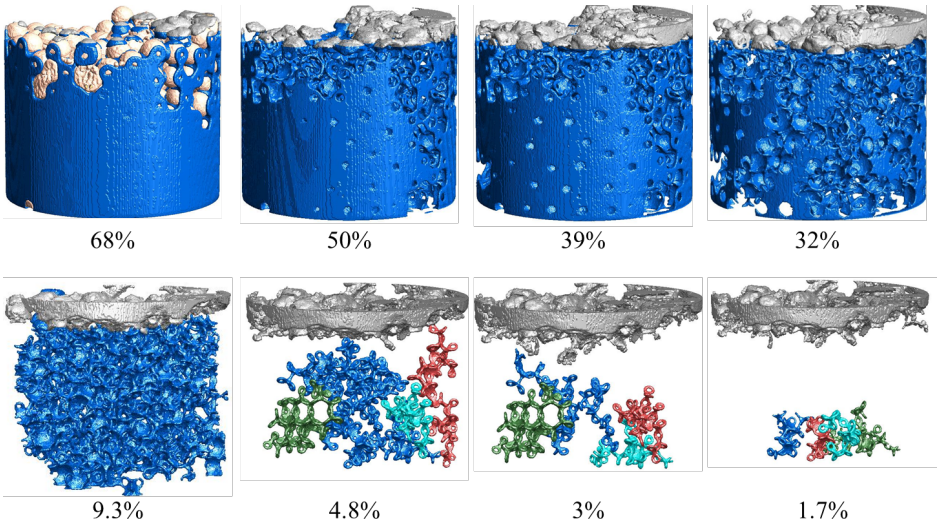

Figure 3.26: 3D structure and evolution of liquid during drying of particle packing. Liquid clusters are labeled in blue, green, red, and cyan by decreasing volume. Salt crystals deposited at the packing surface are shown in gray. Particles (in wheat) are only shown at liquid content 68% [I].

total void space volume. These volumes are calculated from the voxel size and from the number of voxels corresponding to the liquid and solid phases.

Figure 3.26 shows morphology and the time evolution of the liquid phase as well as the aggregated polycrystalline structures formed at the packing surface during drying. At the beginning of the drying process, large pores are invaded by the gas phase, while the liquid is pumped from the large

pores to small pores. This major physical effect of capillary pumping keeps the small pores at the surface partially wet. This effect has already been observed and the liquid structure was visualized in [H], but only up to a liquid content of 20%. Here, we go beyond these steps and characterize the liquid structure and its connectivity from the beginning up to near end of the drying process.

As can be seen in Fig. 3.26, near the open surface and along the container wall small liquid clusters are separated from the main liquid cluster which spans the main region of the packing. The main cluster (in blue) stays connected to the evaporation front – which is still near the surface of the packing – through networks of liquid rings formed at mutual contact points between particles until the liquid content reaches 4.8%. Afterwards the liquid rings are detached from the top surface and thus a dry zone develops therein. At liquid contents below 9.3% isolated small liquid rings – and salt crystals inside the packing – were filtered out to accentuate the continuity of the large ring clusters.

These annular rings can be regarded as secondary capillary structures of the pore space at low liquid contents. A very nice illustration of the ring clusters and their interconnectivities at liquid content 4.8% is shown in Fig. 3.27. The liquid is disintegrated into several clusters with ramified structure. These clusters are classified into six groups according to their respective volumes. In each group the clusters are labeled and then they are counted. Few large and many small ring clusters are identified. Among these clusters, those with the smallest volume are numerous and they span almost the entire packing. The role that such rings play in drying can be positive or negative. They can maintain long-distance hydraulic connections between saturated pores that would otherwise be separated. Drying time will thus be shorten. In the presence of salt, their impact could however be disruptive, e.g., for valuable artworks and monuments. This is attributed to salt crystallization phenomena that occur as a result of ring evaporation [83]. Three-dimensional geometry of such liquid structures and how they can affect the mechanical properties of wet assemblies have been investigated in [84]. What we should expect when considering real particulate systems, e.g. granules made of primary particles, instead of the glass beads used here. We conjecture that the secondary capillary elements may not play a role as important as in the model particulate systems, since the space between the primary particles is partly occupied by solid bridges in real systems.

We now consider other aspects of the particle packing drying, i.e. the salt transport and crystallization. The salt crystals that are deposited in a discrete way at the packing surface during drying is shown in Fig. 3.28. During drying the dissolved salt is transported towards the drying front (i.e. the in-

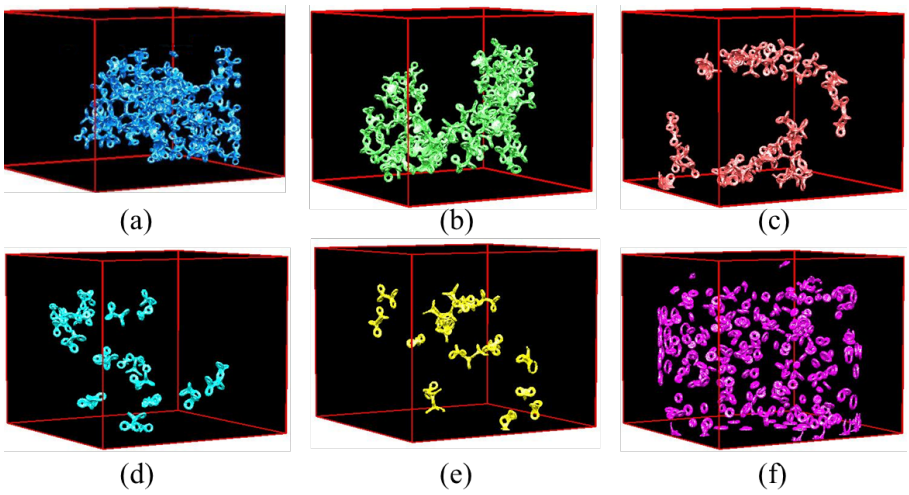

Figure 3.27: Volume and number of liquid ring clusters at liquid content 4.8%: (a) $2\times10^5\mu m^3$, 6, (b) 0.8-$2\times10^5\mu m^3$, 12, (c) 0.4-$0.8\times10^5\mu m^3$, 19, (d) 0.2-$0.4\times10^5\mu m^3$, 14, (e) 0.12-$0.2\times10^5\mu m^3$, 22, and (f) 0.03-$0.12\times10^5\mu m^3$, 350 [I].

terface between the unsaturated and dry zones) by capillary pumping through the liquid-saturated pores and the network of hydraulically connected rings. Since drying is rather slow, local increase of salt concentration at the drying front results in back-diffusion of the salt ions towards the bulk liquid in the packing center. Crystallization occurs when the local salt concentration reaches the saturation level. Figure 3.29 shows a sequence of tomograms that nicely demonstrates the motion of the drying front and the evolution of the salt-crystal regions at low liquid contents of the particle packing. The motion of the drying front and salt deposit occur in discrete steps. With further evaporation, large ring clusters split into small disconnected network of rings which dry out progressively towards the bottom of the packing. This leads to a non-uniform formation of salt crystals. This observation essentially implies that the motion of dissolved component is mostly confined to the boundaries of a liquid-filled region or of a film region.

The deposition of solids in porous materials during drying is an important phenomenon with applications ranging from soil salinization in agriculture or damaging of building materials [85, 86, 87, 88, 89] to impregnation of porous catalyst supports [90]. The fundamental influences of pore structure, drying conditions, as well as initial solute concentration on the solid distribution in technical porous support structures after drying and impregnation are studied in [90].

One more point that can be seen in Fig. 3.29 is the morphology of the

drying front which appears to be fractal. The three-dimensional morphology of the drying front and the scaling characteristics of the liquid structure in a sand column saturated by pure water were studied using synchrotron X-ray tomography in [91]; the results indicate that the drying front is rough and multi-affine.

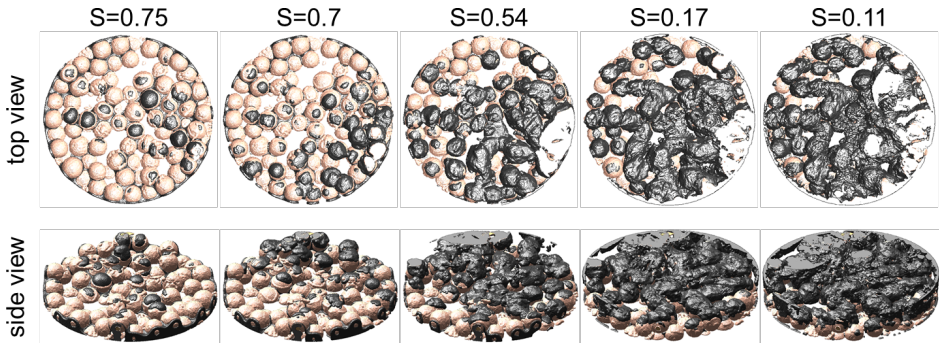

Figure 3.28: 3D structure and evolution of salt crystals deposited at the surface of the packing during drying. Salt crystals and particles are shown in gray and wheat, respectively.

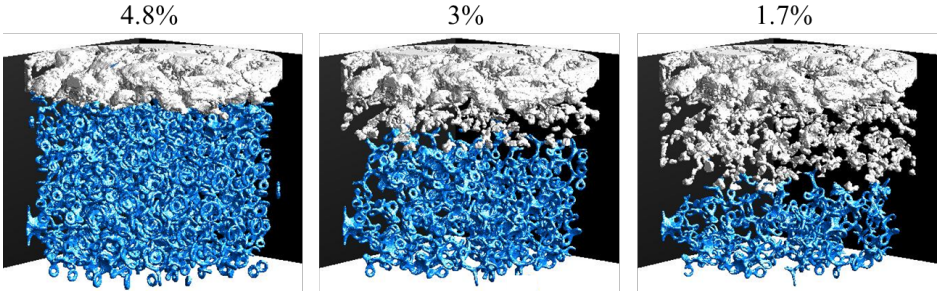

Figure 3.29: Evolution of drying front and salt crystals during the drying process. Salt crystals in gray and liquid phase in blue [I].

In Chapter 4 the liquid capillary rings are approximated as annular discrete entities with volumes computed from the center coordinates of neighboring particles. A three-dimensional pore network drying model is developed that incorporates this new effect. Pore network simulations involving films of liquid rings are expected to improve our understanding of the relationship between liquid configurations, pore-scale effects, and drying kinetics and to give a better prediction of the experimental observations. Moreover, pore network simulations of ion transport and crystallization induced by drying are presented in Chapter 4.

Another series of drying experiments has been conducted with the same tomographic device, but for loose packings of sintered glass beads (mean diameter of 700 μm) initially saturated with water. The intention behind fabricating this packing is to generate a physical model of real gels, which are typically highly porous particle aggregates. This model system is produced by sintering of glass beads inside a graphite mold [A]. The time variation of the solid, liquid, and gas phase distributions during drying of this particle packing is shown in Fig. 3.30 and the corresponding 3D visualization is shown in Fig. 3.31. These figures demonstrate nicely two major pore-scale phenomena relevant to drying of highly porous model particle aggregates: capillary flow and liquid film effect. It can be seen that the large pores are drained by drying air while small regions of the void space remain saturated with liquid for longer time of drying. Similar to drying of compact particle packing shown before, the long-distance between the liquid-filled region and the packing surface is connected via a network of liquid rings formed around particle contacts. Numerical simulation studies of this model system are reported in [a].

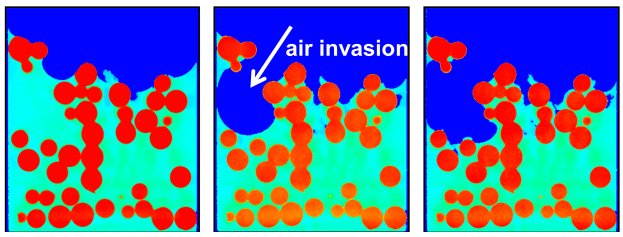

Figure 3.30: 2D tomograms for a packing of sintered glass beads at various liquid contents [A].

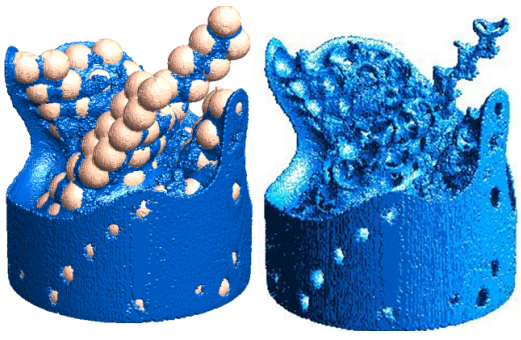

Figure 3.31: 3D visualization of a partially wetted sintered particle packing [A].

3.4 Characterization of Wet Wipes by X-ray Tomography

Wet wipes are predominantly used for cleaning and skin care purposes. One particular type of these commercial wet wipes is considered here, which is called Pampers Baby Wipes. These wet wipes are heavily applied for wiping infants' backsides in diaper changing. They typically consist of a thin porous substrate moistened with a liquid lotion and packed in stacks. The substrate is a non-woven fibrous sheet composed of various types of natural and man-made fibers. The liquid lotion is a water-based emulsion containing several useful ingredients such as surfactants, moisturizes, and perfumes.

Several product quality indices of Pamper Baby Wipes (e.g. the dispensing performance or the wetness perception) can be influenced by the evolution of the lotion distribution over time within wipes. The inner morphology of the substrate plays a crucial role in the dynamics of lotion penetration into a single sample wipe during lotion loading. Therefore, an effort is made to characterize the pore space of two types of substrates, which are referred to as a and b. For this purpose, a sample of each substrate was scanned by means of the aforementioned X-ray microtomography system. The structural properties, i.e. the porosity and the pore size distribution, were determined from the reconstructed high-resolution images (voxel edge length 3.8 μm). For image processing and data analysis we refer the reader to [J] and [63]. Figure 3.32 shows the segmented and volume images of the dry and wet substrates of identical type.

The local through-plane porosity profiles of both substrates are determined from the corresponding X-ray images. These profiles are plotted versus the normalized substrate thickness, where the thickness of substrates a and b are 790 μm and 697 μm, respectively. Three layers are distinguished in both substrates, giving rise to a composite structure of Pampers Baby Wipes. The mean value of the porosity of these substrates differs slightly, as shown with dashed lines in Fig. 3.33. As can be seen, the fiber packing is more dense in the middle layer, whereas it becomes gradually looser towards the top and bottom layers of the substrates. Moreover, the pore size distributions (PSD) of each layer of the substrates are determined individually from the X-ray images. Figure 3.34 shows the pore size distribution obtained for wipe a. A difference between the PSD of the layers is observed. In the top and bottom layers, about 50% of the pore space is occupied by pores with radii smaller than 100 μm, whereas the corresponding value is about 90% for the middle layer. In Sec. 4.1.7 these measured PSDs are utilized to generate a pore network model made of three layers. The pore network simulations of

wetting are then conducted to describe the transient lotion distribution in a fibrous medium made of three layers.

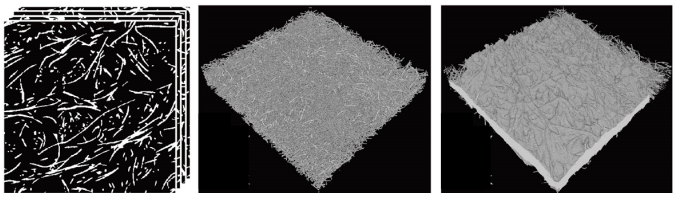

Figure 3.32: 2D binarized (left) and 3D reconstructed X-ray images of dry (middle) and wet (right) wipe substrates [J].

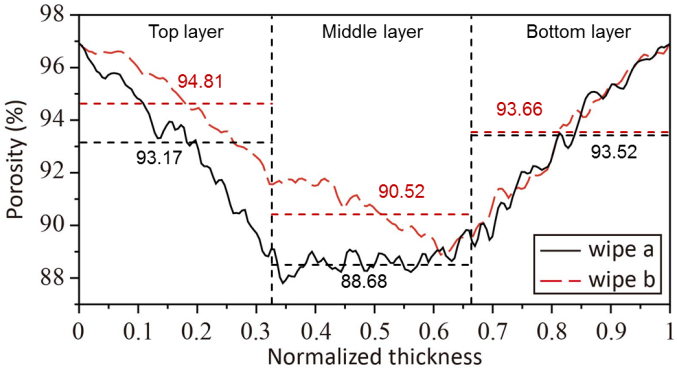

Figure 3.33: Porosity profiles obtained from X-ray images of two types of dry wipe substrates [J].

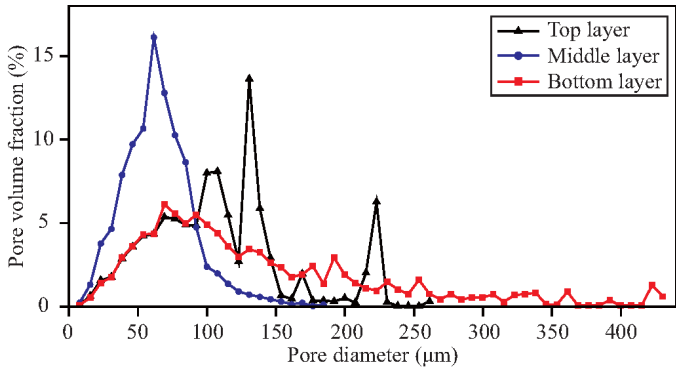

Figure 3.34: Pore volume distribution in the three layers obtained from X-ray images of dry wipe substrate of type a [J].

Chapter 4

Discrete and Continuum Models

This chapter provides an overview over discrete pore network models which are successively developed at the Chair of Thermal Process Engineering at Magdeburg University. These models extend the previously existing pore network drying models by new pore-scale physical phenomena, i.e. capillary valve effect, capillary rings, thermal effect, pore condensation, and solute transport. Due to these extensions, new applications in the fast-growing field of pore network modeling have been opened up. Superheated steam drying of porous materials is simulated using the model version that accounts for both thermal effect and condensation of vapor in pores. The pore network model extended by a solute concentration in the pore liquid can describe functionalization of porous substrates by impregnation and drying. Next, the attention is turned to pore network simulations of wetting with single and dual pore structures. Such simulations are carried out with the aim of determining liquid redistribution in the composite materials. An advanced pore network model that combines drying and wetting algorithms are presented. This model provides a rough approximation for a spray agglomeration process, during which liquid droplets interact with porous particles. The wetting-drying model is then combined with solute transport, so that the impregnation-drying process is simulated. The second part of this chapter seeks to present up-scaling routes. In this regard, discrete pore network simulations are seen as appropriate numerical experiments which are exploited to predict a number of effective parameters of the classical one-equation continuum models. Then, the relevance of the continuum models is assessed. The continuum description of the liquid velocity field caused by drying is reconciled with the pore network simulations. At last, the coupling between the external and internal mass transfer in drying porous media is revisited.

4.1 Pore Networks and Physical Effects

Pore networks are classified into four types (for a synoptic overview, see Table 4.1). This classification is based upon the geometry of pore entities: throats and nodes/pores (see Fig. 4.1). The motivation behind the approximation of the void space with entities of simple geometries (e.g. cylinder, sphere or cube) is essentially that transport mechanisms can be formulated by using simple physical laws. A bunch of such entities with different sizes together with their connectivities are required to generate a pore network. The radii of the pore entities are sampled from a normal or uniform density distribution function. Other distributions of radii would be possible. Aside from this statistical method, such information for a small representative volume can also be obtained from several characterization methods, such as X-ray tomography, focused ion beams and scanning electron microscopy, nuclear magnetic resonance, mercury intrusion porosimetry, and gas adsorption. The latter two methods can produce pore size distribution, but not the full pore connectivity. These techniques are thoroughly described and compared in [92].

Each type of these pore networks accounts for certain physical effects, which are summarized in Table 4.1. Among these effects, capillary pumping and liquid viscous flow are the absolute minimum to simulate the dynamics of the wetting process. Or capillary flow in the liquid phase and vapor diffusion in the gas phase must be coupled to predict the drying process. None of these pore networks account for all effects together. To a large extent this is because each pore network approximates the pore structure (i.e. geometrical and topological characteristics) of certain porous materials with specific applications, and because the role that some effects play during a process is secondary or absent completely. Besides these reasons, pore network simulations that account for all these effects together would be very demanding, at least with the present computational power. Therefore, when the pore-scale modeling of a porous material during a certain process is concerned, the most relevant effects are considered and some assumptions are made. Indeed, the choice of where and how to make assumptions in a pore network model affects what type of information one can expect to obtain from it. For example, in slow drying liquid viscous effect or convection in the gas phase can be neglected as they may make little contribution to the process kinetics; or gravitational effects can play a prominent role if porous materials are vertically elongated and contain large pores; or Knudsen effect (change in diffusion behavior of gas molecules) and Kelvin effect (reduction of saturated vapor pressure) can contribute to drying of porous materials at atmospheric pressure if their pore sizes are smaller than about 40 nm. Overall, the credi-

bility of pore network simulations for a given problem relies on the governing equations, the underlying simplifications applied for the transport equations, as well as the length-scale for the computational domain.

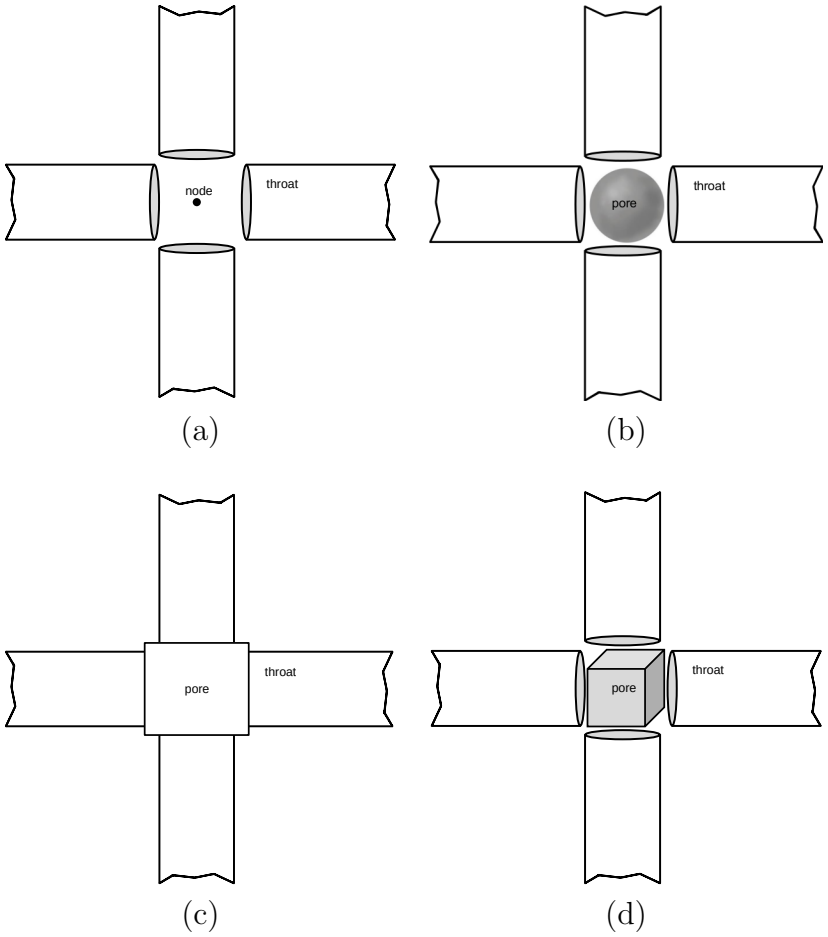

Figure 4.1: Types of pore networks: (a) network I: cylindrical throat and volumeless node, (b) network II: cylindrical throat and spherical pore, (c) network III: rectangular throat and square pore, and (d) network IV: cylindrical throat and cubic pore. In two-dimensional space each node or pore is connected to four throats resulting in coordination number of four. Only a part of the networks are sketched.

4.1.1 Pore Network Modeling of Drying

Pore network models for drying can essentially be classified into two main types: non-viscous and viscous pore network models. The non-viscous ver-

physical effect	network I	network II	network III	network IV
capillary flow	×	×	×	×
vapor diffusion	×	×	×	×
liquid viscosity	×	×	–	×
vapor viscosity	–	×	–	–
thermal effect	×	×	–	–
gravity effect	×	–	–	–
pore condensation	–	×	–	–
capillary force	×	–	–	–
fluid-solid coupling	×	–	–	–
capillary ring	×	–	–	–
dissolved component	×	×	–	–
capillary valve effect	–	–	×	×
gas purging	–	–	–	×
adsorption effect	–	–	–	–
Kelvin effect	–	–	–	–
Knudsen effect	–	–	–	–

Table 4.1: Physical effects that are incorporated (×) into or excluded (–) from the pore networks which are sketched in Fig. 4.1.

sion of the model describes the mass transport under slow isothermal conditions. The gas phase with a semipermeable liquid-gas layer consists of two components, vapor and dry air. Both components are assumed to be ideal gases with total pressure p_g. Two phenomena occur in the gas phase: molecular diffusion of vapor and total convective flow (Stefan flow) which balances the diffusive flux of the air and thus the total air flux vanishes [93]. The quasi-steady vapor diffusion in the gas phase (boundary layer as well as dry regions within the network) is calculated via setting up mass balances for any gas node/pore j that add up to zero:

$$\sum_j \dot{M}_{v,ij} = A_{ij} \frac{\delta}{L_{ij}} \frac{p_g \widetilde{M}_v}{\widetilde{R}T} ln(\frac{p_g - p_{v,i}}{p_g - p_{v,i}}) = 0. \tag{4.1}$$

Here, the sum runs over all nodes that are neighbor to node j, and where L_{ij} denotes the distance between nodes ij, A_{ij} the exchange cross section between two nodes (πr_{ij}^2 for network, L^2 for boundary layer), and δ the vapor diffusivity. The system of equations (4.1) is solved for unknown partial vapor pressure by applying Dirichlet boundary conditions, i.e., the vapor pressure of drying air in the core flow and saturated vapor pressure next to the gas-filled interface.

At the beginning of the drying process, all interface throats are located on the network surface because only this surface is open for evaporation. These throats are all interconnected by liquid and all have the same evaporation rate. Due to the capillary effect, however, only the largest throat is emptied, from which liquid can slowly flow into all the others without friction loss or gravitational effect. The time for emptying this throat is given by its volume and the total drying rate. Thus, throats empty one after the other. Owing to the random size distribution of throats, the liquid can be split up into several clusters, and further emptying proceeds independently in each cluster. An essential component of the model is therefore the cluster labeling, which is implemented as a variant of the Hoshen-Kopelmann algorithm [94]. Once one throat is completely drained, the topology of the liquid may change. Therefore, the following steps must be repeated iteratively until the network is dry: 1) label clusters for current liquid distribution, 2) solve the vapor diffusion equation for the gas phase, 3) calculate the (maximum) time step for each liquid cluster from the total evaporation rate and the amount of the liquid in the largest throat at the phase boundary, 4) update phase distribution for smallest cluster time step. Though many physical effects are neglected in this model version, it can be used as a numerical experiment to study the impact of the pore-structure heterogeneity on the drying process [28, 95].

As regards the viscous pore network model for drying, both liquid viscous and capillary effects are taken into account. Contrary to the non-viscous model, it is no longer assumed that the capillary flow can transport liquid at any rate and over any distance. Instead, it is checked whether the capillary pressure difference (Eq. 2.7) is sufficient to supply liquid with the local evaporation rate. If not, the meniscus moves according to the difference in mass flows for liquid and vapor. Capillary flow rates $\dot{M}_{w,ij}$ between two nodes i and j are calculated by the Hagen-Poiseuille equation. Liquid pressure field is calculated from mass balances at any liquid node/pore j, as

$$\sum_j \dot{M}_{w,ij} = \frac{\pi r_{ij}^4}{8\mu_w L_{ij}}(p_{w,i} - p_{w,j}) = 0. \tag{4.2}$$

Vapor diffusion in emptied throats is governed by diffusion with Stefan correction (Eq. 4.1). Vapor diffusion is coupled to liquid flow at the menisci, which are either moving or stationary, depending on the available capillary pressure in each throat where wetting coefficient is assumed to be unity (perfect wetting). Note that calculations in this model, like the non-viscous model, are performed under quasi-stationary conditions. This means the menisci move at constant speed until one of them reaches the end of a throat. At the tran-

sition to the next quasi-stationary state, no inertia effects are accounted for. Due to the discrete changes in the pressure field, partially emptied throats may be refilled. Completely drained throats remain empty, however. Further details on these pore network drying models can be found in [96, 97].

It shall be emphasized that capillarity is the core physical effect which is present in both model versions. The rudimentary model version is suitable enough to be used at conditions where viscous effects are negligible. These conditions are fulfilled for low drying (and liquid flow) rates, for large pores, and for liquids with low viscosity. On the other hand, when drying (and liquid flow) rates are high, pores are small or liquids are viscous, it is inevitable to opt for the model version that takes into account viscous effects. Nevertheless, it may be hard to justify the application of the isothermal viscous pore network model for high drying rates.

4.1.2 Capillary Valve Effect

Real porous materials contain often pores of different sizes, such that small pores may be connected to large pores with sudden geometrical expansions in the pore cross-sections at the interface. Such a rapid enlargement of the pore cross-section has been observed in our PDMS micromodels. This enlargement of a pore is referred to as a capillary valve and its effect on the motion of the invading fluid as the capillary valve effect (CVE) (see Sec. 3.1.2). This effect essentially alters the threshold pressure of partially filled pores or throats in the micromodels, which in turn impacts the underlying process dynamics. In this subsection, pore network simulations are conducted for slow drying, drying with gas purging, and capillary-dominated two-phase flow. These simulations are conducted in the presence of the CVE. And, the pore space microstructure, the physical properties of the invading and displaced fluids, as well as the initial and boundary conditions are identical to their experimental counterparts presented in Sec. 3.1.2.

The classical algorithm for a duct (i.e. a pore or throat) invasion during slow drying is that in each liquid cluster a partially filled duct (or a meniscus duct) with the lowest threshold pressure empties first. If the pressure difference between the gas and liquid phases neighboring to this partially filled duct exceeds the threshold pressure of the duct, this duct will be invaded by the gas phase. A modified version of this criterion requires to be met when the CVE is taken into consideration; for more details on the drying algorithm see [D].

The simulation results obtained from the pore network models with and without the CVE are shown as phase distributions and drying curves in Figs. 4.2 and 4.3, respectively. As can be seen from the phase distributions,

neglecting the CVE leads to the formation of isolated filled throats that span the entire pore network. In this network the threshold pressures of the pores are lower than the adjacent throats, because they are simply larger. Thereby once a throat in a liquid cluster is invaded by gas its neighboring filled pore will be emptied accordingly. A different situation can however occur in the pore network model with the CVE. The threshold pressure of a pore can be larger than that of a throat because of the burst or merge invasion event. These simulation results can be assessed with the experimental counterpart which is presented in Sec. 3.1.2. A better agreement between these pore network simulations and the microfluidic measurement is observed when the CVE is accounted for in the model. Though the impact of the CVE on the phase distribution can be decisive, its role on the total drying time is marginal (see Fig. 4.3). The drying time predicted by both pore network models is about three times longer than the measurement data. We conjecture that this deviation can be attributed to the liquid permeation through the micromodel walls and the liquid film flow along microgrooves at the wall surfaces.

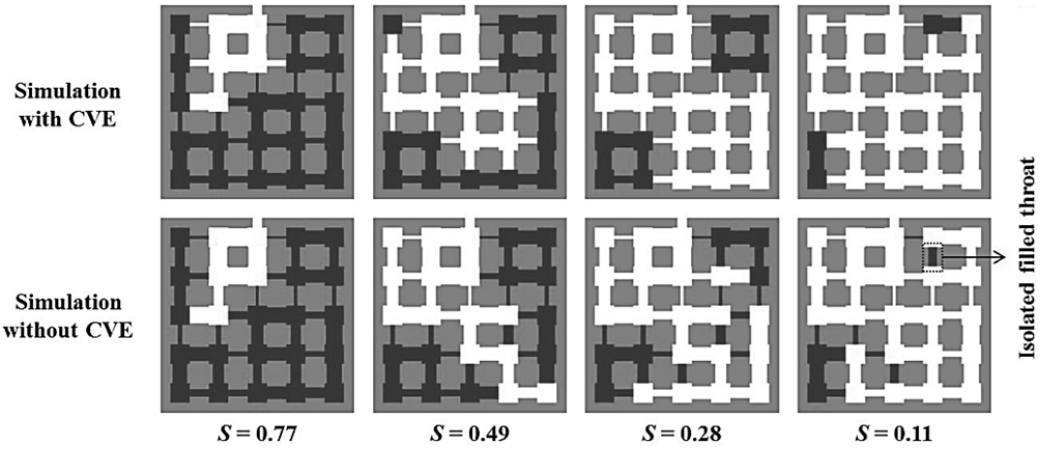

Figure 4.2: Simulated phase distribution in the pore network models with and without the capillary valve effect (CVE) at different values of liquid saturation S [D].

The simulation results obtained from a 2D pore network model that accounts for the gas purging and for the CVE are shown in Figs. 4.4 and 4.5. This pore network is of type IV in Table 4.1. In order to formulate easily the threshold pressure for a pore invasion through the bust event, throats with cylindrical geometry are considered. The radius of the largest inscribed sphere gives the pore radius. Pore and throat radii are distributed uniformly in the interval [8-12] μm and [2-7] μm, respectively. The pore network is

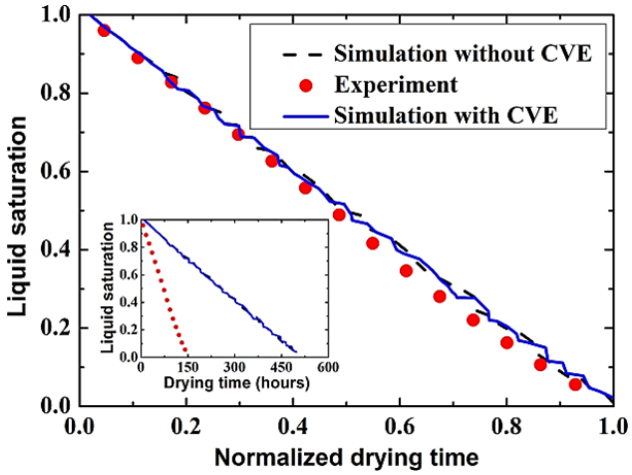

Figure 4.3: Simulated and measured variation of the liquid saturation versus the normalized drying time. The drying time divided by the total drying time yields the normalized drying time. The variation of the liquid saturation with the drying time is shown in the inset [D].

hydrophobic with an advancing contact angle of 105°. Details of the pore network structure and the governing equations of the model can be found in [E].

The pore network simulation results are compared to the data acquired optically from the PDMS micromodel (see also Sec. 3.1.2). The pore network model predictions can fairly well reflect the experimental data, both the phase distribution and drying kinetics. Due to the hydrophobic nature of the pore network and since the pores have a larger threshold than throats, once a pore is invaded by the gas phase during drying, its neighbor throats empty in the next steps. In a liquid cluster, the partially filled pore with the lowest threshold are emptied. The threshold pressure of a pore body depends on the sizes of its neighboring pore throats. The sizes of pore throats are randomly distributed. This in turn results in random gas invasion in the pore network. When comparing curves in Fig.4.5 note that the drying time is normalized. Because prior to starting the drying process, it was impossible to completely fill the network while keeping the purge channel entirely empty. For this reason, misinterpretations such as the simulated drying is faster than the measured one must be avoided.

The pore network simulations of drainage and imbibition are carried out for the limiting case of the capillary-dominated regime. For these simulations a 2D network model of type III that accounts for the CVE is employed (see Table 4.1). Figure 4.6 shows the phase distributions during the drainage and

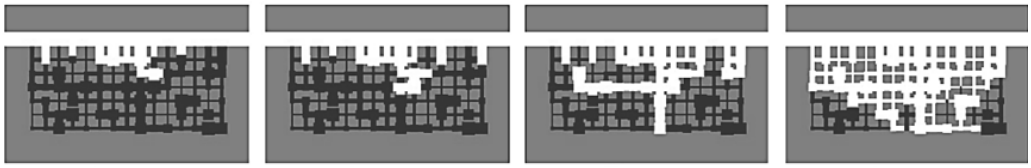

Figure 4.4: Simulated phase distribution in the pore network model that accounts for the capillary valve effect (CVE). The time sequence of the images is from left to right [E].

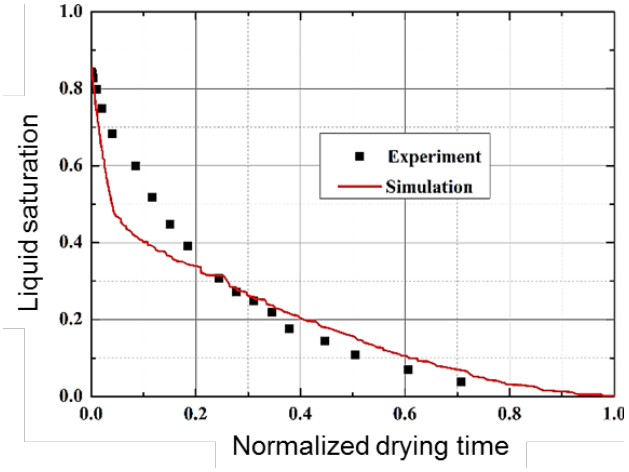

Figure 4.5: Simulated and measured variation of the liquid saturation versus the normalized drying time [E].

imbibition processes. The phase distributions are similar with a capillary-fingering pattern. More throats are however invaded in imbibition. This is because the threshold pressure to invade a throat is smaller than to burst into a pore. Therefore, pore invasion is dominated by the burst event in both processes. On the other hand, a stable displacement pattern is observed when the process was driven by the merge invasion, see [C].

Simulations with a 2D pore network model, which accounts for the gas purge channel but excludes the capillary valve effect, are presented here. The simulations are conducted for different values of the Reynolds number Re for gas flow in the channel. The Re is systematically varied in order to study the impacts of the gas flow rate. Figure 4.7 demonstrates the phase distribution in the networks and in the corresponding gas purge channels during drying for $Re = 0.1$ and 10. In these figures, the pores and throats which are filled completely with liquid, partially with liquid, and completely

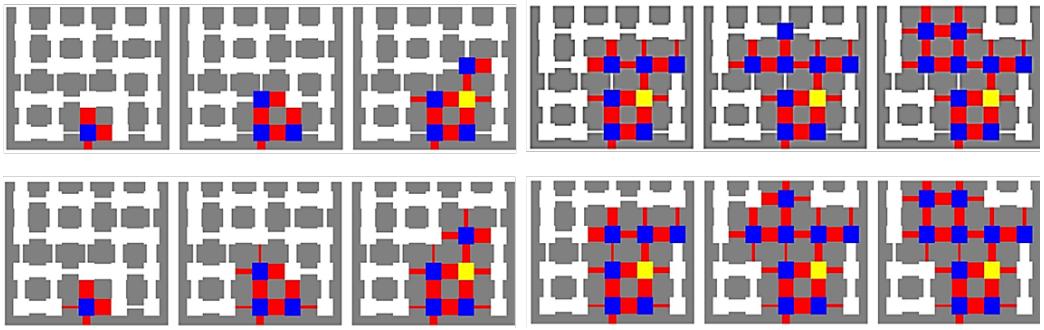

Figure 4.6: Simulated phase distribution during the drainage (top row) and imbibition (bottom row) processes. The color coding is as follows: the invaded throats in red; the pores invaded by the burst and merge invasions are in blue and yellow, respectively; the pores/throats filled with the displaced fluid in white; the solid phase in gray. The time sequence of the images is from left to right [C].

with gas are shown in red, pink, and white, respectively; the solid phase is in gray. As can be seen, the overall liquid distribution in both networks is similar prior to the breakthrough moment. Yet again, the network saturation is defined as the fraction of the network void volume filled with liquid; the breakthrough moment is denoted as the moment when the gas reaches the network bottom for the first time. The phase distribution in these networks, however, differs when the overall saturation decreases. For the case of $Re = 0.01$, the liquid near the channel inlet is removed first, whereas the liquid is removed randomly in the case of $Re = 10$. At the breakthrough moment, two liquid regions can be identified in the networks: the region near the channel inlet and the region near the channel outlet. At $Re = 0.01$, the vapor concentration at the region near the channel outlet is very high (near the saturated vapor concentration) and thus the drying rate in this region is very low. In contrast, at $Re = 10$ the vapor concentration is almost uniform throughout the channel. As a result, the pores and throats in both regions are invaded by the gas phase, and a fractal-like drying front forms which propagates from the top towards the network bottom.

The simulations with aforementioned pore networks are performed for six different values of the Re. The simulation results are presented as drying curves in Fig. 4.8. As expected the drying time reduces as the Re increases. The rate of reduction depends on the value of Re. The reduction is significant when the Re increases from 0.01 to 1. With further increase of the Re, the reduction in drying time becomes however smaller. This is due to the fact

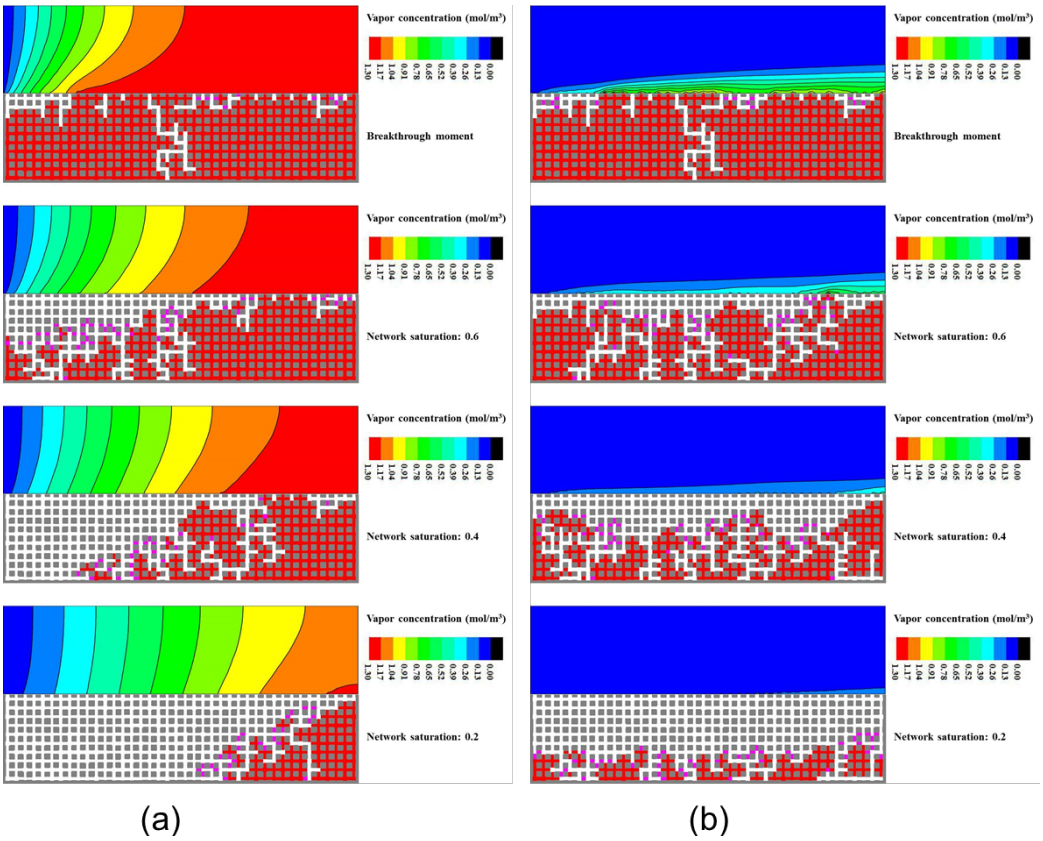

Figure 4.7: Phase distribution in the network and variation of vapor concentration in the channel during drying for (a) $Re = 0.01$ and (b) $Re = 10$ [H].

that the vapor concentration in the channel depends on the Re (see Fig. 4.7). Simulations with three-dimensional pore network models that account for the mixed wettability and for the CVE effect can be found in [98].

4.1.3 Capillary Rings

A sophisticated analysis of the X-ray tomograms revealed that the liquid connectivity over the entire particle packing can be maintained down to very low average liquid contents (see Sec. 3.3). This connectivity is achieved through networks of capillary rings. Only then, the liquid phase disintegrates into several clusters. In this section, this major phenomenon is incorporated into a three-dimensional pore network model and the role that it plays for drying kinetics is shown. The pore network approximates to large extent

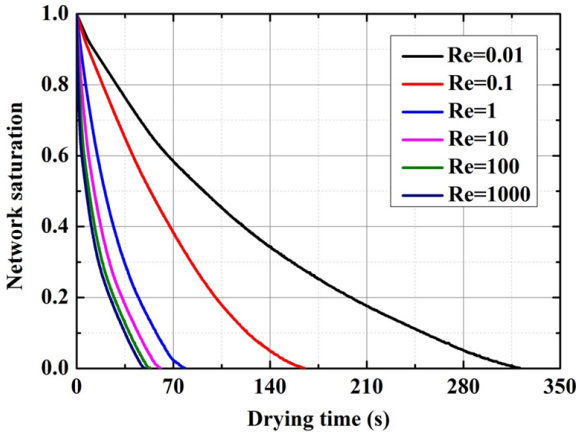

Figure 4.8: Variation of network saturation with respect to drying time [H].

the void space of a particle bed packed regularly with mono-sized spherical particles. The geometrical elements of this network are throats and rings (Fig. 4.9). The throats are cylindrical tubes with uniform length equal to particle diameter. The mean radius of throats is calculated from the particle radius R, $\bar{r} = \sqrt{2R^2} - R$. The throat radii are sampled from a normal distribution with the calculated mean radius and a given standard deviation. The rings are discrete donut-shaped elements and the radius r_r and thickness h_r of the rings are calculated from the half-filling angle α_r and from the particle radius as $r_r = |Rsin\alpha_r|$, where $h_r = R - |Rcos\alpha_r|$. Volume of a liquid ring can hence be calculated as $V = 2(\pi r_r^2 h_r - \frac{3}{\pi}(3R - h_r)h_r^2)$.

The basic version of pore network model for drying is extended by capillary liquid rings. This model accounts for the mass transfer by diffusion in dry regions of the network as well as over the boundary layer, and capillary pumping in liquid-filled regions of the network. The respective drying algorithm operates as follows: the local evaporation rate is obtained by mass balances written at every vapor node. This data marches in time and is used to update saturation of throats, rings and nodes in the network. Capillary rings have identical volume and the liquid-gas interface of the ring is assumed to be flat. Liquid rings maintain the hydraulic interconnectivity between liquid-filled throats – or vice versa – and thus lead to long-distance capillary flow. As a result, mass transfer through the gas-invaded region of the network during drying can remarkably be enhanced. Vapor diffusion in the film region is neglected, because vapor pressure of the gas phase in this region is at the saturated vapor pressure. The liquid rings can evaporate only if they become isolated. At a local level, rings empty following throats. Such an approach can very well describe the transition from the funicular to

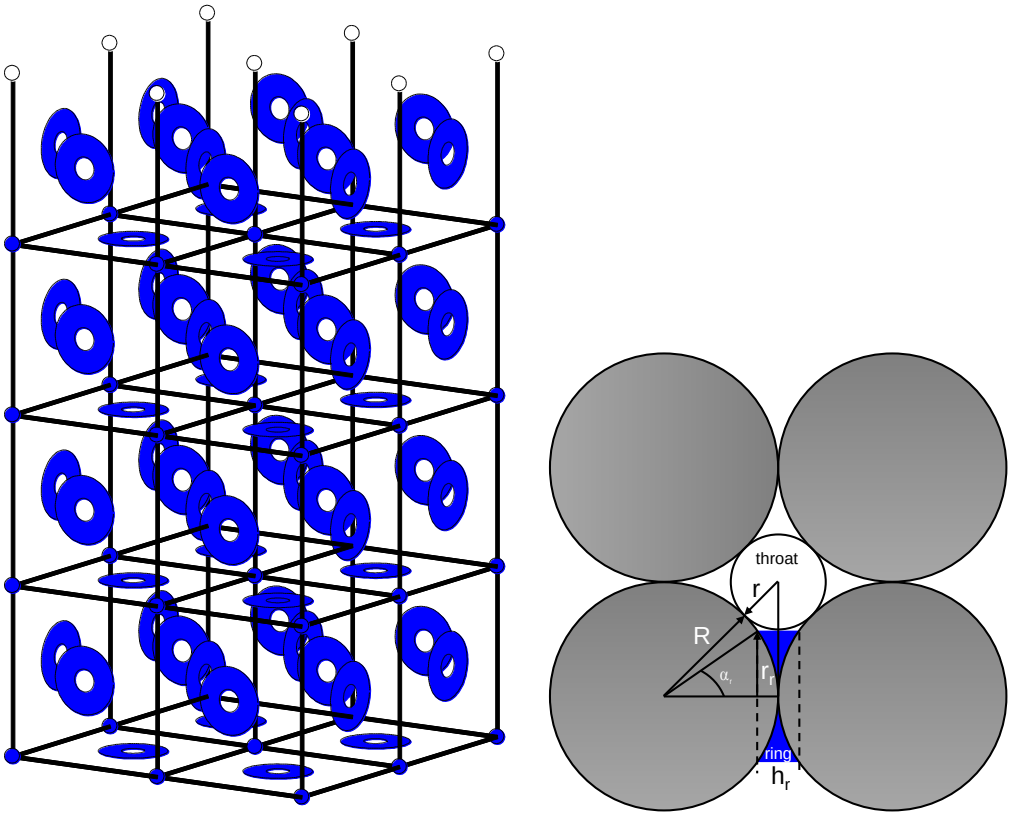

(a) (b)

Figure 4.9: (a) A pore network geometry incorporating liquid rings (throat: black line; ring: blue disk; pore: small circle) and (b) the radius r_r and thickness h_r of the rings are calculated from the half-filling angle α_r and from the particle radius R [I].

the pendular regime for particle aggregates.

Drying simulations are carried out in the limit of capillary-dominated regime. This regime corresponds to situations in which the pressure drop in the liquid phase due to gravity or viscous effects are negligible compared to the capillary effects. Or, in other words, in the capillary-dominated regime capillary pressures are very large compared to the average viscous pressure drops due to the flow. This regime is usually expected when boundary conditions are moderate and porous materials are sufficiently thin. Here a small network of 10×10×20, which is made of throats with a length of 600 μm, mean radius of 124 μm, and standard deviation of 1 μm, is considered. The radius and thickness of the rings are 145 μm and 75 μm, respectively. Drying air with zero moisture is at 20°C and atmospheric pressure. The gas-side

boundary layer has 10 vertical nodes corresponding to a mass transfer coefficient of 2.6×10^{-5} m^2/s. This pore network is utilized to conduct simulations with and without the liquid ring effect.

The simulation results are presented as drying curves in Fig. 4.10. As can be seen, in the pore network model that accounts for the film effect the first drying period is significantly prolonged and thus the drying time is shorten. This is because the hydraulic connectivity of the liquid phase is augmented in the presence of liquid rings. As a consequence, the liquid transport to the evaporation surface by capillary pumping is enhanced. The first drying period lasts as long as the rings saturate, even partly, the network surface. The second drying period begins when the throats and rings dry out from the network surface. For the network without rings, however, the liquid phase splits into small clusters at the early stage of the drying process and hence the liquid flow to the network surface is hindered. The readers interested in details of a three-dimensional pore network model with capillary ring formation and how the presence of these secondary structures affect the phase distribution can refer to [I].

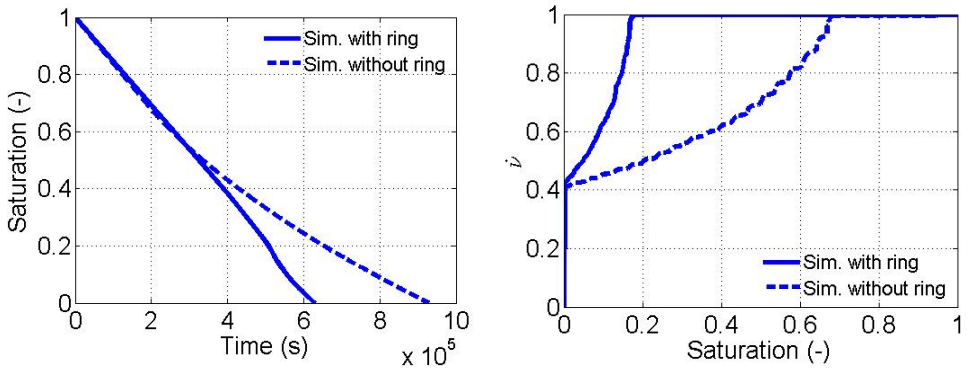

Figure 4.10: Simulated drying curves for regular three-dimensional pore networks with and without rings [I].

4.1.4 Thermal Effect

Considering drying as an isothermal process is meaningful only for limited conditions. That is if the psychometric temperature difference, i.e. the difference between the dry and the wet bulb temperatures, is small, then solid temperature remains nearly constant during the first and second drying periods. Physical examples are the asymptotic behavior in a concurrent belt dryer, or soft drying of woods. Also if drying proceeds slowly, no significant

temperature gradients develop, but product temperature rises uniformly during the second drying period [99]. In real situations drying conditions can be severe, so that non-isothermal effects must be taken into account. These effects can also play a role in processes other than drying, for example, in numerous heat exchange devices such as the loop heat pipe (LHP). In such devices non-isothermal fluid flow is coupled with the phase transition phenomena, i.e., evaporation or condensation.

A major component of a LHP evaporator is the capillary porous wick. The liquid and thermal energy are replenished at opposite sides of the wick. During operation a vapor zone (the so-called vapor pocket) forms inside the wick. Liquid is continuously drawn off by capillary action from the bottom to the liquid-vapor interface. Evaporation occurs at this interface as well as at the surface of the porous wick. The vapor molecules generated as a result of evaporation flow toward the vapor outlet. A pore network modeling of the unsaturated capillary porous wick and of the processes involved under steady-state condition is schematically shown in Fig. 4.11.

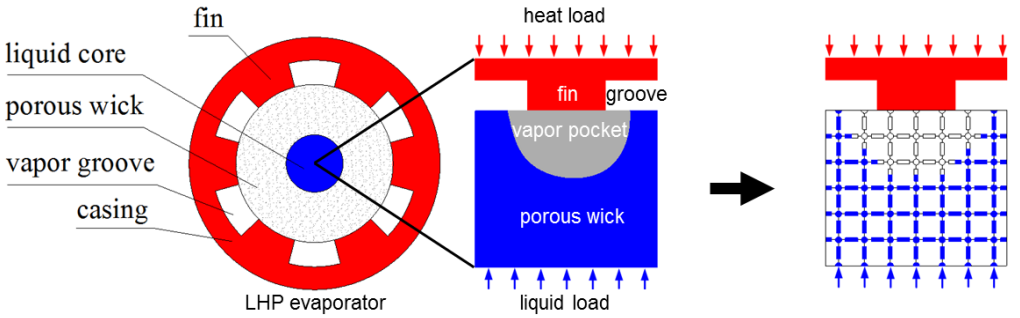

Figure 4.11: Two-dimensional representation of a loop heat pipe (LHP) evaporator (left). Schematically shown are the heat and mass transfer processes in a part of porous wick (middle) and their representation in a pore network model (right) [J].

In this model, the void space of a porous wick is approximated by a two-dimensional Cartesian network of cylindrical throats interconnected via nodes. The mass flow rate through the throats for both the liquid and vapor phases is laminar and thus calculated by the Hagen-Poiseuille law (see Eq. 4.2). The heat conduction in the vapor pocket or in the saturated wick is described by a discrete version of Fourier's law. The following energy balance

equation is written for a node i in the vapor pocket or in the liquid cluster:

$$\sum_j \dot{Q}_{ij} = \sum_j A_{cv,ij} \lambda_{eff,ij} \frac{T_i - T_j}{L} = 0, \tag{4.3}$$

where $\dot{Q}$ denotes the heat rate and j runs over all nodes connected to node i. A_{cv} denotes the heat transfer area and λ_{eff} the effective heat transfer coefficient, which is determined by the parallel heat flux model [100]. The solution of a system of Eq. 4.3 for given boundary conditions yields the temperature distribution. The physical properties of vapor and liquid phases are updated based on the computed temperature and pressure fields. At each liquid-filled throat the evaporation rate is determined by energy balance equation. By solving linear system equations of mass balance the liquid and vapor pressure fields are calculated (Eq. 4.2). By comparing different pressure between gas throat and liquid throat with capillary pressure, throats are filled or emptied. The liquid phase is thus updated and checked for any change in phase distribution. In case of a change these steps are iterated, otherwise the calculation is terminated.

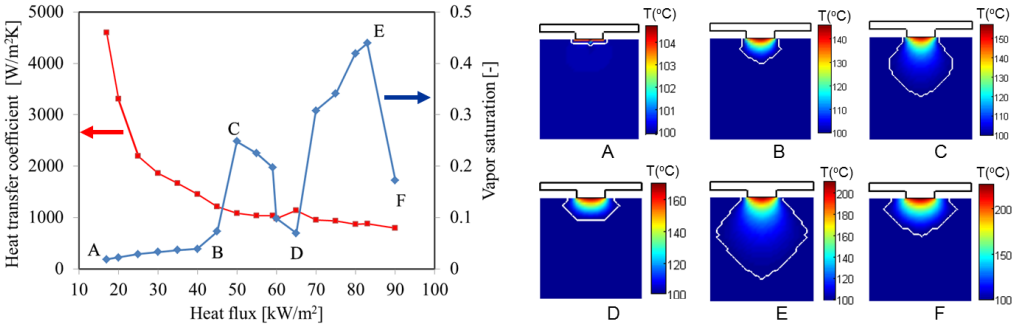

Figure 4.12: The effective heat transfer coefficient and vapor saturation as a function of the heat load (left). Temperature distribution for different values of the heat load (right) [J].

The pore network simulations are carried out to study the impact of the heat load (heat flux) on the heat and mass transfer inside a capillary porous wick (see Fig. 4.12). With increasing the heat load, the vapor pocket primarily grows toward the network bottom and meanwhile the vapor reaches the outlet through a narrow neck. With further increasing heat load, several liquid throats near the neck empty and thus the vapor pocket starts to expand in the lateral direction. This leads to a decrease of the pressure inside the vapor pocket and several empty throats are refilled at the same time, such

that the vapor pocket shrinks. As the heat load increases further, the vapor pocket expands again. With an even higher heat load, the liquid throats at the surface are finally invaded and the hydraulic resistance of the vapor phase decreases again. Therefore, the vapor pressure inside the pocket drops and several empty throats are refilled by liquid, which leads to a decrease of the vapor pocket size. This inflation and deflation behavior of the vapor pocket repeats with further increasing heat load. To quantify the evolution of the vapor pocket for increasing heat load more precisely, the vapor saturation is calculated and shown in Fig. 4.12. For a given value of the heat load, vapor saturation is defined as the ratio of the vapor volume to the total void volume in the network. One can clearly see that as the heat load increases, the vapor saturation fluctuates due to the inflation/deflation of the vapor pocket described before. Such behavior of the vapor pocket directly influences the effective heat transfer coefficient of the wick. As the heat load increases, the distance between the heat source (fin) and the liquid-vapor interface inside the porous wick increases first and then fluctuates. Consequently, the thermal resistance between the fin and the evaporation front increases first – due to the lower thermal conductivity in the vapor phase – and then fluctuates.

These pore network simulations are pertinent only to the limiting case of the dry-out operating regime of the wick. The so-called two-phase zone regime is an intermediate between the dry-out regime and the saturated wick. In this two-phase zone regime, the bottom surface of the fin is partially wetted; therefore, the effective heat transfer coefficient stabilizes at high value before decreasing significantly during the dry-out regime [101, 102].

The influence of the heat load, the porous structure, as well as the liquid inlet pressure and temperature on the heat transfer coefficient efficiency is investigated and discussed in [J] and [103]. The pore network model considered here is inspired by a typical situation in LHP evaporator, this model can however be adopted and refined further to account for other physical effects. For instance, an extension of this model by pore condensation is discussed in next section.

4.1.5 Pore Condensation

Condensation of vapor in pores is another major physical effect that a capillary network model is able to describe. During drying of a porous material an uneven temperature distribution can lead to a non-uniform distribution of the saturated vapor pressure. At a given temperature pore condensation occurs when the vapor pressure exceeds the saturated vapor pressure – as temperature increases the saturated vapor pressure rises as well. This effect has already been incorporated into non-isothermal pore network models for

convective (or hot air) drying, but only partly [30, 104, 105]; in these earlier models the liquid produced by condensation in full pores with liquid-gas interfaces is completely ignored. In the present pore network model, on the other hand, the internal vapor condensation is fully accounted for. This is achieved by coupling the available discrete events with the new liquid invasion rules. Note however that the pore condensation due to the Kelvin effect is neglected in all these published pore network models. Another difference between this pore network model and the previous competing models is that superheated steam is used as the drying agent, instead of hot air. From practical standpoint, application of superheated steam instead of hot air has several benefits. It yields a better product quality, shorter drying time, and higher energy efficiency [106]. As shown in Fig. 4.13, the superheated steam drying process typically consists of three periods: surface condensation, surface evaporation, pore drying [107]. Since our focus here is on the pore condensation phenomenon, only the model components relevant to the latter period are briefly presented. Details on the other model components and the numerical solution method can be found in [K] and [103].

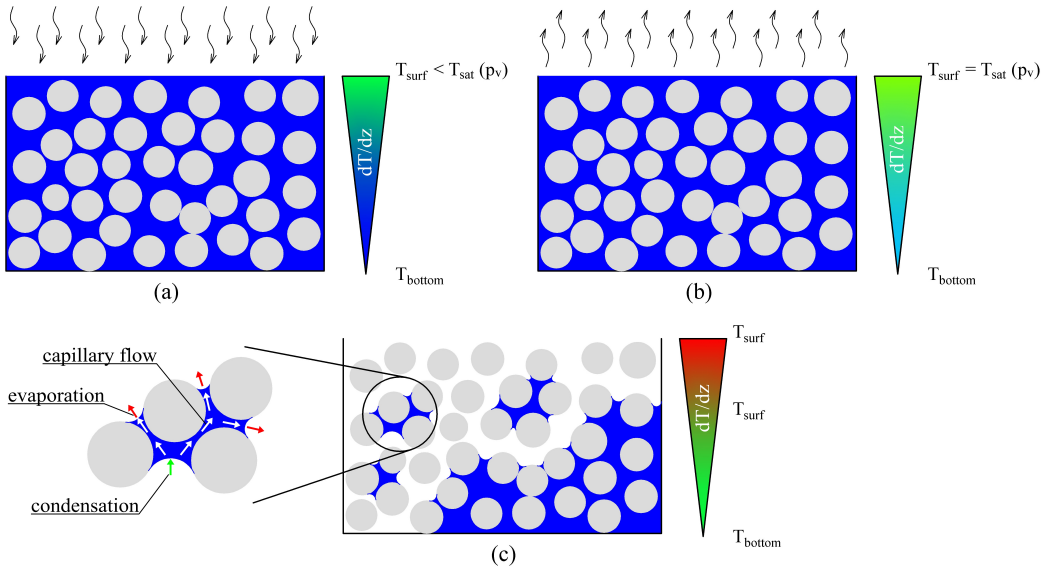

Figure 4.13: Pictorial representation of surface condensation (a) and surface evaporation (b), as well as of local events that occur inside a porous medium during superheated steam drying [K].

The rate of pore evaporation or pore condensation, $\dot{M}_{evp,con}$, is calculated

by the modified Hertz-Knudsen equation at the quasi-steady state:

$$\dot{M}_{evp,con} = \pi r^2 \frac{2\delta_{evp}}{2-\delta_{evp}} \sqrt{\frac{\widetilde{M}_v}{2\pi \widetilde{R} T}} (p_v^*(T) - p_v), \tag{4.4}$$

where δ_{evp} denotes the evaporation coefficient, which is determined from evaporation experiments. In fact, this coefficient accounts for various effects, such as the reflection of liquid molecules or the replacement of vapor molecules, which lower the evaporation rate compared to that in vacuum [108, 109]. In Eq. 4.4, if the liquid temperature is lower than the boiling temperature (saturation temperature) at vapor pressure, then condensation occurs. In contrary, if the liquid temperature is larger than the boiling temperature at vapor pressure, then evaporation takes place. The vapor pressure field is obtained from the mass balance equation written for each empty or partially filled pore. The vapor mass flow rate through pores are calculated by the Hagen-Poiseuille law – note that for superheated steam drying there is no air in the drying agent. The liquid transport is driven by capillary action where the surface tension depends on the liquid temperature.

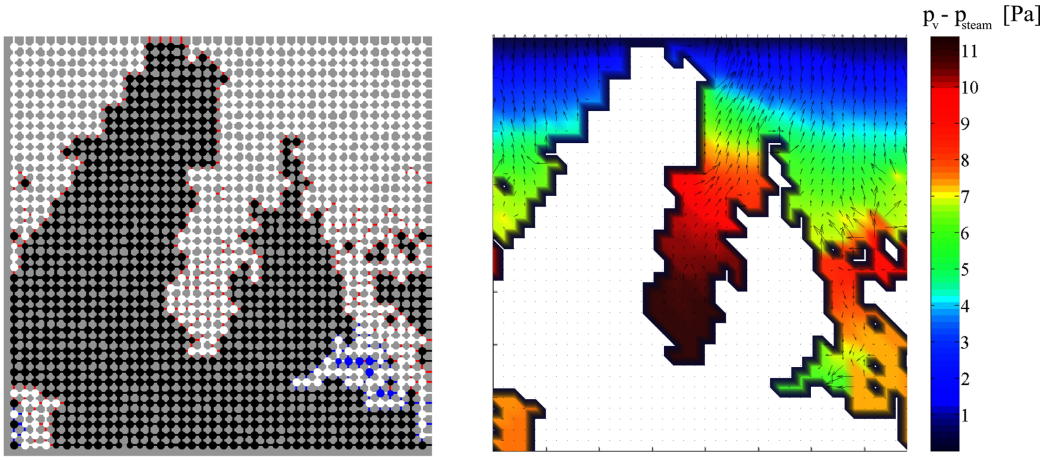

Figure 4.14: (a) Liquid phase distribution and (b) vapor pressure field. The evaporating and condensing throats/pores are shown in red and blue, respectively. The arrows indicate local vapor velocity [K].

Simulations are conducted with a 40×40 pore network. The length of throats is 1 mm and the pore and throat radii are sampled from normal distributions with mean radii of 250 μm and 100 μ, respectively, and standard deviation of 10 μm for both pores and throats. The steam pressure

is 1 bar. The phase distribution and the vapor pressure field at network saturation 0.6 are presented in Fig. 4.14. As can be seen, most evaporating throats/pores are located above the condensing throats/pores. This is due to the temperature gradient throughout the network height. The liquid is divided into clusters by capillary action and thus vapor fingers appear at the evaporation front. The temperature at the upper throats is higher than the boiling temperature, whereas the temperature at the lower throats/pores may be lower. As a result, evaporation takes place at the upper throats containing menisci and condensation occurs deeper inside the network. Also, a non-monotonic distribution of the vapor pressure is observed which leads to a local downward vapor flow.

Though the local condensation is fully accounted for in the drying algorithm, numerical stability requires short time steps resulting in long computational times. Therefore, this model version is not yet suitable for product-scale simulations where much larger pore networks are required.

4.1.6 Salt Transport and Accumulation

Prior to pore network simulations, let us schematically trace the main physical effects/events that may appear during drying of a simple porous medium which is saturated initially with salt solution. As can be seen in Fig. 4.15, this medium consists of two pores that are hydraulically connected. Solvent evaporation occurs from the top side of the medium. The evaporation leads to a local increase of concentration in both pores. The combined effect of capillary flow from the big pore to small pore and back-diffusion into the liquid results in a concentration field. When saturation in the small pore reaches the saturation level, excess solute is immobilized in this pore as salt crystals.

A pore network model that accounts for all these effects is described next. This model is then used to predict the influence of process condition and pore structure on the evolution of accumulation sites formed within a porous matrix during the convective drying process. In this pore network model, capillary flow of the pore liquid (Eq. 4.2) and diffusion of the vapor molecules (Eq. 4.1) are coupled at the menisci depending on the available capillary pressure (Eq. 2.7). The migration of salt in the network is modeled by a one-dimensional transient advection (driven by capillary flow) and diffusion (driven by concentration gradient) equation. The salt concentration c is calculated by

$$\frac{\partial c}{\partial t} = -u\frac{\partial c}{\partial z} + D\frac{\partial^2 c}{\partial^2 z}, \tag{4.5}$$

where u denotes the average velocity of the liquid in the pores, referred to

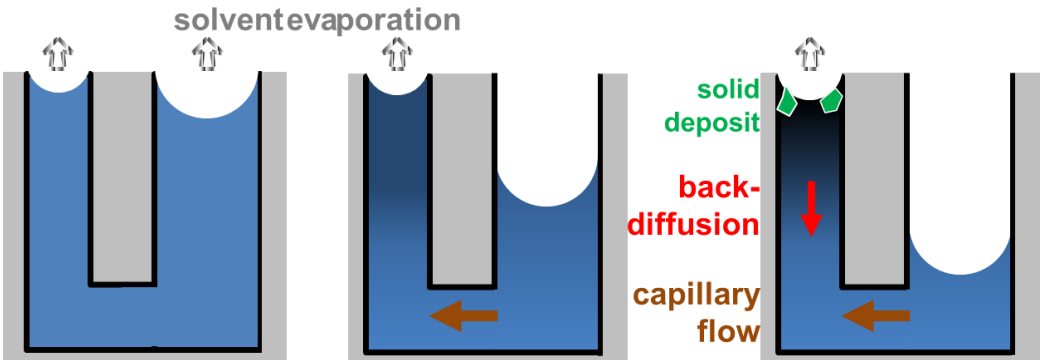

Figure 4.15: Schematic of main physical effects that occur during (slow) drying of a porous medium in which pore water is aqueous salt solution with an initial concentration much lower than the saturation level.

as the interstitial or superficial velocity of the liquid, D the binary diffusion coefficient of salt in water. In Eq. 4.5 the hydrodynamic dispersion is neglected. This assumption holds when $\|u\bar{r}/D\| \ll 1$, where $\bar{r}$ is the mean pore size of the medium. Ion adsorption to the pore walls is also neglected, because porous materials with wide pores, say wider than 1 μm, are considered here. Since electroneutrality is assumed, there is no need to treat the transport of ions separately. A discrete version of Eq. 4.5 is applied to each liquid throat to calculate the corresponding salt concentration. This additional sub-discretization step is however computationally unfavorable. The numerical accuracy of this pore network model has already been assessed by several test problems, see [L, M].

A 10×10 pore network with randomly distributed throat radii (1±0.1 μm) and a uniform throat length of 100 μm is initially saturated with 90% NaCl solution. The pore network is open to ambient air from the top side and the evaporation process takes place thereon. In order to achieve a low rate of drying, the air temperature is at 25°C and the thickness of the gas-side boundary layer is 10 mm (i.e. significantly larger than network height). In this situation, capillary forces dominate over viscous forces in the liquid phase. A substantial fraction of liquid is thus pumped to the network surface because the hydraulic connection between liquid clusters in the network and throats at the surface is maintained (see Fig. 4.16). As a result, a significant amount of dissolved salt is transported to the network surface. Solidification occurs when the saturation level is reached in the pores. The salt accumulation is non-uniform and very significant at the network surface, because the high initial concentration of the solution gives no room for transport of

ions into the bulk liquid by back-diffusion. By contrast, for a lower initial concentration of salt solution, the low rate of drying allows the concentration gradient to level out to a greater extent by back-diffusion. Hence, a more uniform solidification pattern is expected throughout the network.

To ensure a high rate of drying, the air temperature is increased to 80°C and the boundary layer thickness is decreased by one order of magnitude. In the first drying period the evaporation front propagates throughout the network since capillary flow is hindered (see Fig. 4.16). As a result of local solvent evaporation a thin crust forms homogeneously near the network surface. In this period the time scale is too small to allow for any redistribution of ions by back-diffusion. During the second period the drying rate drops significantly and capillary flow becomes relevant, advecting the salt ions to the evaporation zones located beneath the network surface. This period is again short, so that back-diffusion cannot reduce the salt accumulation. For a very high drying rate the salt crystals may form uniformly in the entire network as ion transport can significantly be suppressed in the liquid phase.

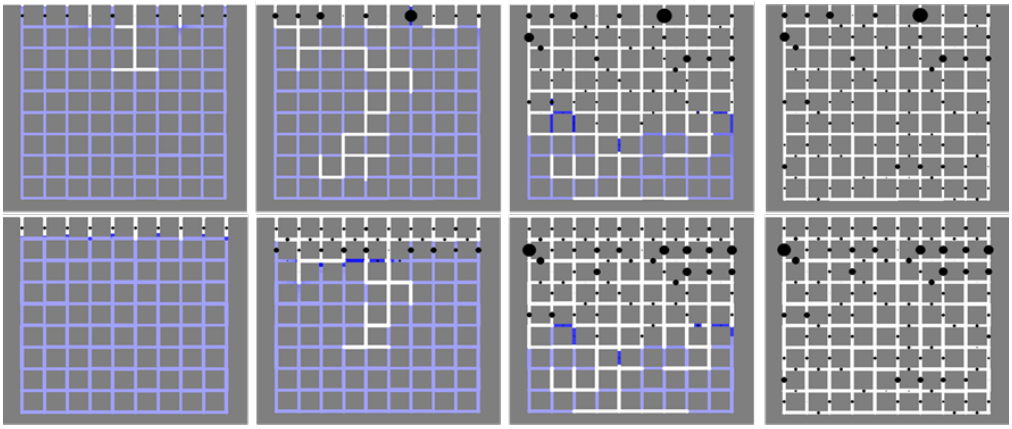

Figure 4.16: Time evolution of salt solution and solidified deposits within a small pore network subjected to slow drying (top row) and fast drying (bottom row). Drying is from the top and network saturation decreases from left to right. Salt deposits are visualized as black disks – their size indicates deposit mass. Different shades of blue represent the salt concentration in the liquid – a darker color indicates a higher concentration [L].

In order to study the effect of pore structure on the salt distribution during drying, a pore network of size 30×30 with a bimodal pore size distribution is considered. In this network vertical and horizontal macro-throats isolate micro-porous regions. The size distribution of the throats located in the micro-porous regions is identical to that in the network with mono-modal

pore size distribution. The macro-throats are randomly distributed and their radii follow a normal distribution function with a mean value of 2 μm and standard deviation of 0.1 μm. All throats in macro- or micro-regions have identical length. Initial salt concentration is reduced to 20% of the saturation concentration to enhance dissolved salt diffusion. Figure 4.17 shows pore network simulations that are conducted at two different drying rates, referred to as slow and fast drying. These conditions are set by varying the drying air temperature and the boundary layer thickness.

Slow drying results in a noticeable accumulation of salt at the network surface, especially in the left region where pores of smaller diameters are located. This inhomogeneous distribution of salt is resulted from the transport of dissolved salt by capillary flow from the interior towards the network surface, leading to supersaturation and solidification. As drying proceeds, the micro-porous regions become hydraulically isolated. The isolated regions cause screening effect for the larger liquid clusters, which are located deep in the network. This reduces the time for salt diffusion and hence for establishing the concentration gradients. This effect leads to a uniform distribution of salt within the micro-porous regions.

For fast drying, the simulation results show a considerable amount of salt crystals beneath the network surface. This feature is similar to what has been observed for the pore structures with mono-modal pore size distribution. One can also see a pronounced accumulation of salt crystals in the top side of the micro-porous regions, but negligible accumulation in the macro-channels. This is due to the fact that almost all dissolved salt is transported to the micro-porous regions during drying.

4.1.7 Pore Network Modeling of Wetting

A dynamic pore network model is developed to simulate the wetting process in single or dual pore networks. A single pore network is generated with features that mimic the pore structure of the micromodel described in Sec. 3.2, see Fig. 4.18. This type of pore network appears homogeneous at the macroscopic scale. On the other hand, interacting dual pore networks (or dual-porosity pore networks or two-layered pore networks) consist of two hydraulically linked, distinctive regions, each with a specific pore size distribution and separated by a sharp vertical capillary interface – such medium is heterogeneous at the macroscopic scale. These networks are initially empty and exposed to a liquid reservoir from one end and open to air from the other end. The dual pore networks are connected to the liquid reservoir from either only the fine region or both the fine and coarse regions. The dual network with its fine region connected to the reservoir is 10×100 mm; the

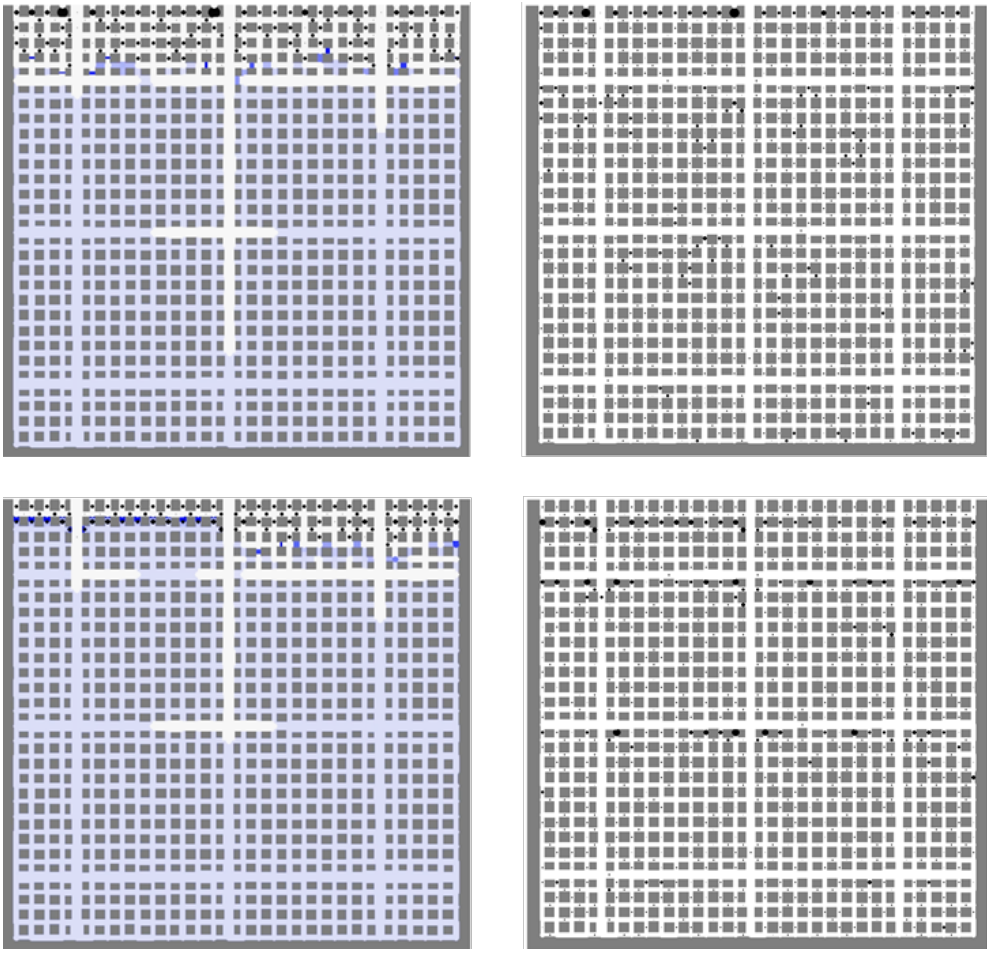

Figure 4.17: Time evolution of salt solution and precipitated deposits within a pore network with isolated small-pore regions, which is subjected to slow drying (top row) and fast drying (bottom row). Drying is from the top and network saturation decreases from left to right. Salt deposits are visualized as black disks – their size indicates deposit mass. Different shades of blue represent the salt concentration in the liquid – a darker color indicates a higher concentration [M].

pore radius distributions in the fine and coarse regions are respectively 25±1 μm and 125±5 μm, and the pore length is 0.5 mm. The other dual network is 4.9×9.9 cm; the pore radius distributions in the fine and coarse regions are respectively 80±10 μm and 48±6 μm, and the pore length is 1 mm. The water uptake capacity of the former dual network is equal to its void volume, whereas the uptake capacity of the latter dual network is smaller than its void volume.

In the pore network model for wetting the liquid transport in each capillary (throat) is driven by difference in Laplace pressure as opposed by viscous drag force. Inertial and gravitational effects are neglected. The wetting process takes place under isothermal conditions and perfect wetting is assumed. The wetting algorithm is as follows: the mass balance equations are collected for all liquid nodes, leading to a system of linear equations. The solution of these equations yields the pressure field in the entire network. After each liquid displacement the pressure field calculation is repeated. When the pressure profile is known, stationary menisci, invading menisci and receding menisci are identified. The time step size is chosen such that only one throat is completely emptied or filled in each time step. The other invading or receding menisci partly fill or drain the corresponding throats with respect to their flow rates and the time step. Another discrete pore-level event, called breakage, is possible when a throat becomes empty. This event occurs if the pressure in the adjacent liquid pore is not sufficiently large to sustain the liquid connectivity. The breakage results in formation of a meniscus in one or more neighboring full throats. A description of this algorithm can be found in detail in [F] and [63].

Figure 4.19 shows the measured and simulated evolution of the total liquid volume over time inside the single pore network and the etched micromodel for three different mixtures of ethanol and water. The spatial distribution of the liquid mixture with 80% ethanol mass fraction is also shown in Fig. 4.19; simulations with the same pore network but with different mass fractions of ethanol result in similar phase distributions, see [63]. The simulation results obtained from the single pore network for all test mixtures compared favorably with experimental observations processed by an image analyzer, though the wetting tends to be rather slower in the experiments. The wetting process starts from the smallest surface pores because their entry capillary pressures are the highest. This process advances pore by pore according to their radii and their distance from the network surface until the network becomes fully saturated with the liquid. During this process the rate of pore invasion by the wetting liquid is dictated by the competition between capillary and viscous forces. In other words, the liquid flow rate adjusts itself to attain a state of equilibrium between capillary and viscous forces. At the onset of the wetting process the time-invariant capillary forces drive the liquid into the network, and later the advancement of menisci is slowed down by viscous drag forces. The wetting kinetics of this sort of pore network with nearly sharp front follows the classical Lucas-Washburn law, i.e. liquid volume $\propto$ time$^{0.5}$.

In dual pore network with a series arrangement of fine and coarse regions (Fig. 4.20) a wetting front with limited width forms which preferentially

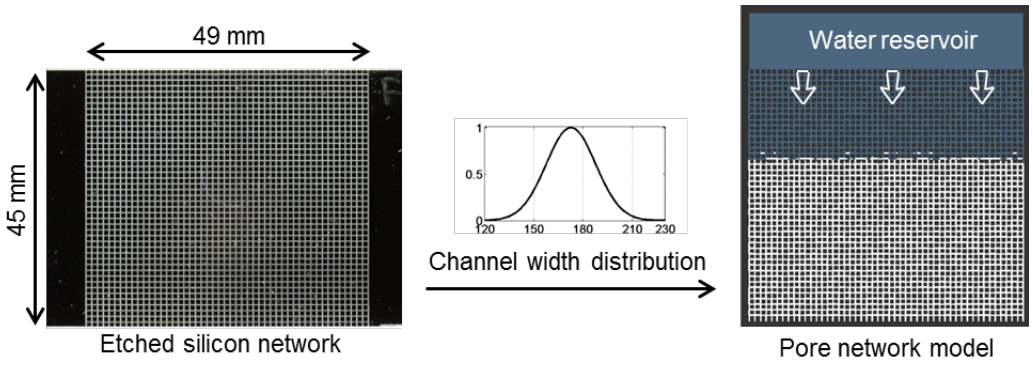

Figure 4.18: Single pore-network structure is generated based on the data obtained from the etched silicon micromodel; adapted from [63].

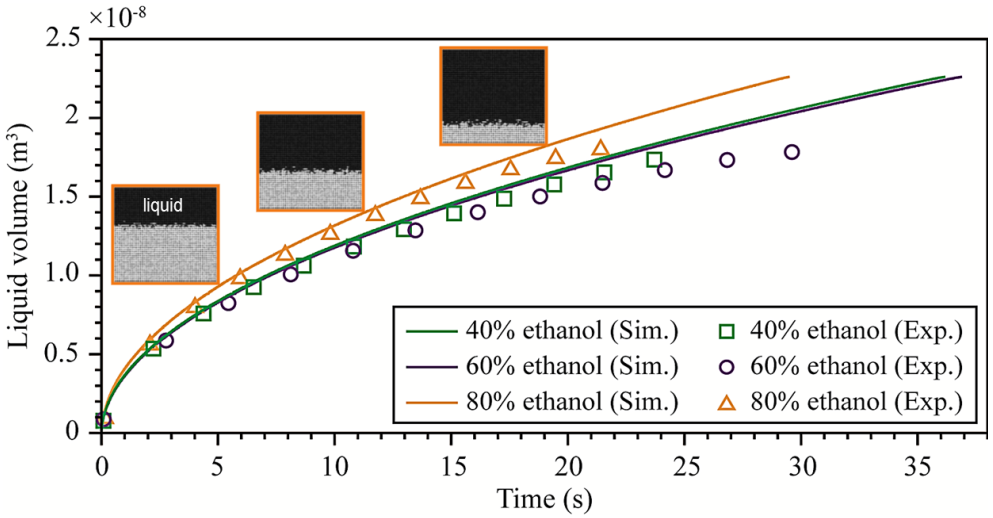

Figure 4.19: Evolution of the liquid volume over time for three different mixtures of ethanol and water. Micromodel measurements (Exp.) and pore network simulations (Sim.) are shown by symbols and lines, respectively. The spatial distribution of the liquid mixture with 80% ethanol mass fraction is also shown here; adapted from [F].

propagates towards the coarse region. This process continues until the fine region becomes completely saturated with the liquid. The liquid propagation advances since the liquid pressure in the reservoir is higher than the liquid pressure in the menisci located in the pores of the coarse region. During this period the wetting front spans almost the entire coarse region. This fractal morphology of fluid-fluid displacement is due to the fact that the

liquid transport in the coarse region is dominated by capillarity.

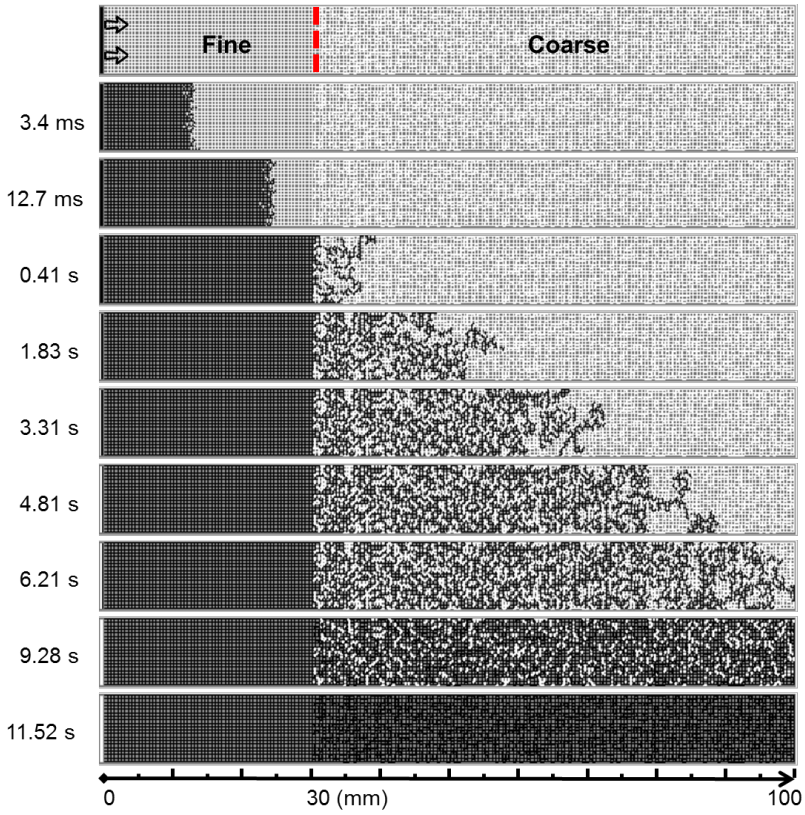

Figure 4.20: Simulated transient liquid distribution for the dual pore network where only its fine region is connected to a liquid water reservoir with capacity equal to the void volume of the network. Liquid-filled and empty pores are shown in black and white, respectively [Q].

In dual pore network with a parallel arrangement of find and coarse regions (Fig. 4.21) all surface throats at the inlet of both fine and coarse regions are invaded by the liquid. As long as the liquid exists in the wetting reservoir two distinct wetting fronts with similar feature form, both of which advance towards the other end of the network but the one in the fine region leads during this period of the wetting process. When the wetting reservoir has emptied a second front develops in the coarse region as a result of liquid pumping from the coarse to the fine region. During this period the coarse region acts like a secondary wetting reservoir making the fine region completely wet. Afterwards, the local displacement of the liquid in the coarse region continues until the equilibrium state is achieved.

Further pore network simulations of wetting are conducted with an inten-

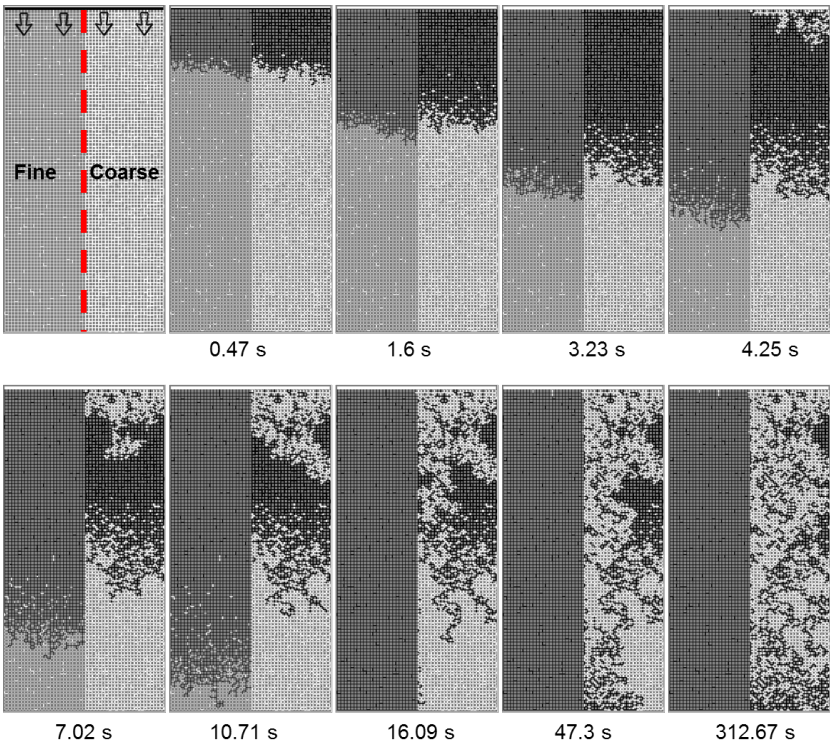

Figure 4.21: Simulated transient liquid distribution for the dual pore network where its both fine and coarse regions are connected to a liquid water reservoir with capacity less than the void volume of the network. Liquid-filled and empty pores are shown in black and white, respectively [Q].

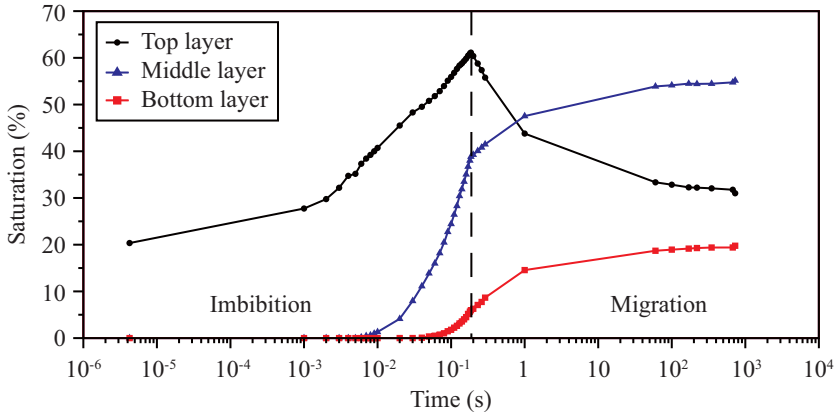

Figure 4.22: Simulated saturation profiles obtained from the layered network that mimics the pore structure of the wipe-substrate [J].

tion to better understand the lotion transport and redistribution in wet wipe substrates. The network size is 80×10 nodes with laterally period boundary conditions. This network size corresponds to about 12×0.80 mm^2 of vertical cross-section area of the subtract. The throat radii in the network are assigned according to the pore size distribution acquired from the X-ray images (see Sec. 3.4). The simulation results, which are presented as the time evolution of lotion saturation for each layer in Fig. 4.22, are averaged over fifteen realizations of the pore network with the same pore size distribution. The real physical properties of the lotion are used in the simulations [63]. The amount of lotion in the reservoir is equal to the total lotion volume of the substrate measured in Sec. 3.4. Before the reservoir is emptied, the lotion invades all three layers, starting from the top layer. When the liquid saturation has reached at least 5% in the bottom layer, the liquid starts migrating from the top layer towards the middle and bottom layers. Afterwards, the lotion flows from the top layer to fill the small pores in the middle and bottom layers. Over the course of time, the middle layer is filled with lotion to the highest possible degree since this layer contains relatively small throats. Such pore network simulations can be performed to study the impregnation of porous matrices or the rehydration features of dried products.

4.1.8 Combined Wetting and Drying

The pore network models, as described in preceding sections, are able to successfully predict wetting and drying of a capillary porous medium. In this section, this capability is extended to a complex situation, where the wetting and drying processes occur simultaneously. This nontrivial problem is of relevance to various product formulation processes such as agglomeration of powder particles or impregnation of porous supports in a spray fluidized bed. During these processes a pure liquid binder or an agent solution is sprayed onto the fluidized bed in the form of small droplets. If droplets come into contact with porous particles, they may penetrate into the pores and concurrently evaporate from the droplet surface or from the surrounding wet pores. Pore network simulations of wetting and simultaneous drying are conducted with different pore structures and for various values of the droplet viscosity. Simulations are also performed with a liquid droplet that contains a dissolved solute.

The wetting of pore structure by a pure liquid droplet with simultaneous drying is presented first. The pore structure is represented by a network of cylindrical throats and spherical pores. The droplet volume is equal to the void volume in the network. For a detailed description of the network structure and the physical properties of the liquid, see [110]. During the

wetting-drying process two distinct regimes are essentially recognized, depending on which process (i.e. wetting or drying) is dominant. As long as the droplet is present at the network surface, the wetting regime is dominant. The process is controlled by drying when the droplet is removed from the network surface by evaporation or infiltration. From another standpoint, the liquid is added to the network during the wetting regime, whereas during the drying regime the liquid is given away from the network.

Figure 4.23 demonstrates the wetting-drying process in a mono-modal network. During the wetting stage, capillary flow transports the liquid into the throats and, thus, the network becomes completely saturated with liquid within a few milliseconds. Since viscous forces are almost absent, nearly no time is left for evaporation to take place in the surface throats connected to the droplet (blue line in Fig. 4.24). In the drying regime, gas invades through the surface throats into the network and meanwhile the liquid is transported to the network surface by capillary forces. In the late drying regime, the separate liquid clusters dry out one-by-one from the surface, and drying rate drops due to the additional diffusion resistance. As evidenced in Fig. 4.24, the liquid viscous effect impacts significantly the wetting-drying kinetics. Two limiting values of the viscosity can respectively approximate water and highly viscous binder solutions, for instance. If the liquid viscosity is negligible, wetting occurs almost instantly, but drying lasts for longer time. For high viscosity, on the other hand, the liquid migration into the network is substantially limited and thus the liquid resides for a long time on the network surface.

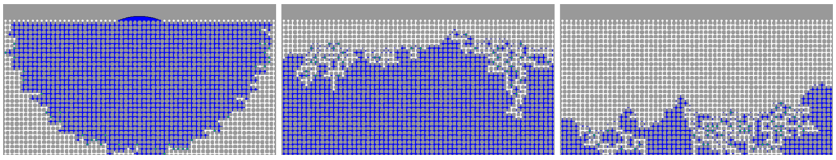

Figure 4.23: Wetting and simultaneous drying of a mono-modal pore network with a droplet [R].

The time-scales of wetting and drying regimes can also be influenced by the pore structure. Figure 4.25 shows the simultaneous wetting and drying behavior of a pore structure with bi-modal pore size distribution. In this pore structure, micro-porous regions are wrapped with macro-throats. During wetting, the liquid invades toward the network bottom by preferentially filling the interior macro-throats. In the drying period, the macro-throats almost right away give their liquid into neighboring small throats. Such pore network simulations are carried out for bi-modal pore structures, in which micro- and

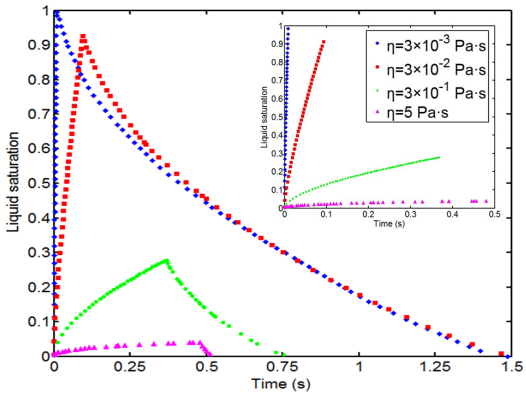

Figure 4.24: Evolution of liquid saturation during wetting and simultaneous drying of a mono-modal pore network. Symbols (lines) correspond to different viscosity values of a liquid droplet deposited on the network surface [R].

macro-throats are spatially correlated in different ways – see [R].

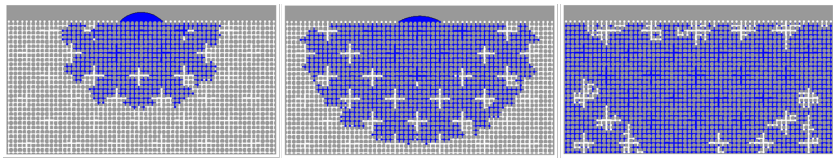

Figure 4.25: Wetting and simultaneous drying of a bi-modal pore network with a droplet [R].

The pore network model of wetting-drying is combined with a solute in order to describe the impregnation process of porous substrates. This process consists of the loading of a porous substrate with a droplet containing volatile solution and the subsequent drying step leaving the solidified deposit inside the pores. A pore network simulation of this process with salt solution is shown in Fig. 4.26. Liquid capillary flow transports the dissolved salt through the surface throats into the network. Towards the end of the loading stage the salt concentration in the droplet reaches the saturation level. Therefore, salt is deposited at the network surface prior to the drying stage. As the drying proceeds, more salt crystals form which span almost the entire regions saturated with liquid solution. Important influence factors, e.g. drying conditions and pore structures, are discussed in [S].

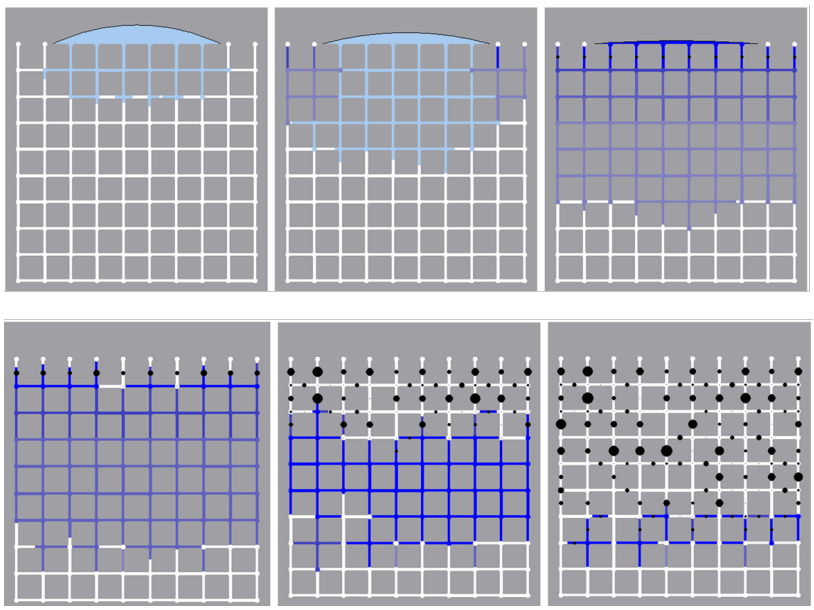

Figure 4.26: Wetting and simultaneous drying of a pore network with a droplet containing dissolved salt. Drying is from the top and network saturation decreases from left to right. Salt deposits are visualized as black disks – their size indicates deposit mass. Different shades of blue represent the salt concentration in the liquid – a darker color indicates a higher concentration [S].

4.2 Continuum Model Parameters

Within the frame of macroscopic continuum approach for drying, a partially saturated porous medium is considered homogeneous and the heat and mass transfers are driven by gradients in state variables – like temperature and liquid saturation – and controlled by a set of parameters. These parameters have a clear physical meaning, describing either the fluid transport phenomena (i.e. intrinsic permeability, relative liquid and gas permeability, vapor diffusivity and thermal conductivity) or the local equilibrium properties (i.e. capillary pressure and desorption isotherm). However, it is not straightforward to determine the values of these parameters, because they depend on the morphological and surface properties of the porous material as well as on the liquid saturation that changes smoothly with time and space. A natural question arises now as to how these saturation-dependent parameters (or constitutive closures) can be measured or predicted for a given porous medium.

Originally these parameters are determined from experimental data us-

ing empirical approaches [111] or inverse methods [112, 113]. With advances achieved later in the pore-scale models these parameters are predicted with the help of discrete models. Nowicki et al. [114] are the first to calculate three macroscopic transport parameters (capillary pressure, relative permeability, and effective diffusivity as functions of liquid saturation) for drying from several simulations on 2D pore networks of biconical pore bodies with uniformly distributed pore radii. The estimates of these parameters are dependent on the drying rate and on the slices cut out of the drying network. Later, this approach has been adopted to compute these parameters from multiple realizations of 2D pore networks of cylindrical pore throats with normally distributed pore radii [115]. The obtained parameters together with a saturation-dependent function for the sorption isotherm, which is predefined by introducing artificial sorbed water, are used to conduct drying simulations with the continuum models; the respective saturation profiles and drying kinetics are inadequately assessed. Though these works are first attempts in this direction, two main criticisms can be applied to them: First they are limited to 2D systems that cannot properly describe the percolation properties of the involved fluids. Second, due to the small size of these 2D systems, they cannot be considered as an REV, in which the state variables are computed. For these reasons, simulations with large 3D pore networks are obligatory.

As another class of discrete models, a bundle of capillary tube model is used to calculate the effective parameters of a drying porous medium. In this model, liquid is retained in the smallest pores due to capillary pumping, implying that the computed effective parameters are unique functions of the saturation, i.e. independent of drying rate. Then, the continuum drying model is solved with the estimates of effective parameters; good correspondence is shown as regards to moisture profiles and drying rates [116]. An advantage of this type of discrete model is that it allows for describing the influence of pore volume distribution on the values of the effective parameters. However, the role of other morphological properties characterizing a real three-dimensional pore structure, such as pore coordination number, cannot be studied.

The macroscopic parameters of the continuum models for wetting are mainly permeability, relative permeability, and capillary pressure curve. Similar to drying, determination of these parameters is one of the challenging topics. One way to determine these parameters is to opt for laborious experimental techniques such as porous plate method, mercury injection, etc. [117, 118]. Another way is to utilize the various empirical correlations, which are system-dependent and include other unknown coefficients [119, 120, 121]. These coefficients are often correlated to either experimental data [120] or

numerical solutions [44, 122] by fitting. These parameters can also be computed by exploiting pore network simulations. For this purpose, the most conventional pore network model, which is based on quasi-static invasion rules, has mainly been used. These rules fulfill the assumption of local capillary equilibrium underlying the classical continuum model of two-phase flow in porous media (e.g., [123, 124, 125]). Others also computed the effective parameters from dynamic pore network modeling (e.g., [126, 127]).

In the following methods are introduced to determine the macroscopic parameters of a capillary porous medium by means of pore network simulations.

4.2.1 Two-equation Continuum Model for Drying

A simple version of the broadly accepted continuum model (CM) of drying, which is originally developed by Whitaker [9] and later extended by Perré [11] mainly for wood drying, is revisited in this section. This model describes the moisture transport in a capillary porous medium in the absence of gravity which is exposed to soft drying conditions. Under these conditions drying occurs slowly, so that a uniform temperature profile and constant gas pressure may approximately be maintained inside the medium during the entire drying process. Thus, no additional equations for the heat transfer and for the air transport need to be solved.

To derive this CM, the conservation of mass is written for both liquid and gas phases that coexist in the REV. The respective mass transfer is considered to be dominant in the direction perpendicular to the evaporation surface, i.e. z direction. The component mass balance for the liquid phase in local formulation yields:

$$\frac{\partial \rho_{\ell c}}{\partial t} = -\frac{\partial}{\partial z}(\rho_{\ell c} u + j_{\ell c}) - \Gamma, \tag{4.6}$$

where $j_{\ell c}$ denotes the liquid diffusion flux, which is driven by concentration difference. Assuming that the liquid transport is dominated by advection, the diffusion term can be neglected. Γ denotes the sink term, which is caused by evaporation. $\rho_{\ell c}$ is the liquid mass density calculated by

$$\rho_{\ell c} = \frac{m_{\ell c}}{V}, \tag{4.7}$$

where $m_{\ell c}$ and V denote the liquid mass and the total volume, respectively. The total volume can be expressed by

$$V = \frac{V_{void}}{\epsilon}, \tag{4.8}$$

where V_{void} and ϵ denote the void volume and the local porosity, respectively. The liquid mass can be expressed by

$$m_{\ell c} = \rho_\ell V_{\ell c}, \tag{4.9}$$

where ρ_ℓ and $V_{\ell c}$ denote the liquid mass density and the local liquid volume, which can be calculated by

$$V_{\ell c} = S V_{void}, \tag{4.10}$$

where S is the saturation. By combining Eqs. 4.7 and 4.10, ρ_ℓ can be expressed by:

$$\rho_{\ell c} = \epsilon \rho_\ell S. \tag{4.11}$$

The liquid velocity u can be calculated from Darcy's law (neglecting gravity) as:

$$u = -\frac{\frac{k_{eff}}{\mu}\frac{\partial p_\ell}{\partial z}}{\epsilon S}. \tag{4.12}$$

By inserting Eqs. 4.11 and 4.12 into Eq. 4.6, one can obtain:

$$\frac{\partial \epsilon \rho_\ell S}{\partial t} = -\frac{\partial}{\partial z}(-\rho_\ell \frac{k_{eff}}{\mu}\frac{\partial p_\ell}{\partial z}) - \Gamma. \tag{4.13}$$

The component mass balance in local formulation for the vapor phase reads:

$$\frac{\partial \rho_{vc}}{\partial t} = -\frac{\partial}{\partial z}(\rho_{vc} u + j_{vc}) + \Gamma, \tag{4.14}$$

where ρ_{vc} denotes the vapor mass density and j_{vc} the vapor diffusion flux. As for the vapor component, evaporation is a source term. The convection and diffusion terms (Stefan flow) can be calculated by

$$\rho_{vc} u + j_{vc} = -\frac{D_{v,eff}\widetilde{M}_v}{\widetilde{R}T}\frac{p_g}{p_g - p_v}\frac{\partial p_v}{\partial z}. \tag{4.15}$$

The vapor mass density and volume can respectively be calculated by

$$\rho_{vc} = \frac{m_{vc}}{V} = \frac{\rho_v V_{vc}}{V}, \tag{4.16}$$

and

$$V_{vc} = V_{void} - V_{\ell c}. \tag{4.17}$$

Combining Eqs. 4.8, 4.16 and 4.17 results in:

$$\rho_{vc} = \epsilon \rho_v (1 - S). \tag{4.18}$$

Inserting Eqs. 4.15 and 4.18 into Eq. 4.14 gives:

$$\frac{\partial \epsilon \rho_v (1-S)}{\partial t} = -\frac{\partial}{\partial z}(-\frac{D_{v,eff}\widetilde{M_v}}{\widetilde{R}T}\frac{p_g}{p_g - p_v}\frac{\partial p_v}{\partial z}) + \Gamma. \tag{4.19}$$

By expressing $k_{eff} = k_{abs}k_{r\ell}$ and $D_{v,eff} = D_{abs}D_{rv}$, the two-equation continuum model can be written as:

$$\frac{\partial \epsilon \rho_\ell S}{\partial t} = -\frac{\partial}{\partial z}(-\rho_\ell \frac{k_{abs}k_{r\ell}}{\mu}\frac{\partial p_\ell}{\partial z}) - \Gamma. \tag{4.20}$$

$$\frac{\partial \epsilon \rho_v (1-S)}{\partial t} = -\frac{\partial}{\partial z}(-\frac{D_{abs}D_{rv}\widetilde{M_v}}{\widetilde{R}T}\frac{p_g}{p_g - p_v}\frac{\partial p_v}{\partial z}) + \Gamma. \tag{4.21}$$

Equations 4.20 and 4.21 describe the one-dimensional distribution of the liquid and vapor phases in the REV during the drying process. The effective parameters k_{eff} and $D_{v,eff}$ control the average behavior of the REV and their values should not essentially change with increasing REV size provided that the chosen size is small enough compared to the volume of the system, but large enough compared to the pore sizes. This is referred to as length-scale separation criterion [9]. The two-equation continuum model refers to these macroscopic equations.

4.2.2 One-equation Continuum Model for Drying

This section concentrates on the derivation of the one-equation continuum model. First the total moisture (i.e. liquid and vapor) balance is written as:

$$\frac{\partial \epsilon \rho_v (1-S)}{\partial t} + \frac{\partial \epsilon \rho_\ell S}{\partial t} = -\frac{\partial}{\partial z}(-\rho_\ell \frac{k_{abs}k_{r\ell}}{\mu}\frac{\partial p_\ell}{\partial z} - \frac{D_{abs}D_{rv}\widetilde{M_v}}{\widetilde{R}T}\frac{p_g}{p_g - p_v}\frac{\partial p_v}{\partial z}). \tag{4.22}$$

Under the assumption of quasi-steady state condition for vapor transfer in the gas phase, the first term on the left hand side of Eq. 4.22 turns to zero:

$$\epsilon \rho_\ell \frac{\partial S}{\partial t} = -\frac{\partial}{\partial z}(-\rho_\ell \frac{k_{abs}k_{r\ell}}{\mu}\frac{\partial p_\ell}{\partial z} - \frac{D_{abs}D_{rv}\widetilde{M_v}}{\widetilde{R}T}\frac{p_g}{p_g - p_v}\frac{\partial p_v}{\partial z}). \tag{4.23}$$

In order to be able to solve Eq. 4.23, two assumptions are made: A local capillary equilibrium in an REV yields:

$$p_\ell = p_g - p_c. \tag{4.24}$$

At constant temperature the saturated vapor pressure p_v^* is constant. Thus, the condition on the relative humidity φ becomes a condition on p_v (and in turn on S):

$$\varphi(S) = \frac{p_v}{p_v^*} = \frac{1}{p_v^*} p_v(S). \tag{4.25}$$

Commonly p_v is related to the total saturation, i.e. both free capillary water and bound water, by a predefined expression of sorption isotherm. However, a new interpretation of φ is introduced in this work. Incorporating these two assumptions into Eq. 4.23, the one-equation continuum model can be obtained that takes the form of:

$$\epsilon \frac{\partial S}{\partial t} = \frac{\partial}{\partial z}\left(\frac{k_{abs} k_{r\ell}}{\mu}\left(-\frac{\partial p_c}{\partial S}\frac{\partial S}{\partial z}\right) + \frac{D_{abs} D_{rv} \widetilde{M}_v}{\rho_\ell \widetilde{R} T} \frac{p_v^* p_g}{p_g - \varphi p_v^*} \frac{\partial \varphi}{\partial S}\frac{\partial S}{\partial z}\right). \tag{4.26}$$

This equation is expressed only in S and thus is referred to as one-equation continuum model. To simplify the form of this equation, the following term is denoted by $D(S)$:

$$D(S) = \frac{k_{abs} k_{r\ell}}{\mu}\left(-\frac{\partial p_c}{\partial S}\right) + \frac{D_{abs} D_{rv} \widetilde{M}_v}{\rho_\ell \widetilde{R} T} \frac{p_v^* p_g}{p_g - \varphi p_v^*} \frac{\partial \varphi}{\partial S}. \tag{4.27}$$

As a result, the one-equation CM can be expressed by:

$$\epsilon \frac{\partial S}{\partial t} = \frac{\partial}{\partial z}\left(D(S)\frac{\partial S}{\partial z}\right). \tag{4.28}$$

In this equation, $D(S)$ is regarded as the total moisture transport coefficient with contributions of both the liquid and vapor phases:

$$D(S) = D_\ell(S) + D_v(S). \tag{4.29}$$

By comparing Eqs. 4.23 and 4.27, one can calculate the one-dimensional total liquid flux by:

$$j_\ell = -\rho_\ell D_\ell(S)\frac{\partial S}{\partial z}, \tag{4.30}$$

and likewise the total vapor flux by:

$$j_v = -\rho_\ell D_v(S)\frac{\partial S}{\partial z}. \tag{4.31}$$

The initial and boundary conditions for the porous body are set up as follows: The porous medium is initially saturated with pure liquid water. No-flux boundary condition is assumed at the medium bottom ($z = 0$). At the open

surface ($z = H$), the drying rate (i.e. vapor flux) is prescribed for convective drying by boundary layer theory (without Stefan correction):

$$\dot{m}_v = \frac{\widetilde{M}_v \delta p_v^*}{\widetilde{R}T}\left(\frac{\varphi_s(S_s) - \varphi_\infty}{\varepsilon}\right). \tag{4.32}$$

Equation 4.28 is highly nonlinear because of the dependence of D on S. Therefore this equation is solved numerically by means of a finite difference approximation. The spatial domain is discretized into several uniform grids and an explicit time stepping scheme with variable time step is used for time discretization. In the following sections, three methods are introduced to determine the macroscopic parameters of the one-equation CM for drying.

4.2.3 Forward Methods

Two methods are presented that are used to determine the macroscopic transport and equilibrium parameters from simulations at the pore level. First method is based on post-treatment of phase distributions obtained from (dynamic) pore network simulations of drying for multiple realizations of the pore space geometry. By applying this method, the internal and surface relationships between vapor pressure and saturation as well as the moisture transport coefficient D over the full range of saturation are determined. Second method requires phase distributions at distinct times that are obtained from network simulations where the pore invasion is controlled by capillarity only; this is referred to as capillary-controlled invasion pore network simulations. Thus, intrinsic permeability, wetting fluid relative permeability, and capillary pressure are computed. Contrary to the first method, this method allows to determine the variation of D_ℓ only for saturation greater than the irreducible saturation $S \geq S_{irr}$. An attribute common to both methods is that they are somehow offline, i.e. the coefficients are computed by the pore network simulations prior to the continuum simulation is run.

The reason why two methods are used is simply to check whether both methods lead to comparable results for the moisture transport coefficient. This gives more confidence in the results obtained from the drying simulations. Also, since the network size is different for each model, this gives an indication that the averaging volume choice in the drying simulations is not perhaps such an issue as it may appear at first glance.

Method I: Dynamic Pore Network Drying Simulations

This method is motivated by experimental methods. It operates for a given numerical porous medium as follows: Input quantities are the evolution of the

liquid saturation as well as the vapor pressure (p_v) and the liquid pressure (p_ℓ) at nodes within averaging volumes over drying time. An averaging volume (or REV) is identified by slicing virtually a three-dimensional pore network into horizontal volumes with constant thickness (Δz) and cross section (A) at specific times during drying (see Fig. 4.27). Thus the volume-weighted averaging method is used here. Outputs are the local macroscopic variables, i.e. the average vapor partial pressure ($\bar{p}_v$), the average liquid flux (j_ℓ), and the average vapor flux (j_v).

Due to high computational demand, fifteen Monte-Carlo simulations have been run and the results are presented as averaged profiles. All simulations start with saturated networks at room temperature (20°C) and atmospheric pressure (1 bar); the physical properties are indicated in Table 4.2. The value of liquid viscosity may look quite strange. This however is utterly a trick for obtaining a viscous dissipation characteristic length shorter than the network height. As a result, the maximum size of the two-phase zone in the simulated drying process is smaller than the network height. When the viscous effects are less, the two-phase spans over the full height of the pore network. The computation is not affected since the same viscosity is used in both the pore network simulations and the continuum model. Liquid evaporation occurs only at the top of the network; the remaining faces are impervious to fluids.

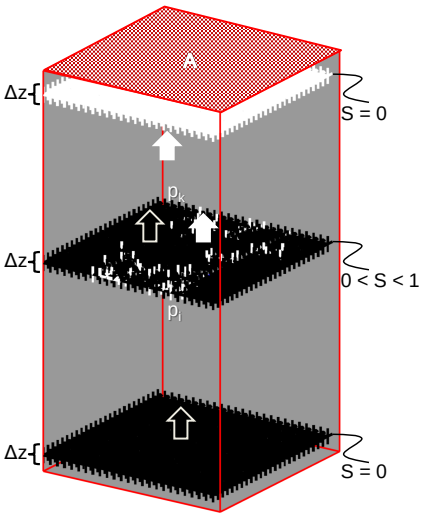

Figure 4.27: Slices (or REVs) with a constant thickness of Δz are virtually cut out from a pore network with cross section A. Liquid or vapor flux j within a slice with saturation S is driven by gradient in the corresponding pressure, i.e. p_i and p_k. Black and white lines, respectively, stands for liquid and empty pores.

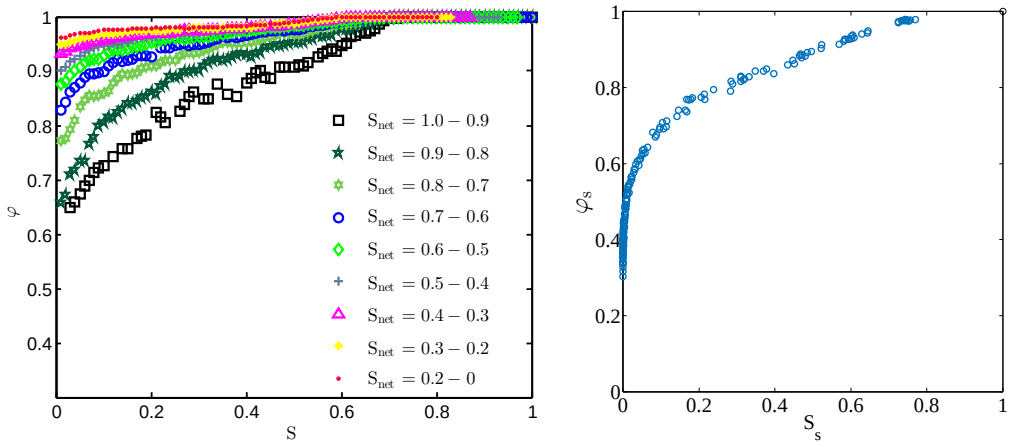

(a) (b)

Figure 4.28: Variation of φ with local saturation S inside the network (a) and at the network surface (b). The profiles are averages of 15 pore network realizations, which are dried under identical drying conditions [T].

Under isothermal condition p_v^* is constant. The functions for internal relative humidity $\varphi(S)$ and surface relative humidity $\varphi_s(S_s)$ are thus built based upon the averaged data $\bar{p}_v(S)$ and $\bar{p}_{v,s}(S_s)$, respectively. These functions are shown in Fig. 4.28. When modeling drying of a non-hygroscopic porous medium, i.e. a porous medium in which adsorption phenomena are absent, within the frame of continuum approach, it is postulated that the equilibrium vapor pressure in an REV with non-zero water content is the saturated vapor pressure; this implies a relative humidity of unity. However, the average partial vapor pressure profiles obtained from the pore network simulations deviate significantly from the saturated vapor pressure, and also depend on network saturation S_{net}. This deviation is interpreted as the signature of a non-local equilibrium (NLE) effect, which is observed inside the network as well as near the open surface of the network. This observation is despite of the fact that the vapor pressure above the meniscus surface in the pore network simulations is assumed to be at the saturated vapor pressure. Based on these profiles, vapor diffusion can be described not only in dry region, but also in partially saturated network region.

It may worth noting that the NLE effect has nothing to do with the sorption isotherm which is relevant for hygroscopic porous materials, not for capillary porous materials as considered in this study. In addition, one could argue that the NLE relation is trivial and can be described by accounting for the capillary condensation effect (see Chapter 2). However, this effect, which

property	value
Bulk vapor pressure, $p_{v,\infty}$ (Pa)	0.0
Saturated vapor pressure, p_v^* (Pa)	2339
Kinematic viscosity of water, ν_w (m^2/s)	$28 \cdot 10^{-3}$
Molar vapor mass, $\widetilde{M}_v$ (kg/kmol)	18.02
Surface tension between water and air, σ (N/m)	0.07274
Universal gas constant, $\widetilde{R}$ (J/kmolK)	8314.5
Vapor diffusivity, δ (m^2/s)	$2.5685 \cdot 10^{-5}$
Network size (node)	$25 \times 25 \times 51$
Boundary layer size (node)	$25 \times 25 \times 10$
Mean throat radius, $\bar{r}$ (μm)	250
Standard deviation of throat radius, σ_0 (μm)	25
Throat length, L (mm)	1
Network porosity	0.594

Table 4.2: Physical properties of fluids at $T = 293.15$ K and $p_g = 1$ bar as well as structural characteristics of the pore network.

can be described by the Kelvin equation, is neglected in the pore network drying model considered in this study.

Based on the pore network simulation results, the local moisture transport coefficients for the liquid and vapor phases are also computed respectively by:

$$D_\ell(S) = -\frac{\frac{\sum_{k=1}^{n} J_{\ell,k}}{A}}{\rho_\ell \frac{\partial S}{\partial z}} = -\frac{j_\ell}{\rho_\ell \frac{\partial S}{\partial z}}, \tag{4.33}$$

$$D_v(S) = -\frac{\frac{\sum_{k=1}^{n} J_{v,k}}{A}}{\rho_\ell \frac{\partial S}{\partial z}} = -\frac{j_v}{\rho_\ell \frac{\partial S}{\partial z}}. \tag{4.34}$$

Here, the liquid and vapor mass flow rates, i.e. J_ℓ and J_v, over all vertical throats filled with liquid or vapor ($k = 1...n$) are computed by the Hagen-Posieuille equation and the linear gas diffusion equation, respectively. The linear superposition of these coefficients gives the resultant moisture transport coefficient for both phases $D(S)$. Figure 4.29 illustrates these three transport functions that control the transport phenomena in the model porous medium during drying. Three distinct points are identified in the $D - S$ curve: at $S \approx 1$ the moisture transport is driven fully in the liquid phase, at $S \approx 0$ the transport is entirely in the vapor phase, and at S_{min} the moisture transport occurs in both phases with comparable contributions.

As can be seen, the values of D_ℓ decrease with decreasing the local saturation. This is because the hydraulic conductivity of the liquid phase is alleviated in the course of the drying process. During this period, the mean local vapor pressure remains nearly at the saturated vapor pressure in the whole network, and thus no vapor pressure gradient can be established in the gas phase. As drying proceeds, the partial vapor pressure in gas pores departs from the saturated vapor pressure. Consequently, the driving force for the vapor transport increases, and thus D_v increases (see Eq. 4.34). These numerical results are qualitatively in line with experimental determinations on real porous bodies available in the literature [80]. However, one noticeable difference in the $D - S$ curves obtained in this study and those reported in previous works is the clear dependency of D on the network saturation for local saturation $S < 0.68$. This non-unique characteristics of the function $D(S)$ is attributed to the presence of isolated liquid menisci that become increasingly more numerous for similar local saturation during drying. The fact that the $D(S)$ function is not unique has been observed in the experimental data with a certain level of uncertainty, as can be seen in Fig. 4.31b.

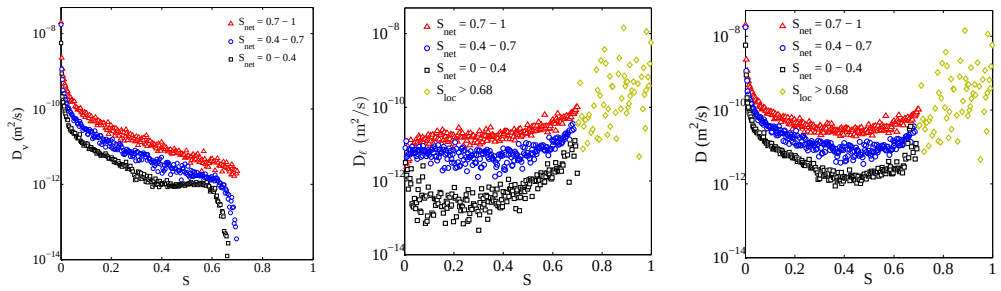

(a) (b) (c)

Figure 4.29: Variation of vapor (a), liquid (b) and total (c) transport coefficients with local saturation during the drying process [T].

Method II: Capillary-Controlled Invasion Pore Network Simulations

This method is adopted from the procedure commonly used for computation of single-phase and two-phase flow parameters from quasi-static pore network simulations [45]. In this method, a pore network of size $25 \times 25 \times 25$ is chosen as an REV. In order to reduce the level of uncertainty in the parameters, the capillary-driven pore network simulations have been performed for 45 different realizations of the pore space. The resulting value of the intrinsic permeability, which is considered as a static property, is $1.6 \cdot 10^{-9} \pm 7 \cdot 10^{-13}$

m^2. Figure 4.30 shows the evolution of the capillary pressure p_c and the relative permeability $k_{r\ell}$, which are considered as dynamic properties, during the invasion process.

Under a fully saturated condition ($S = 1$) the liquid phase forms one cluster spanning the entire network. This leads to a maximum value of the relative permeability ($k_{r\ell} = 1$). On the other hand, the capillary pressure is minimum at the beginning of the invasion process. When once bigger pores are invaded by the gas phase, the liquid looses its hydraulic conductivity. The liquid permeability thus continues to decrease, whereas the capillary pressure increases as the local saturation decreases. The gas continues invading liquid pores until the irreducible saturation is reached. The unconventional large value of the irreducible saturation ($S_{irr} \approx 0.68$) is due to low coordination number of the pore network (each pore is connected to six neighbor pores) compared to the average coordination number in real systems. Also, the fact that the pores are volumeless and thus the entire pore space volume is in the throats leads to a greater irreducible saturation.

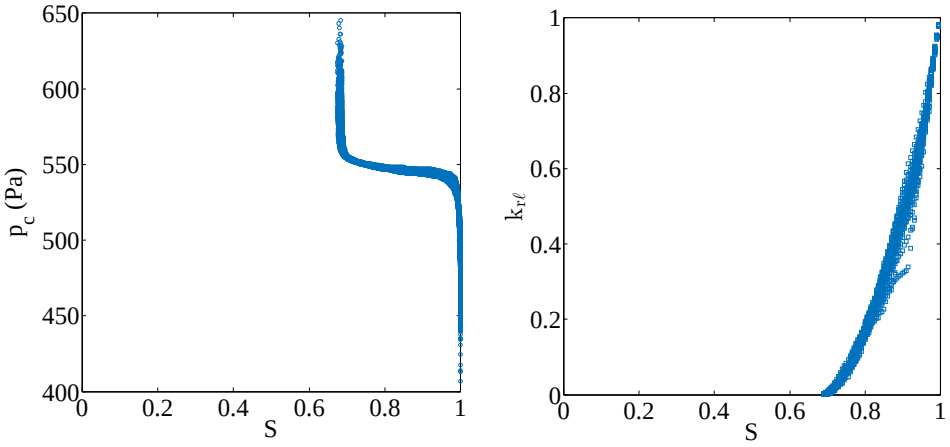

Figure 4.30: The values of the relative permeability (a) and the capillary pressure (b) computed by the quasi-static pore network simulations [T].

4.2.4 Inverse Method

If transport properties of a porous medium during drying are known a priori, then a direct (or forward) method can be used to determine the variation of state variables during the drying process. On the other hand, if these properties are unknown, the inverse method can be used to deduce them from a set of available experimental or simulation data. Hence the inverse method

can conceptually be formulated as "simulation results or experimental data → transport properties".

An inverse method for the problem of porous media drying operates as follows: First model equations as well as initial and boundary conditions are defined. Values are assumed for the model parameters and then the governing equations are solved. Desired values of the parameters are thus estimated by minimizing systematically the differences between measured and simulated variables of interest, e.g., the medium moisture content.

As an example, the diffusion coefficient has been identified from the inverse analysis of the transient moisture profiles measured by nuclear magnetic resonance (NMR) during drying of a sand-lime brick sample [80] – see Fig. 4.31. For this purpose, a non-linear diffusion equation is employed to describe the moisture transport for the one-dimensional isothermal drying:

$$\frac{\partial X}{\partial t} = \frac{\partial}{\partial z}(D(X)\frac{\partial X}{\partial z}), \tag{4.35}$$

where X denotes the moisture content which varies along the sample height z. To infer the $D(X)$ from the experimental moisture profiles (Fig. 4.31), Eq. 4.35 is integrated with respect to z, yielding:

$$D(X) = \frac{\int_0^{z'}(\frac{\partial X}{\partial t})}{(\frac{\partial X}{\partial z})_{z'}}. \tag{4.36}$$

In Eq. 4.36, the partial derivative of X with respect to z is zero at the sample bottom, i.e. $z = 0$. The moisture diffusivity is numerically calculated at each position z', corresponding to a moisture content X. This procedure is repeated for all moisture profiles and the moisture diffusivity is thus determined as a function of moisture content, but only up to the residual moisture content (Fig. 4.31). The moisture diffusivity over the full range of the moisture content has however been determined by combining the moisture diffusivities obtained from the moisture profiles during the drying and absorption experiments, with those obtained from the receding front model. The results of such an approach can be found in [80].

The moisture profiles obtained from the NMR experiments and the slice-averaged saturation profiles computed from the pore network simulations delineate different behavior (see Figs. 4.31a and 4.32a). The measured moisture profiles remain essentially uniform in space for a significant period of the drying process. This may be attributed to the existence of the secondary capillary structures. However, the absence of these structures in the pore network model has led to a sharp drop of saturation in the regions near the network surface. Despite these discrepancies, the moisture diffusivity-

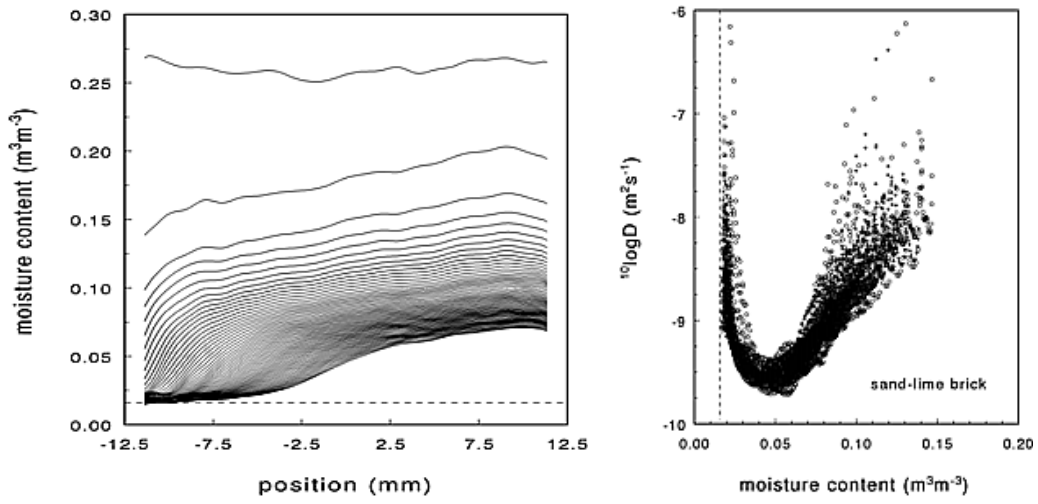

(a) (b)

Figure 4.31: (a) Moisture profiles measured during drying for sand-lime brick and (b) corresponding moisture diffusivity determined from the inverse analysis. The moisture profiles are measured for a period of 120 hours and the time between subsequent profiles is 2 hours. The positions 12.5 and -12.5 correspond to the top and bottom of the sample, respectively. The dashed line indicates the residual moisture content observed at 45% relative humidity of air in the drying experiment [80].

saturation curve determined from the inverse analysis reflects a trend similar to that obtained from the forward pore network drying simulations [T], i.e. two maxima and a minimum. The D-S curves determined from these two methods show a somewhat similar scattering with clouds of values at each level of saturation. The scatting could be due to a non-unique correspondence between the saturation and the local liquid distribution during drying. However, further research is required to clarify this issue.

It should be stated that the use of the inverse method is computationally expensive because both the dynamic pore network simulations and many solutions of the diffusion equations for different values of the coefficient D are required.

4.2.5 Continuum Modeling of Wetting

The Lucas-Washburn law and the Richards equation are two continuum models that are widely adopted for wetting porous materials and therefore are revisited in this section. In hydrology or other disciplines these two models

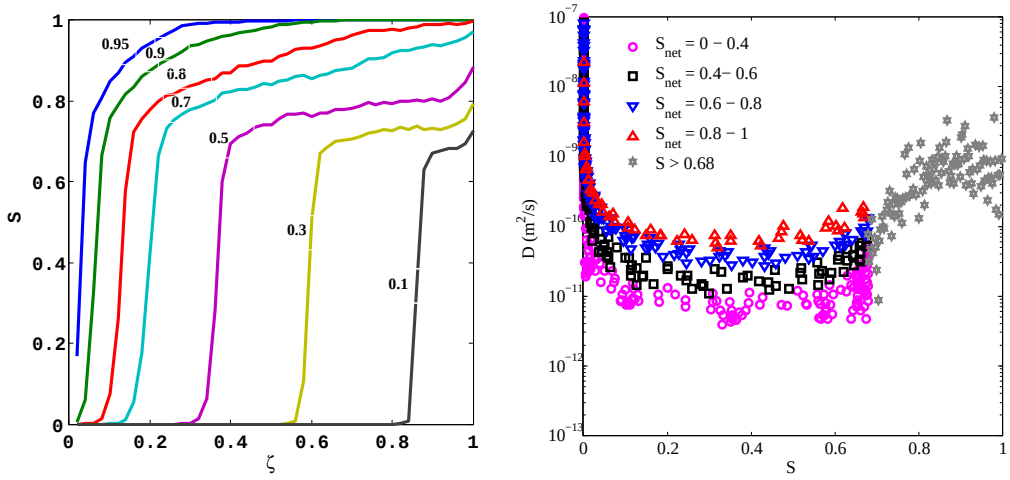

(a) (b)

Figure 4.32: (a) Saturation profiles obtained from pore network simulations and (b) corresponding moisture diffusivity determined from the inverse analysis. The saturation profiles are averages over 13 realizations of a network with size of 25×25×51. $\zeta = 1$ corresponds to the bottom and $\zeta = 0$ to the top of the network [128].

are used in the context of unsaturated flow in porous media. The Lucas-Washburn law is derived from a momentum balance of a liquid within a (rigid) porous medium. For this purpose a simple situation is adopted, which assumes that the gravitational and the inertial forces are negligible. Therefore the distance traveling in the very initial period is ignored, and the Darcy region – for a single capillary, Poiseuille region – covers practically the entire flow. Also, a piston-like displacement of the wetting front, an equilibrium contact angle, a constant mean pore radius, and negligible air entrapment are assumed. Based on these assumptions, an analytical solution of the momentum balance equation reads:

$$S(t) = \frac{2}{H}\sqrt{\frac{\sigma cos\theta k_{abs}}{r\epsilon\mu}}\sqrt{t}. \tag{4.37}$$

This solution indicates that the medium saturation S and thus the front height, $h(t) = S(t)H$, varies with respect to square root of time. The fairly simple – and thus nice to handle – Lucas-Washburn solution is probably the most used equation when it comes to the problem of a wetting liquid intruding in a porous matrix. An important lesson that can be learned from this equation is that when a dry homogeneous porous medium is brought

in contact with a bath of wetting liquid, small pores favor high rising and big pores favor high initial front speeds. Applicabilities and extensions of the Lucas-Washburn equation to other flow regimes have been reported in [34, 129].

In the analysis of the Lucas-Washburn solution the saturation is either equal to unity or null. However, it has been observed experimentally that the transition between the liquid saturated part and the air saturated part of the medium is more gradual. Richards considered this situation and derived his equation by combining the mass conservation law (without the external source or sink term) for the liquid phase and Darcy's law as a closure. Putting in mathematical language, the Richards equation in saturation-based form reads:

$$\epsilon \frac{\partial S}{\partial t} = \frac{\partial}{\partial z}(D(S)\frac{\partial S}{\partial z}), \tag{4.38}$$

$$D(S) = -\frac{k_{abs} k_{r\ell}(S)}{\mu} \frac{\partial p_c(S)}{\partial S}. \tag{4.39}$$

The moisture transport coefficient $D(S)$ is determined from the capillary-controlled invasion pore network simulations, which are conducted for an REV with a size of $15 \times 15 \times 15$. At each invasion step, the smallest throat containing a meniscus is filled with liquid and the corresponding saturation, capillary pressure p_c and relative permeability $k_{r\ell}$ are calculated. This procedure continues until the REV is fully saturated with the liquid. At this stage ($S = 1$), the relative permeability is equal to unity (single-phase flow) and the absolute permeability k_{abs} is calculated. Having all the required parameters k_{abs}, $k_{r\ell}(S)$ and $p_c(S)$, the moisture transport coefficient $D(S)$ can be determined using Eq. 4.39.

These pore network simulations are repeated for 15 times, where each time a new set of throat radii is sampled from a normal distribution with a mean of 250 μm and a standard deviation of 20%. These simulations result in an absolute permeability value of $1.8349 \cdot 10^{-9}$ m^2. Figure 4.33 shows the capillary pressure curve and the relative permeability curve. The relative permeability value starts when the liquid breaks through the network. At this moment only the spanning liquid clusters, i.e. those which are connected to both the top and bottom of the network, contribute to the liquid transport. In these simulations the breakthrough occurs at saturation $S = 0.0648$.

The superposition of the permeabilities' values provides the function $D(S)$, see Figure 4.34. As can be seen, D is not defined near $S = 0$. This is due to the fact that one of its constituents, i.e. $k_{r\ell}$, can be calculated only after the breakthrough saturation. This $D(S)$ function is fed into the

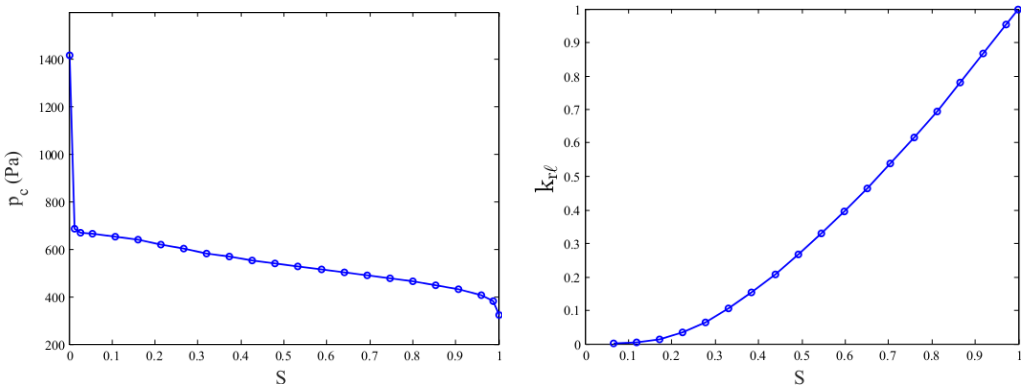

(a) (b)

Figure 4.33: Capillary pressure (a) and relative liquid permeability (b) as a function of the liquid saturation during the wetting process [U].

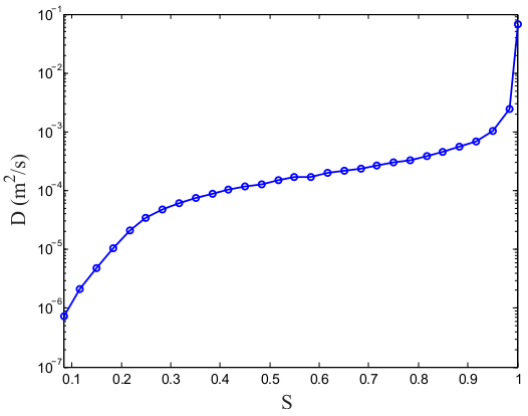

Figure 4.34: Moisture transport coefficient as a function of the local saturation [U].

Richards equation and the resulting numerical solution is quantitatively assessed versus dynamic pore network simulation results, later in this chapter. Another route to determine the moisture transport function is the classical inverse method, in which the kinetic data obtained from the dynamic pore network simulations is used [U].

4.3 Reconciliation of Discrete and Continuum Models

4.3.1 Drying Models

The one-equation continuum model for drying is quantitatively assessed based on the numerical pore network simulations. The continuum model parameters, $D(S)$, $\varphi(S)$, $\varphi_s(S_s)$, are calculated by the pore network drying model, according to the method introduced in Sec. 4.2.

Figure 4.35 shows saturation profiles obtained from both the pore network and continuum model simulations. By comparing saturation profiles of these two models, it can be seen that the saturation profiles predicted by both models are in agreement. It however is clear that after network saturation reaches 0.4 the continuum model fails slightly to predict the dry region correctly. This deficiency is even more pronounced at lower saturations. A minor discrepancy can also be seen at lower part of the network, where saturation values are overestimated by the continuum model. The discrepancies seen between the continuum model and the pore network simulation results are mainly due to the fact that in Eq. 4.28 only saturation is introduced as a process variable. In drying of porous media, vapor pressure is also a variable which changes spatiotemporally. In fact the moisture diffusion model considers a relationship between vapor pressure and saturation inside the network, similar to pseudo-desorption isotherm at the surface, and treats the drying process as a one-variable process. This relationship is actually hidden in the moisture transport coefficient. This assumption may lead to smoother distribution of water along the network, since the water conductivity is better established through a solely saturation-dependent moisture diffusion coefficient. One solution to this would be to develop a two-variable diffusion model in which saturation and vapor pressure are considered as independent variables.

4.3.2 Wetting Models

The Richards equation is solved numerically with $D(S)$ estimated from the capillary-controlled invasion pore network simulations presented in Sec. 3.3. The solution of the Richards equation yields the liquid saturation at different heights of the network during wetting, i.e. $S(t, z)$, until the network is fully wet. The total saturation S_{net} at each time is calculated from the local saturation levels. On the other hand, dynamic pore network simulations are conducted for 15 realizations of the pore space. In all realizations the network size is $15 \times 15 \times 60$, and the throat radii are sampled from a normal

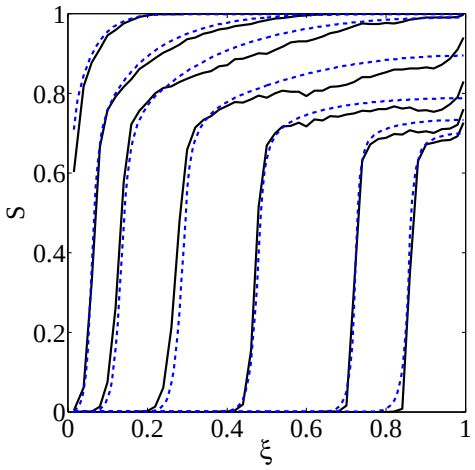

Figure 4.35: Spatio-temporal variation of local saturation S during drying of a model porous medium with normalized height ζ. The continuum model solution and the pore network simulations are shown in blue dashed lines and black solid lines, respectively. The saturation profiles of pore network are averaged among 15 realizations [T].

distribution with a mean of 250 μm and a standard deviation of 20%. For comparison, the results of both models are shown together in Fig. 4.36.

As can be seen, the solution of the Richards equation gives an estimation of the wetting rate and of the total wetting time, with a slight deviation from the pore network prediction. This deviation is almost negligible at the onset of the process, yet becomes more pronounced at later times. It can also be seen that the Lucas-Washburn law predicts a slightly faster wetting compared to the pore network solution. In the Lucas-Washburn law the front is assumed to be sharp. This assumption essentially suggests that the viscous forces dominate the capillary forces, otherwise the front would be fractal. An occurrence of this situation implies a higher liquid flow rate, and thus a larger average liquid velocity.

The saturation profiles obtained from the pore network simulation results and the solution of the Richards equation are shown in Fig. 4.37. The Richards equation predicts similar results as the pore network model at early stages of the wetting process. However, as time proceeds, a discrepancy appears and the Richards equation predicts a slightly broader wetting front than the pore network model.

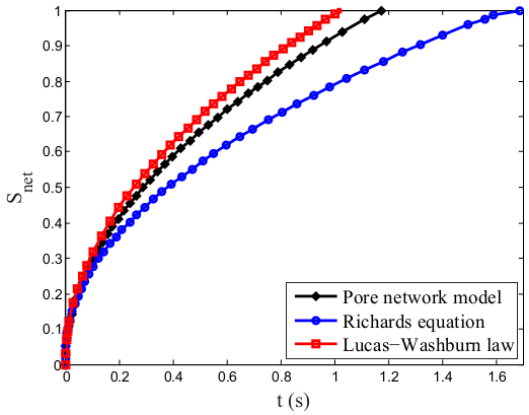

Figure 4.36: Wetting kinetics obtained from the pore network simulations and the continuum model solutions [U].

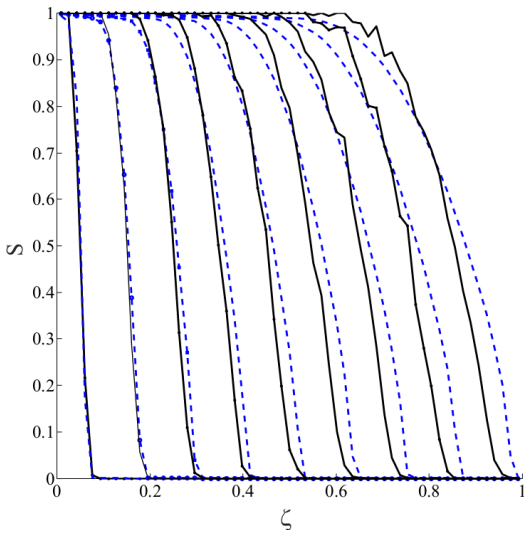

Figure 4.37: Saturation profiles obtained from the solution of the Richards equation (dashed line) and from the pore network simulation results (solid line). From left to right, S_{net} = 0.14, 0.24, 0.34, 0.44, 0.54, 0.64, 0.74, 0.84, 0.94. ζ denotes the normalized position in the height direction [U].

4.3.3 Liquid Velocity Field

Liquid velocity field arising from the drying process in a capillary porous medium is determined within the continuum and discrete modeling frameworks. In both approaches, a prerequisite for determining the velocity field is the liquid distribution profiles, i.e., the local variation of the liquid saturation during drying. The distribution of the liquid saturation along the

medium height during drying depends on the interplay between capillary, viscous, and gravitational forces. Depending on dominant forces, various drying regimes can be developed [130]. When the capillary forces are instantaneously most favorable during the drying process, the liquid distribution in the porous medium remains almost independent of the vertical coordinate. Such a limiting case is referred to as the capillary-dominated regime and it occurs during most of the CRP/FRP. The velocity profile from the continuum standpoint is determined as follows: First a total mass balance is written that relates the variation of the average liquid saturation to the total drying flux at the medium surface. Then a local mass balance is written for the variation of local saturation inside the medium. Combining these two balance equations and invoking a spatially uniform saturation profile clearly shows that the liquid velocity varies linearly along the medium height. It is zero at the medium bottom and increases monotonically towards the evaporative surface. The resulting velocity function represents the interstitial velocity and not the filtration (or Darcy) velocity. At a give location inside the medium, the filtration velocity is time independent, whereas the interstitial velocity increases with respect to time. This argument holds as long as the drying rate remains almost constant [131].

On the other hand, the velocity field in the liquid phase is computed from discrete pore network simulations with physical properties given in Table 4.2. Since the main goal is to reconcile the discrete description of the velocity field with the continuous counterpart, the pore network simulations are also conducted under the capillary-dominated regime. In this regime, the liquid velocity field is determined from the liquid distribution, which is a result of a succession of quasi-static capillary equilibria. In each equilibrium state, a single liquid pore is fully invaded by the gas phase. This is typically referred to as the capillary action or capillary pumping (see Sec. 2.3). It can also be referred to as a global Haines jump. The difference between the Haines jump and the capillary pumping is that the former event occurs almost in zero time. In other words, the Haines jump could be explained as a capillary flow with an infinite flow velocity, during which dynamic effects resulted from viscous and inertial forces are present [132, 133]. The role of these events in the successive equilibrium distributions is not accounted for in the pore network model.

As mentioned before, during drying liquid clusters form as a result of the pore invasions and the diffusive transport of the vapor. In the limit of capillary-dominated regime, there is one pore with an unstable meniscus in each cluster. During drying of each cluster, the liquid is pumped from the unstable meniscus to stable menisci, originating thus the liquid velocity field. The method developed to compute the velocity field is reported in [V] and

in [128, 134].

The instantaneous three-dimensional velocity field is averaged over the horizontal or vertical slices during the CRP so as to determine the one-dimensional cumulative out-plane or in-plane velocity profile, respectively. As shown in Fig. 4.38, the cumulative out-plane velocity, which is perpendicular to the evaporative surface, is three to four orders of magnitude greater than the in-plane velocity. For the reconciliation, the out-plane (or vertical) filtration velocity is considered.

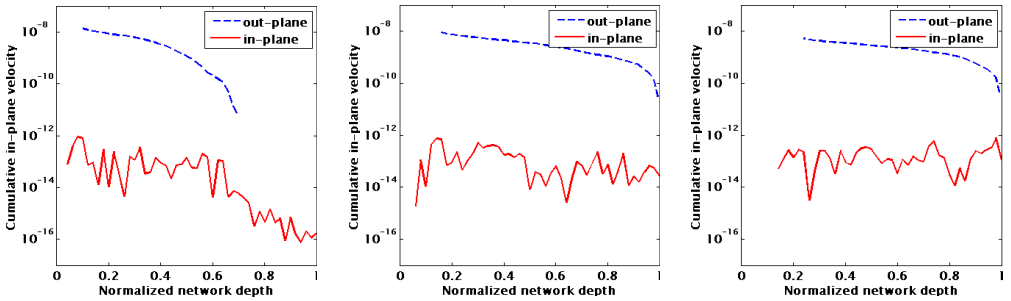

Figure 4.38: Comparison of cumulative in-plane and cumulative out-plane velocities at three different network saturations: (a) 90%, (b) 80%, and (c) 70%. On x-axis one and zero indicate bottom and top of the pore network, respectively [135].

The vertical filtration velocity profiles obtained from the numerical pore network simulations are shown in Fig. 4.39. These profiles are remarkably different from the one deduced from the continuous approach. The instantaneous vertical velocity profiles computed from the pore network simulations results in step functions in lieu of the linear one obtained from the continuum description. By averaging the single-invasion velocity profiles over a number of invasions, or in other words, over a time interval, the velocity profile of the continuum approach can be obtained. This study suggests that the classical macroscopic equations used to predict the drying behavior in the capillary regime could thoroughly be formulated combining space and time averages.

The determination of velocity field paves the way to better understand ions, colloidal or metal particles transport and their distribution in porous media during drying [136, 137, 138, 139]. For instance, the formation of salt efflorescence on cultural heritages [131, 140] or the functionalization of heterogeneous catalysts is related to the convective transport of dissolved species toward the evaporative surface by the velocity field [90].

The velocity field under other drying regimes, i.e., gravity-capillary regime

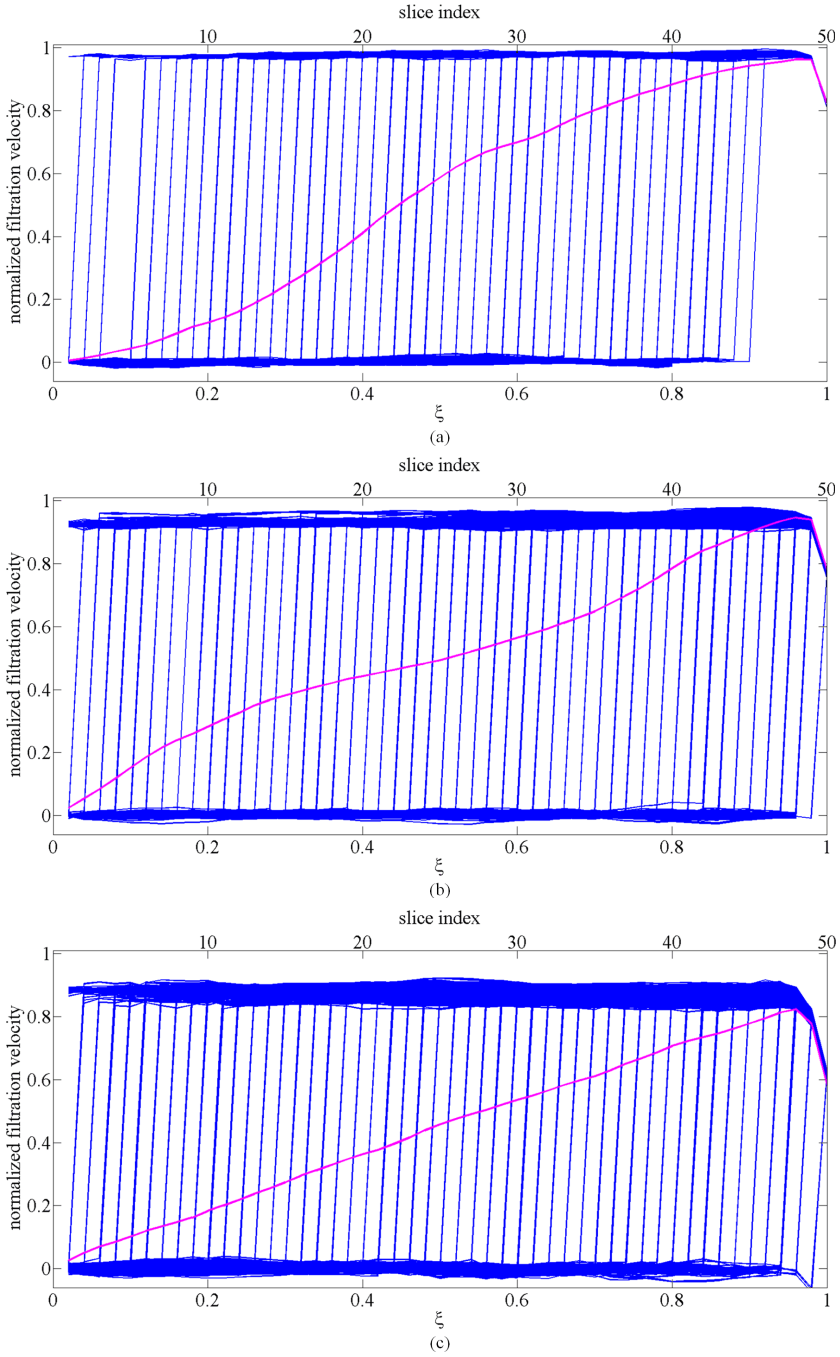

Figure 4.39: Normalized step filtration velocity profiles generated in the liquid phase by single invasions (blue lines) for network saturations (a) 90%, (b) 80%, and (c) 70%. The averaging of these single velocity profiles resulted in the quasi-linear average velocity profile (purple line) [V].

or viscous-capillary regime, are also performed. However, in the presence of viscosity or gravity, the averaged liquid velocity profiles are not linear. To calculate the velocity profiles from the continuum standpoint, a routine has to be used to post process saturation profiles which are obtained from discrete simulations [134].

4.3.4 External Mass Transfer

Drying of a porous medium involves both the internal transfers, i.e. inside the medium, and external transfers, i.e. in the gas-side boundary layer adjacent to the medium surface. If drying conditions are moderate, the drying process can be considered to be driven by mass transfer only. In the previous sections the internal mass transfer is extensively studied through both the continuum and discrete models, whereas a little attention is paid on the external mass transfer. However, the theoretical and experimental studies conducted under moderate conditions clearly indicate that both the internal and external mass transfers play a significant role in the existence and duration of the constant rate period (CRP) [141, 142]. The duration of the CRP is of paramount importance from an engineering viewpoint, because the total drying time can be reduced when a long CRP is maintained. The end of the CRP and transition toward the falling rate period (FRP) can be described from an internal transfer perspective. The CRP/FRP transition occurs when a net flow of liquid from the inside of the medium toward the smaller pores at the surface is not sufficient to compensate the total drying rate corresponding to the CRP. The compensation is in fact deteriorated due to the increasing viscous resistance in the liquid.

This transition can also be understood from the external mass-transfer perspective. What matters in this view is whether there are enough well-distributed liquid-filled pores at the medium surface and whether the adjacent gas-side boundary layer is sufficiently thick to maintain the drying rate at the high initial value. Viewing the CRP/FRP transition from the external mass-transfer perspective has been recognized at least since the sixties with the pioneering work of Suzuki and Maeda [143]. Suzuki and Maeda essentially explained that a partially wet surface could yield the same drying rate as a fully wet surface provided that the mass flux from the wet patches is greater than the average flux so that the absence of flux from the dry solid areas of the surface can be compensated. Later Schlünder considered this problem and proposed a simpler analytical model [144, 145]. Recently Schlünder's model has been analyzed and discussed by Or's group [146, 147, 148], as well as by us [U] and Prat's team [149].

In the analysis of Schlünder the porous medium surface is treated as a

smooth, flat, and porous surface with cylindrical pores of uniform sizes. In the entrance of these pores the liquid is mounted as uniform hemispheres. During drying vapor molecules are generated and then transported across a viscous layer by diffusion. These assumptions enabled Schlünder to derive a simple closure that provides an explicit relationship between the drying rate and the faction of the medium surface wetted by the liquid. According to this pore-scale relationship the thickness of the boundary layer is of major importance for the extent of the CRP. In the limit of a very thin boundary layer, lateral vapor transfer becomes negligible and the drying rate drops from the very beginning of the drying process. Another interesting piece of information that can be inferred from Schlünder's model is that the increase in the evaporation flux from the wetted area compensates the decrease in the mass-transfer rate from pores becoming dry at the surface, so that the total drying rate is not affected during the CRP [144, 145].

Very recently Prat [149] tested Schlünder's model for pores with different shapes or sizes. If the shape of individual pores of a model porous surface deviates too much from a circular pore, Schlünder's formula is not reliable enough for estimation of the corresponding drying rate. Also, when the fraction of the surface wetted area is low, the standard application of Schlünder's model leads to poor predictions of the drying rate. As regards to the surface with non-uniform pore sizes, Schlünder's formula results in less good estimates: the drying rate from bigger pores is significantly underestimated, whereas the drying rate from smaller pores is remarkably overestimated. Based on these rigorous analyses, a modified version of Schlünder's analytical model that accounts for pore size heterogeneity is proposed [149].

In fact both Schlünder and Prat disregarded the liquid flow capacity of a porous medium (capillary pumping) and thus the time-dependent behavior of wet patches at the medium surface. Linking the gas-side boundary phenomena with the internal mass transfer mechanisms provides the base for studying the dynamics of surface wetness and how it affects the drying rate under different boundary conditions.

To describe the lateral vapor transfer in the gas-side boundary layer, the dynamics of wet patches at the porous medium surface, the spatial variation in pore radius as well as the coupling with phenomena occurring inside the porous medium, a pore network model is certainly a good choice. In this frame, Irawan [95] clearly depicted that the lateral vapor transfer is important for the extent of the CRP. Very recently a more fundamental study in this direction has been conducted by our group.

Figure 4.40 is a top view of the network surface which shows phase distributions for various degrees of occupancy of the surface by liquid. Different colors, except white one, correspond to discrete liquid clusters (wet patches)

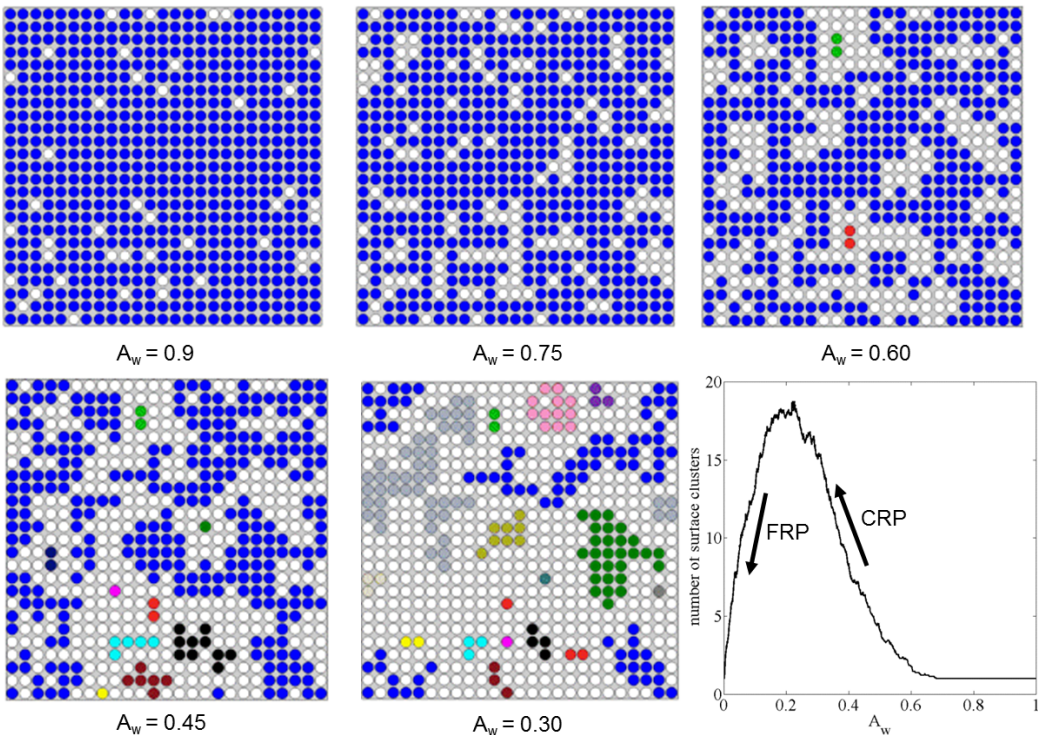

Figure 4.40: Evolution of liquid throats at the network surface during drying. Different colors correspond to liquid surface throats (wet patches) that belong to various liquid clusters, whereas gas throats (dry patches) are shown in white. Variation of the total number of surface clusters as a function of the surface pore occupancy degree A_w during the constant rate period (CRP) and falling rate period (FRP) is also shown [W].

at the surface – white color indicates gas pores (dry patches). At the onset of the drying process, only one big wet patch exists at the surface. As drying proceeds, wet patches with different sizes are formed. The evolution of the number of surface clusters during the CRP and FRP is also shown in Fig. 4.40. The number of surface clusters increases dramatically during the CRP. This number is then reaches a short plateau around the CRP/FRP transition prior to dropping sharply during the FRP. Figure 4.41 shows the relative contributions of the wet and dry patches to the total drying rate. As can be seen both wet and dry patches contribute to the mass transfer from the surface. This is notably different from Schlünder's classical model, which essentially hypothesizes that the contribution of dry pores to the mass transfer is negligible compared to the evaporation from the wetted area.

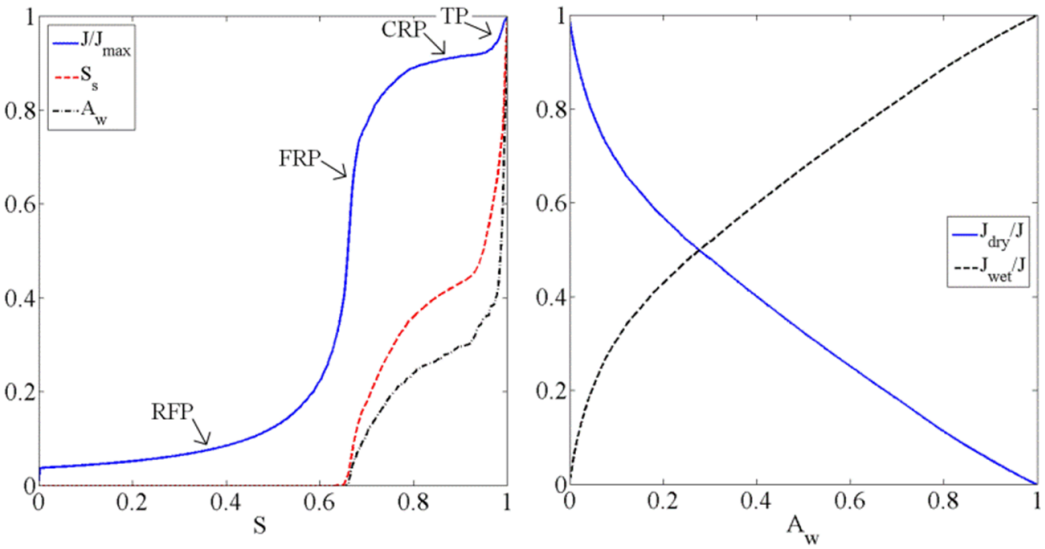

Figure 4.41: (left) Normalized evaporate rate J/J_{max}, fraction of surface throats occupied by liquid A_w, and network surface saturation S_s as a function of network saturation S. (right) Relative contributions of dry and wet patches at the network surface to the total mass transfer rate versus A_w. The results are averaged over 15 realizations [W].

In practice the mass transfer at the interface between a drying product and the surrounding bulk agent is generally achieved by introducing ad-hoc modeling such as a mass-transfer coefficient [150]. The dimensionless version of this coefficient, that is, the Sherwood number Sh, is usually expressed as a function of the Reynolds number Re and the Schmidt number Sc, i.e. $Sh = f(Re, Sc)$. These numbers are major tools that engineers use to confuse scientists. Anyway, such a function can be obtained by combining theoretical models (e.g., boundary layer theory or penetration theory) and correlations of experimental data [151]. In this framework, the mass-transfer coefficient depends on the relevant physical properties of the bulk agent, the geometry of the product, and the velocity of the bulk agent. Though this continuum approach is much simpler than, for example, the pore-scale Schlünder's model, it is not satisfactory from modeling/theoretical standpoints. This is because the temporal and spatial variations of the mass transfer coefficient, which result from the coupling between the external and internal mass transfer, are generally not known a priori. Therefore, this coefficient is frequently used as a fitting parameter to match experimental data. The fitting procedure seeks a function that relates this coefficient to the surface saturation.

The most versatile approach for coupling mass transfer at the interface between the medium surface and the external gas is to solve the Navier-Stokes equations for the external gas together with the vapor transport equation for both the external gas and medium itself. This infers that the continuity of vapor concentration (or, equivalently, the vapor partial pressure) and mass flux at the interface must be maintained. Such a coupling strategy is employed for the case when the porous medium is treated as a continuum [152, 153] or when it is regarded as a discrete pore network [154].

Chapter 5

Summary and Future Research Directions

5.1 Summary

Experimental and theoretical studies have been presented in this thesis with the primary goal to describe complex drying and wetting processes in capillary porous materials. On the experimental side, drying measurements were performed in quasi-two-dimensional single and dual cells formed by monodisperse spherical glass beads sandwiched between glass plates. The optical shadowscopy imaging technique and image processing permitted to visualize the time-dependent phase distributions as well as the drying kinetics. It has been observed in a single drying cell that the drying rate typically exhibits a transition from a high and almost constant evaporation rate sustained by the capillary liquid flow (first drying period) to a lower rate when the vapor diffusion is dominant (second drying period). During the first drying period, continuous liquid pathways connect the liquid region to the surface of the medium and thus sustain a high evaporation rate. Most experiments exhibit a first drying period down to extremely low "apparent" saturations, which is probably due to film flow. Structural effects can therefore only be seen in the phase distributions. In a dual drying cell that is divided into a hydrophobic region and a hydrophilic region, the hydrophobic region dries out first, supplying the hydrophilic region with liquid, so that the hydrophilic region stays fully saturated until the hydrophobic region is completely dry. Likewise, capillary pressure differences make the large particles supply the small ones with liquid. Thus changing the wetting property of the solid surface (hydrophilic-hydrophobic) has a similar effect as changing the pore size (small-large). In fact, experiments with such simplified packed beds are use-

ful in understanding the drying kinetics of general particle packings at the pore scale.

Other model systems used in our studies were transparent micromodels made of PDMS or silicon-glass materials. Three different PDMS micromodels were employed to conduct drying and two-phase flow experiments (i.e. drainage and imbibition), while a silicon-glass micromodel was utilized for wetting experiments. Two-dimensional images were optically acquired from the top cover of the micromodels. The small size (few centimeters) of the PDMS micromodels allowed to track the fluid displacement process in every single pore. Experiments revealed that a sharp geometrical expansion at a pore cross-section plays a decisive role in the dynamics of the pore invasion by a fluid. When a meniscus reaches the cross section between pores it pines first until the pressure across the meniscus increases to a critical value. This phenomenon is referred to as the capillary valve effect. As a result of this effect, the burst and merge events are recognized that can have a consequence on the phase distribution. When pore invasions are dominated by burst events, both the drainage and imbibition experiments show a capillary fingering pattern. Otherwise, a stable flow pattern is expected. By tracking the total liquid volume penetrated into the silica micromodel as a function of time it was possible to determine the overall wetting kinetics. The transient behavior of the advancing liquid front in this micromodel follows the classical Lucas-Washburn law.

The three-dimensional microstructure of the liquid phase in a drying particle bed packed with spherical glass beads was characterized using in situ X-ray microtomography. The results clearly show that even at low saturation, the liquid phase remains connected to the packing surface through networks of liquid rings formed at the mutual contact points between particles. As a result, the impact of capillary rings on the constant rate period is significant. Similar experiments were conducted with loose packings of sintered glass beads. A major pore-scale phenomenon of capillary pumping liquid from large pores to small pores was clearly captured in the X-ray tomograms. Moreover, porosity profiles and pore size distributions of real fibrous substrates were determined from the X-ray images. Such thin porous materials were comprised of multiple layers with distinct pore structures.

On the theoretical side, the focus was laid on discrete pore network models, in which the capillary fluid action takes a central position. The basic pore network model for drying was extended by incorporating new physical effects, of which the capillary ring effect and the capillary valve effect were observed experimentally. Three-dimensional pore network simulations conducted in the presence of capillary rings resulted in an extended first period of drying and uniform saturation profiles. These predictions seem to be consistent with

existing experimental knowledge. Pore network models that account for the capillary valve effect were also developed that can simulate situations of slow drying, drying with gas purging, and capillary-dominated two-phase flow. A better agreement between the pore network simulations and the microfluidic experiments was observed when the capillary valve effect was accounted for. The pore network models were also extended by pore condensation, as well as by the transport and accumulation of a solute. Accounting for the thermal effect enabled us to study the impact of heat load on the heat and mass transfer inside a capillary porous wick. An inflation and deflation of the vapor region occurs when the heat load increases, resulting in a time-variation of the effective heat transfer coefficient of the porous wick. Both the thermal effect and the condensation of vapor in pores were incorporated into a pore network model to simulate the superheated steam drying process, for the first time in a discrete way. Pore network modeling of solute transport and subsequent solid formation was studied with the goal of understanding the impacts of process conditions and pore structure on the distribution of a solute component after the impregnation-drying process. Simulation results show that slow drying leads to solute accumulation at the medium surface and a low solid loading in the interior due to the transport of solute to the surface by capillary action during a constant rate period. On the other hand, fast drying results in less surface accumulation and a higher solid loading in the interior because of an early and fast recession of the drying front.

In addition to drying, the wetting process was also described with a pore network model that takes into account pore emptying and filling as well as the separation of the liquid into clusters under the effect of viscous capillary flow. The validation of this pore network model was achieved by considering a set of data which was obtained from the silicon-glass micromodel experiments. An effort was then made to put the pore network simulations in relation to the results of the continuum models, namely the Lucas-Washburn law and the Richards equation. Moreover, an interesting example of the use of pore network models for wetting with technical application was presented. This example refers to the simulations of liquid penetration and subsequent redistribution in wet wipes.

A notable pore network model was developed that combines the wetting and drying algorithms. This model is capable of mimicking the process of spray agglomeration of porous particles in a fluidized bed. With this model, the time required for a droplet of binder liquid to disappear from the particle surface by drying or capillary suction is calculated. The prediction of this time is important for the success of the agglomeration process. Essentially this time must be in the right proportion to the typical collision interval. Furthermore, the pore network model of wetting-drying was combined with

a solute, so that the impregnation process of porous solid structures was simulated.

The pore network models presented here can contribute not only to a better understanding of a process, but they can also be used for the purpose of optimizing pore structures, process conditions, or even formulation recipes. On the other hand, between pore network simulations and product level there are often several orders of magnitude and thus the price to be paid for the simulations is quite demanding. Therefore, under certain conditions, continuum models still keep their validity. The issue however is their time-dependent effective parameters that often need to be determined a priori.

In this thesis methods were employed to compute the parameters from representative pore network simulations, which serve as numerical experiments. The key advantage of such methods over experiments is that everything can be controlled and everything is observable in the pore network simulations. Regarding the drying of capillary porous media, the computed (non-unique) moisture diffusivity is characterized by a minimum corresponding to the transition between liquid and vapor transport mechanisms, which supports existing interpretations. Also, the pore network drying simulations of a capillary porous medium indicate a significant non-local equilibrium effect, that is, the average vapor pressure deviation from the saturated vapor pressure when the saturation is sufficiently low in the averaging volume. It was noted that the occurrence of this effect has nothing to do with adsorption-desorption phenomena or the Kelvin effect since neither adsorption-desorption phenomena nor Kelvin effect are accounted for in the pore network simulations. Moreover, the edge effect was realized, which refers to a significant variation of the saturation in a thin layer adjacent to the porous medium surface.

The velocity field of the liquid phase was also studied by exploiting pore network simulations. The instantaneous volume-averaged velocity field in the vertical direction results in step profiles, whereas a simple mass balance in the continuum framework leads to a linear variation of the vertical velocity profile. Another key issue in the modeling of drying processes was also addressed, which is the mass exchange between the porous medium and the adjacent external air. Contrary to previous models and analyses, the pore network simulations of drying revealed that not only wet patches but also dry patches contribute to the total mass flux which leaves the porous medium. The statistical and topological properties of surface clusters (dried or still wet) have been analyzed by means of pore network simulations.

Finally, the moisture transport coefficient of the Richards equation was computed from quasi-static pore network simulations and through an inverse method. The Richards equation was then solved with the coefficient obtained

from both methods. Its prediction quality was thus assessed by pore network simulations. However, the way to full equivalence of discrete and continuum models for both drying and wetting still seems to be long.

5.2 Future Research Directions

In this thesis, based on a combination of discrete and continuum models and experiments, important progress has been made in the description of drying and wetting of capillary porous materials. There are however several open questions to be addressed and challenging aspects to be further looked upon by future research.

- One prominent research direction shall be to investigate further the role and significance of secondary capillary structures (e.g. corner liquid films and capillary liquid rings) in drying of capillary porous materials. For this purpose, gravimetric drying experiments with particle packings shall provide information regarding the impact of these structures on drying. Moreover, X-ray imaging of such model systems shall enable the characterization of the three-dimensional morphology (i.e. shape and connectivity) of the secondary capillary structures. In this way, it would be possible to study how these structures are set by the pore-scale geometry and material properties, and they can be modified by variations in pore geometry or surface properties of the particles. Also, the distance over which these structures can form connected liquid pathways shall be determined. A sophisticated and challenging version of these experiments would be to account for non-isothermal conditions. On the basis of such experiments, drying situations shall be defined where the secondary capillary structures would transform from discontinuous into continuous. It would also be interesting to carry out these experiments in the presence of a salt solution. The formation and distribution of salt crystallization spots shall thus be used as a physical signature of the drying process, especially regarding the impact of the secondary capillary structures which evolve during drying.

- The drying pore network model with capillary liquid rings disregards friction and non-isothermal effects. Therefore, this model can describe only slow, and thus long, drying of a relatively thin porous medium. These effects shall be incorporated into a pore network model in order to fully describe all possible situations of drying.

- The macroscopic parameters of the conventional continuum models have been determined from volume-averaged data. So far simulations have been conducted with relatively small pore networks, which makes the representativeness of this data questionable. Therefore, a daunting research direction shall be to develop high-performance computing codes in order to run simulations over significantly large pore networks. Such brute-force simulations shall enable us to quantify the stochastic nature of data, increase the confidence in averages, and determine the macroscopic parameters for a wide range of process conditions and for various pore structures.

- The existing continuum models shall be extended in order to take into account the non-local equilibrium effect, the edge effect, the secondary capillary structures as well as various morphological descriptors. In this way, new and superior continuum models shall be developed.

- The wetting pore network model is still immature, as it accounts for only viscous capillary flow of liquid. Therefore, this model shall be extended by allowing for trapping of the non-wetting phase, pressure gradient in the gas phase, velocity dependence and hysteresis (advancing/receding liquid) of the contact angle, etc.

- The pore network model of impregnation-drying shall be extended to account for multiple impregnation-drying cycles. Such an extension shall certainly broaden the technical applications of this pore network model. For instance, it shall be used to design tablets with customizable content of active pharmaceutical ingredients.

- Since the tools to extract irregular pore networks from complementary particle networks are available in relevant literature, it shall be a promising research direction to investigate the drying and wetting of real aggregate materials with a more or less broad distribution of particle diameters.

Appendix A

Publications Appended

[A] Kharaghani A., Kirsch C., Metzger T., Tsotsas E. *Liquid distribution and structural changes during convective drying of gels.* pp. 93-112. M. Kind, W. Peukert, H. Rehage, H. Schuchmann (Eds.). Colloid Process Engineering, Springer, 2015.

[B] Kharaghani A., Anyamene D., Tsotsas E. *Direct imaging of convective drying process for single and dual cells of two-dimensional particle packings.* The 18th International Drying Symposium (IDS), 11-15 November 2012, Xiamen, China.

[C] Wu R., Kharaghani A., Tsotsas E. *Two-phase flow with capillary valve effect in porous media.* Chemical Engineering Science 139 (2016) 241-248.

[D] Wu R., Kharaghani A., Tsotsas E. *Capillary valve effect during slow drying of porous media.* International Journal of Heat and Mass Transfer 94 (2016) 81-86.

[E] Wu R., Zhao C.Y., Tsotsas E., Kharaghani A. *Convective drying of thin hydrophobic porous media.* International Journal of Heat and Mass Transfer 112, (2017) 630-642.

[F] Sun Y., Kharaghani A., Tsotsas E. *Micro-model experiments and pore network simulations of liquid imbibition in porous media.* Chemical Engineering Science 150 (2016) 41-53.

[G] Sun Y., Song H., Kharaghani A., Tsotsas E. *Pore-scale simulation and experiment of liquid imbibition in capillary porous media.* The 15th Forschungskolloquium am Fraunhofer, 18 October 2013, Magdeburg, Germany.

[H] Wang Y.J., Kharaghani A., Metzger T., Tsotsas E. *Pore network drying model for particle aggregates: Assessment by X-ray microtomography.* Drying Technology 30 (2012) 1800-1809.

[I] Wang Y.J., Kharaghani A., Tsotsas E. *Pore-scale visualization and simulation of liquid films for drying particle packing.* The 4th European Drying Conference (EuroDrying), 2-4 October 2013, Paris, France.

[J] Sun Y., Kharaghani A., Metzger T., Müller J., Tsotsas E. *Lotion distribution in wet wipes investigated by pore network simulation and X-ray micro tomography.* Transport in Porous Media 107 (2015) 449-468.

[K] Wu R., Kharaghani A., Tsotsas E. *Convective drying in porous media bounded with a gas purge channel.* The 16th Forschungskolloquium am Fraunhofer, 14 November 2014, Magdeburg, Germany.

[L] Wang Y.J., Mahmood H.T., Kharaghani A., Tsotsas E. *Visualization and modeling of liquid film rings observed during drying of particulate packings.* The 19th International Drying Symposium (IDS), 24-27 August 2014, Lyon, Paris.

[M] Le K.H., Kharaghani A., Kirsch C., Tsotsas E. *Pore network simulations of heat and mass transfer inside the porous wick of loop heat pipe evaporators.* Transport in Porous Media 114(3) (2016) 623-648.

[N] Le K.H., Kharaghani A., Kirsch C., Tsotsas E. *Discrete pore network modeling of superheated steam drying.* Drying Technology 35(13) (2017) 1584-1601.

[O] Rahimi A., Kharaghani A. Metzger T., Tsotsas E. *Pore network model for drying of salt solutions: Solute migration and crystallization.* The 1st Nordic Baltic Drying Conference (NBDC), 17-19 June 2015, Gdansk, Poland.

[P] Rahimi A., Kharaghani A. Metzger T., Tsotsas E. *Pore network simulations of salt crystallization in drying porous media.* The 5th European Drying Conference (EuroDrying), 21-23 October 2015, Budapest, Hungry.

[Q] Sun Y., Kharaghani A., Tsotsas E. *Liquid imbibition in capillary porous media: Pore network simulation and micro-model experiment.* The 5th International Conference on Porous Media and Annual Meeting, 21-24 May 2013, Prague, Czech Republic.

[R] Rahimi A., Metzger T., Kharaghani A., Tsotsas E. *Interaction of droplets with porous structures: Pore network simulation of wetting and drying.* Drying Technology 34(9) (2016) 1129-1140.

[S] Rahimi A., Kharaghani A. Metzger T., Tsotsas E. *Pore network modeling of a salt solution droplet on a porous substrate: Imbibition, evaporation, and crystallization.* The 20th International Drying Symposium (IDS), 7-10 August 2016, Gifu, Japan.

[T] Moghaddam A.A., Prat M., Tsotsas E., Kharaghani A. *Evaporation in capillary porous media at the perfect piston-like invasion limit: Evidence of non-local equilibrium effects.* Water Resource Research 53(12) (2017) 10433-10449.

[U] Jabbari Y., Tsotsas E., Kirsch C., Kharaghani A. *Determination of the moisture transport coefficient from pore network simulations of spontaneous imbibition in capillary porous media.* Chemical Engineering Science 207(2) (2019) 600-610.

[V] Moghaddam A.A., Kharaghani A., Tsotsas E., Prat M. *Kinematics in a slowly drying porous medium: Reconciliation of pore network simulations and continuum modeling.* Physics of Fluids 29 (2017) 022102.

[W] Moghaddam A.A., Kharaghani A., Tsotsas E., Prat M. *A pore network study of evaporation from the surface of a drying non-hygroscopic porous medium.* AIChE Journal 64(4) (2018) 1435-1447.

A.1 Other Selected Own Publications

[a] Kharaghani A., Kirsch C., Metzger T., Tsotsas E. *Micro-scale fluid model for drying of highly particle aggregates.* Computers and Chemical Engineering 52 (2013) 46-54.

[b] Pashminehazar R., Kharaghani A., Tsotsas E. *Three dimensional characterization of morphology and internal structure of soft material agglomerates produced in spray fluidized bed by X-ray tomography.* Powder Technology 300 (2016) 46-60.

[c] Pashminehazar R., Ahmed S.J., Kharaghani A., Tsotsas E. *Spatial morphology of maltodextrin agglomerates from X-ray microtomographic data: Real structure evaluation vs. spherical primary particle model.* Powder Technology 331 (2018) 204-217.

[d] Pashminehazar R., Kharaghani A., Tsotsas E. *Determination of fractal dimension and prefactor of agglomerates with irregular structure.* Powder Technology 343 (2019) 765-774.

[e] Á. Calín-Sánchez, A. Kharaghani, K. Lech, A. Figiel, Á.A. Carbonell-Barrachina, E. Tsotsas. *Drying kinetics and microstructural and sensory properties of black chokeberry (Aronia melanocarpa) as affected by drying method.* Food Bioprocess Technology 8 (2015) 63-74.

[f] Szadzińska J., Łechtańska J., Pashiminehazar R., Kharaghani A., Tsotsas E. *Microwave- and ultrasound-assisted convective drying of raspberries: Drying kinetics and microstructural changes.* Drying Technology 37(1) (2019) 1-12.

[g] Szadzińska J., Łechtańska J., Pashiminehazar R., Kharaghani A. *Non-stationary convective drying of raspberries, assisted by microwaves and ultrasound.* Drying Technology 37(1) (2019) 988-1001.

[h] Szadzińska J., Mierzwa D., PawŁowski A., Musielak G., Pashiminehazar R., Kharaghani A. *Ultrasound- and microwave-assisted intermittent drying of red beetroot.* Drying Technology 38(1-2) (2020) 93-107.

[i] S. Khalloufi, A. Kharaghani, C. Almeida-Rivera, J. Nijsse, G. van Dalen, E. Tsotsas. *Monitoring of initial porosity and new pores formation during drying: A scientific debate and a technical challenge.* Trends in Food Science & Technology 45 (2015) 179-186.

[j] Shamaei S., Kharaghani A., Seiiedlou S.S., Aghbashlo M., Sondej F., Tsotsas E. *Drying behavior and locking point of single droplets containing functional oil.* Advanced Powder Technology 27 (2016) 1750-1760.

[k] Shamaei S., Seiiedlou S.S., Aghbashlo M., Tsotsas E., Kharaghani A. *Microencapsulation of walnut oil by spray drying: Effects of wall material and drying conditions on physicochemical properties of microcapsules.* Innovative Food Science and Emerging Technologies 39 (2017) 101-112.

[l] Jaskulski M., Kharaghani A., Tsotsas E. *Encapsulation methods: Spray drying, spray chilling and spray cooling.* CRC Press (2017).

[m] Gouaou I., Shamaei S., Salah Koutchoukali M., Tsotsas E., Kharaghani A. *Impact of operating conditions on a single droplet and spray drying of hydroxypropylated pea starch: Process performance and final powder properties.* Asia-Pacific Journal of Chemical Engineering 14(1) (2019) e2268.

Bibliography

[1] Geoffroy S., Prat M. *A review of drying theory and modeling approaches.* J.M.P.Q. Delgado (ed.), Drying and wetting of building materials and components, Building Pathology and Rehabilitation 4, 2014.

[2] Prat M., Agaesse T. *Thin porous media.* K. Vafai (ed.), Handbook of porous media, 3rd Edition, CRC Press, 2015.

[3] Krischer O. *Die wissenschaftlichen Grundlagen der Trocknungstechnik.* Springer, Berlin, 1963.

[4] Krischer O., Kast W. *Trocknungstechnik: Die wissenschaftlichen Grundlagen der Trocknungstechnik.* Springer, New York, 1993.

[5] Tsotsas E., Metzger T., Gnielinski V., Schlünder E.U. *Drying of solid materials.* Wiley-VCH, Weinheim, 2012.

[6] Gupta S., Huinink H.P., Prat M., Pel L., Kopinga K. *Paradoxical drying of a red-clay brick due to salt crystallization.* Chemical Engineering Science 109 (2014) 204-211.

[7] van Meel D.A. *Adiabatic convection batch drying with recirculation of air.* Chemical Engineering Science 9 (1958) 36-44.

[8] Suherman M., Peglow M., Tsotsas E. *On the applicability of normalization for drying kinetics.* Drying Technology 26 (2008) 90-96.

[9] Whitaker S. *Simultaneous heat, mass and momentum transfer in porous media: A theory of drying.* Advances in Heat Transfer 13 (1977) 119-203.

[10] Whitaker S. *Coupled transport in multiphase systems: A theory of drying.* Advances in Heat Transfer 13 (1998) 1-103.

[11] Perré P., Turner I.W. *A 3-D version of TransPore: A comprehensive heat and mass transfer computational model for simulating the drying*

of porous media. International Journal of Heat and Mass Transfer 42 (1999) 4501-4521.

[12] Vu T.H. *Influence of pore size distribution on drying behavior of porous media by continuous model.* PhD thesis, Otto-von-Guericke-Universität Magdeburg, Germany, 2006.

[13] Kohout M., Grof Z., Štěpńek F. *Pore-scale modelling and tomographic visualisation of drying in granular media.* Journal of Colloid Interface Science 299 (2006) 342-351.

[14] Philip J.R., De Vries D. A. *Moisture movement in porous materials under temperature gradients.* Transactions of American Geophysical Union 38(2) (1957), 222-232.

[15] Luikov A.V. *Heat and mass transfer in capillary-porous bodies.* 1st English Edition, Pergamon, Oxford, 1966.

[16] Luikov A.V. *Systems of differential equations of heat and mass transfer in capillary-porous bodies (review).* International Journal of Heat and Mass Transfer 18(1) (1975) 1-14.

[17] Whitaker S. *The method of volume averaging.* Springer, 1999.

[18] Plumb O.A. *Transport phenomena in porous media: Modeling the drying process.* K. Vafai (ed.), Handbook of Porous Media, M. Dekker, 2000.

[19] Lenormand R., Touboul E., Zarcone C. *Numerical models and experiments on immiscible displacements in porous media.* Journal of Fluid Mechanics 189 (1988) 165-187.

[20] Shaw T.M. *Drying as an immiscible displacement process with fluid counterflow.* Physical Review Letter 59 (1987) 1671-1674.

[21] Tsimpanogiannis I.N., Yortsos Y., Poulou S., Kanellopoulos N., Stubos A.K. *Scaling theory of drying in porous media.* Physical Review E 59 (1999) 4353-4365.

[22] Prat M. *Percolation model of drying under isothermal conditions.* International Journal of Multiphase Flow 46 (1993) 691-704.

[23] Prat M., Bouleux F. *Drying of capillary porous media with a stabilized front in two dimensions.* Physical Review E Statistical Physics Plasmas Fluids and Related Interdisciplinary Topics 60 (1999) 5647-5656.

[24] Laurindo J.B., Prat M. *Modeling of drying in capillary-porous media: a discrete approach.* Drying Technology 16 (1998) 1769-1787.

[25] Huinink H.P., Pel L., Michels M.A.J., Prat M. *Drying processes in the presence of temperature gradients, pore scale modeling.* The European Physical Journal E 9 (2002) 487-498.

[26] Prat M. *On the influence of pore shape, contact angle and film flows on drying of capillary porous media.* International Journal of Heat and Mass Transfer 50 (2007) 1455-1468.

[27] Yiotis A.G., Stubos A.K., Boudouvis A.G., Yortsos Y.C. *A 2-D pore network model of the drying of single-component liquids in porous media.* Advances in Water Resources 24 (2001) 439-460.

[28] Metzger T., Irawan A., Tsotsas E. *Influence of pore structure on drying kinetics: A pore network study.* AIChE Journal 53 (2007) 3029-3041.

[29] Metzger T., Irawan A., Tsotsas E. *Isothermal drying of pore networks: Influence of friction for different pore structures.* Drying Technology 25 (2007) 49-57.

[30] Surasani V.K., Metzger T., Tsotsas E. *Consideration of heat transfer in pore network modeling of convective drying.* International Journal of Heat and Mass Transfer 51 (2008) 2506-2518.

[31] Kharaghani A. Metzger T., Tsotsas E. *A proposal for discrete modeling of mechanical effects during drying, combining pore networks with DEM.* AIChE Journal 57(4) (2011) 872-885.

[32] Dullien F.A.L. *Porous media: Fluid Transport and pore structure.* 2nd Edition, Academic Press, the University of Michigan, 1979.

[33] Sahimi M. *Flow and transport in porous media and fractured rock: From classical methods to modern approaches.* 2nd Edition, WILEY-VCH, Weinheim, 2011.

[34] Hamraoui A., Nylander T. *Analytical approach for the Lucas-Washburn equation.* Journal of Colloidal and Interface Science 250 (2002) 415-421.

[35] Whitaker S. *Advances in theory of fluid motion in porous media.* Industrial and Engineering Chemistry 61 (1969) 14-28.

[36] Descamps F. *Continuum and discrete modelling of isothermal water and air flow in porous media.* PhD thesis, KU Leuven, Belgium, 1996.

[37] Martic G., Gentner F., Seveno D., Coulon D., De Coninck J., Blake T.D. *A molecular dynamics simulation of capillary imbibition.* Langmuir 18 (2002) 7971-7976.

[38] Wang X., Xiao S., Zhang Z., He J. *Effect of nanoparticles on spontaneous imbibition of water into ultraconfined reservoir capillary by molecular dynamics simulation.* Energies 10 (2017) 506-520.

[39] Ahrenholz B., Tölke J., Lehmann P., Peters A., Kaestner A., Krafczyk M., Durner W. *Prediction of capillary hysteresis in a porous material using lattice-Boltzmann methods and comparison to experimental data and a morphological pore network model.* Advances in Water Resources 31 (2008) 1151-1173.

[40] Arabjamaloei R., Ruth D. *Numerical study of inertial effects on permeability of porous media utilizing the Lattice Boltzmann Method.* Journal of Natural Gas Science and Engineering 44 (2017) 22-36.

[41] Zheng J., Chen Z., Xie C., Wang Z., Lei Z., Ju Y., Wang M. *Characterization of spontaneous imbibition kinetics in irregular channels by mesoscopic modeling.* Computers & Fluids 168 (2018) 21-31.

[42] Yin X., Zarikos I., Karadimitriou N.K., Raoof A., Hassanizadeh S.M. *Direct simulations of two-phase flow experiments of different geometry complexities using Volume-of-Fluid (VOF) method.* Chemical Engineering Science 195 (2019) 820-827.

[43] Ashari A., Vahedi Tafreshi H. *A two-scale modeling of motion-induced fluid release from thin fibrous porous media.* Chemical Engineering Science 64 (2009) 2067-2075.

[44] Zarandi F., Pillai K.M. *Spontaneous imbibition of liquid in glass fiber wicks, Part II: Validation of a diffuse-front model.* AIChE Journal 64 (2018) 306-315.

[45] Blunt M.J., Jackson M.D., Piri M., Valvatne P.H. *Detailed physics, predictive capabilities and macroscopic consequences for pore-network models of multiphase flow.* Advances in Water Resources 25 (2002) 1069-1089.

[46] Bell J.M., Cameron F.K. *The flow of liquid through capillary spaces.* The Journal of Physical Chemistry 10(8) (1905) 658-674.

[47] Lucas R. *Rate of capillary ascension of liquids.* Kolloid Z 23 (1918) 15-22.

[48] Washburn E.W. *The dynamics of capillary flow.* Physics Review 17(3) (1921) 273-283.

[49] Gruener S., Huber P. *Imbibition in mesoporous silica: Rheological concepts and experiments on water and a liquid crystal.* Journal of Physics: Condensed Matter 23(18) (2011) 184109.

[50] Cai J., Perfect E., Cheng C.L., Hu X. *Generalized modeling of spontaneous imbibition based on Hagen–Poiseuille flow in tortuous capillaries with variably shaped apertures.* Langmuir 30(18) (2014) 5142-5151.

[51] Li K., Zhang D., Bian H., Meng C. Yang Y. *Criteria for applying the Lucas-Washburn law.* Scientific Reports 5 (2015) 14085.

[52] Suo S., Liu M., Gan Y. *Modelling imbibition processes in heterogeneous porous media.* Transport in Porous Media 126 (2019) 615-631.

[53] Richards L.A. *Capillary conduction of liquids through porous mediums.* Physics 1 (1931) 318-333.

[54] Fatt I. *The network model of porous media.* AIME Petroleum Transactions 207 (1956) 144-181.

[55] Thompson K.E. *Pore-scale modeling of fluid transport in disordered fibrous materials.* AIChE Journal 48 (2002) 1369-1389.

[56] Bazylak A., Berejnov V., Markicevic B., Sinton D., Djilali N. *Numerical and microfluidic pore networks: Towards designs for directed water transport in GDLs.* Electrochimica Acta 53(26) (2008) 7630-7637.

[57] Jerauld G.R., Salter S.J. *The effect of pore-structure on hysteresis in relative permeability and capillary pressure: Pore level modeling.* Transport in Porous Media 5 (1990) 103-151.

[58] Joekar Niasar V., Hassanizadeh S.M., Pyrak-Nolte L.J., Berentsen C. *Simulating drainage and imbibition experiments in a high-porosity micromodel using an unstructured pore network model.* Water Resources Research 45 (2009) W02430.

[59] Raoof A., Hassanizadeh S.M. *A new formulation for pore-network modeling of two-phase flow.* Water Resources Research 48 (2012) W01514.

[60] Gruener S., Sadjadi Z., Hermes H.E., Kityk A. V., Knorr K., Egelhaaf S.U., Rieger H., Huber P. *Anomalous front broadening during spontaneous imbibition in a matrix with elongated pores.* Proceedings of the National Academy of Sciences 109 (2012) 10245-10250.

[61] Valvatne P.H., Blunt M.J. *Predictive pore-scale modeling of two-phase flow in mixed wet media.* Water Resources Research 40 (2004) W07406.

[62] Mason G., Morrow N.R. *Developments in spontaneous imbibition and possibilities for future work.* Journal of Petroleum Science and Engineering 110 (2013) 268-293.

[63] Sun Y. *Liquid imbibition in porous media investigated by pore network models and pore-scale experiments.* PhD thesis, Otto-von-Guericke-Universität Magdeburg, Germany, 2014.

[64] Bear J., Corapcioglu M.Y. *Advances in transport phenomena in porous media.* Martinus Nijhoff Publishers, Lancaster, 1987.

[65] McHale G., Newton M.I. *Frenkel's method and the dynamic wetting of heterogeneous planar surfaces.* Colloids and Surfaces A 206 (2002) 193-201.

[66] Adamson A.W. *Physical chemistry of surfaces.* 5th Edition, WILEY-VCH, New York, 1990.

[67] Berg J. *Wettability.* 1st Edition, CRC Press, New York, 1993.

[68] de Gennes P.G., Brochard-Wyart F., Quere D. *Capillarity and wetting Phenomena: Drops, Bubbles, Pearls, Waves.* 1st Edition, Springer, New York, 2013.

[69] Adamson A.W., Gast A.P. *Physical chemistry of surfaces.* 6th Edition, Wiley-Blackwell, New York, 1997.

[70] Bell L.N., Labuza T.P. *Practical aspects of moisture sorption isotherm measurement and use.* 2nd Edition, AACC Eagan Press, Eagan, 2000.

[71] Chartrand R. *Numerical differentiation of noisy, non-smooth data.* ISRN Applied Mathematics 2011 (2011) 11 pages.

[72] Kharaghani A. Metzger T., Tsotsas E. *An irregular pore network model for convective drying and resulting damage of particle aggregates.* Chemical Engineering Science 75 (2012) 267-278.

[73] Vorhauer N., Wang Y.J., Kharaghani A., Tsotsas E., Prat M. *Drying with formation of capillary rings in a model porous medium.* Transport in Porous Media 110 (2015) 197-223.

[74] Metzger T., Tsotsas E. *Network models for capillary porous media: Application to drying technology.* Chemie Ingenieur Technik 6 (2010) 869-879.

[75] Anyamene D. *Direct imaging of pore-scale phenomena during drying of 2-D particle aggregates.* MSc thesis, Otto-von-Guericke-Universität Magdeburg, Germany, 2011.

[76] Karadimitriou N.K., Hassanizadeh S.M. *A review of micromodels and their use in two-phase flow studies.* Vadose Zone Journal 11(3) (2012) vzj2011.0072.

[77] Li X. *Fabrication of PDMS-based microfluidic model and visualization experiments.* MSc thesis, Otto-von-Guericke-Universität Magdeburg, Germany, 2015.

[78] Mahmud W.M., Nguyen V.H. *Effects of snap-off in imbibition in porous media with different spatial correlations.* Transport in Porous Media 64 (2006) 279-300.

[79] Song H. *Pore-scale simulation and experiment of liquid imbibition in porous media.* MSc thesis, Otto-von-Guericke-Universität Magdeburg, Germany, 2013.

[80] Pel L. *Moisture transport in porous building materials.* PhD thesis, Eindhoven University of Technology, The Netherlands, 1995.

[81] Shokri N., Lehmann P., Or D. *Liquid-phase continuity and solute concentration dynamics during evaporation from porous media: Pore-scale processes near vaporization surface.* Physical Review E 81 (2010) 046308.

[82] Pashminehazar R. *Micro-structure of particles produced by fluidized bed agglomeration of soft materials.* PhD thesis, Otto-von-Guericke-Universität Magdeburg, Germany, 2019.

[83] Scherer G.W. *Stress from crystallization of salt.* Cement and Concrete Research 34 (2004), 1613-1624.

[84] Scheel M., Seemann R., Brinkmann M., Michiel M.D., Sheppard A., Herminghaus S. *Liquid distribution and cohesion in wet granular assemblies*

beyond the capillary bridge regime. Journal of Physics Condensed Matter 20(2008) 494236-7.

[85] Brinker C.J., Scherer G.W. *Sol-Gel Science.* Academic Press, New York, 1990.

[86] Pel L., Huinink H., Kopinga K. *Ion Transport and crystallization in inorganic building material as studied by nuclear magnetic resonance.* Applied Physics Letters 81 (2002), 2893-2895.

[87] Sghaier N., Prat M. *Effect of efflorescence formation on drying kinetics of porous media.* Transport in Porous Media 80 (2009), 441-454.

[88] Rad N.M., Shokri N. *Nonlinear effects of salt concentrations on evaporation from porous media.* Geophysical Research Letters 39 (2012) L04403.

[89] Eloukabi H., Sghaier N., Nassrallah B., Prat M. *Experimental study of the effect of sodium chloride on drying of porous media: The crusty-patchy efflorescence transition.* International Journal of Heat and Mass Transfer 56 (2013) 80-93.

[90] Börnhorst M., Walzel P., Rahimi A., Kharaghani A., Tsotsas E., Nestle N., Besser A., Kleine Jäger F., Metzger T. Influence of pore structure and impregnation-drying conditions on the solid distribution in porous support materials. Drying Technology 34(16) (2016) 1964-1978.

[91] Shokri N., Sahimi M. *Structure of drying fronts in three-dimensional porous media.* Physical Review E 85 (2012) 066312.

[92] Xiong Q., Baychev T.G., Jivkov A.P. *Review of pore network modeling of porous media: Experimental characterizations, network constructions and applications to reactive transport.* Journal of Contaminant Hydrology 192 (2016) 101-117.

[93] Stefan J. *über das Gleichgewicht und die Bewegung, insbesondere die Diffusion von Gasgemengen.* Sitzungsberichte der Akademie der Wissenschaften 63 (1871) 63-124.

[94] Metzger T., Irawan A., Tsotsas E. *Remarks on the paper "Extension of Hoshen-Kopelman algorithm to non-lattice environments" by A. Al-Futaisi and T.W. Patzek, Physica A 321 (2003) 665-678.* Physica A 363 (2006) 558-560.

[95] Irawan A. *Isothermal drying of pore networks: influence of pore structure on drying kinetics.* PhD Thesis, Otto-von-Guericke-Universität Magdeburg, 2006.

[96] Metzger T., Tsotsas E., Prat M. *Chapter 2: Pore network models.* In: Tsotsas E, Mujumdar AS, eds. Modern Drying Technology 1: Computational Tools at Different Scales. John Wiley & Sons, 2007, pp. 57-102.

[97] Metzger T., Tsotsas E. *Viscous stabilization of drying front: Three-dimensional pore network simulations.* Chemical Engineering Research and Design 86(7) (2008) 739-744.

[98] Zhi H. *Convective drying of porous medium with bounded gas purge channel.* MSc thesis, Otto-von-Guericke-Universität Magdeburg, Germany, 2016.

[99] Prat M. *Isothermal drying of non-hygroscopic capillary-porous materials as an invasion percolation process.* International Journal of Multiphase Flow 21 (1995) 875-892.

[100] Tsotsas E., Martin H. *Thermal conductivity of packed beds: A review.* Chemical Engineering and Processing: Process Intensification 22(1), (1987) 19-37.

[101] Mottet L., Coquard T., Prat M. *Three dimensional liquid and vapor distribution in the wick of capillary evaporators.* International Journal of Heat and Mass Transfer 83 (2015) 636-651.

[102] Nishikawara M., Nagano H., Mottet L., Prat, M. *Formation of unsaturated regions in the porous wick of a capillary evaporator.* International Journal of Heat and Mass Transfer 89 (2015) 588-595.

[103] Le K.H. *Multiscale modeling of non-isothermal fluid transport in porous media.* PhD thesis, Otto-von-Guericke-Universität Magdeburg, Germany, 2017.

[104] Plourde F., Prat M. *Pore network simulations of drying of capillary porous media: Influence of thermal gradients..* International Journal of Heat and Mass Transfer 34(8) (1991) 1975-1981.

[105] Taleghani S.T., Dadvar M. *Two dimensional pore network modeling and simulation of non-isothermal drying by the inclusion of viscous effects.* International Journal of Multiphase Flow 62 (2014) 37-44.

[106] Mujumdar A.S. *Handbook of Industrial Drying.* 4th Edition, Taylor and Francis, Hoboken, 2014.

[107] Iyota H., Nishimura N., Yoshida M., Nomura T. *Simulation of superheated steam drying considering initial condensation.* Drying Technology 19(7) (2001) 1425-1440.

[108] Eames I.W., Marr N.J., Sabir H. *The evaporation coefficient of water: A review.* International Journal of Heat and Mass Transfer 40(12) (1997) 2963-2973.

[109] Pound G.M. *Selected values of evaporation and condensation coefficients for simple substances.* Journal of Physical and Chemical Reference Data 1(1) (1972) 135-146.

[110] Hu X. *Incorporation of pore-node volume into wetting-drying pore network model.* MSc thesis, Otto-von-Guericke-Universität Magdeburg, Germany, 2015.

[111] Schoeber W. *Regular regimes in sorption processes: Calculation of drying rates and determination of concentration dependent diffusion coefficients.* PhD thesis, Eindhoven University of Technology, the Netherlands, 1976.

[112] Marchand R.G., Kumaran M.K. *Moisture diffusivity of cellulose insulation.* Journal of Thermal Insulation and Building Envelopes 17 (1994) 362-377.

[113] Pel L., Brocken H., Kopinga K. *Determination of moisture diffusivity in porous media using moisture concentration profiles.* International Journal of Heat and Mass Transfer 39(6) (1996) 1273-1280.

[114] Nowicki S.C., Davis H.T., Scriven L. *Microscopic determination of transport parameters in drying porous media.* Drying Technology 10 (1992) 925-946.

[115] Vorhauer N., Metzger T., Tsotsas E. *Extraction of effective parameters for continuous drying model from discrete pore network mode.* The 17th International Drying Symposium (IDS), 3-6 October 2010, Magdeburg, Germany.

[116] Vu H.T., Tsotsas E. *A framework and numerical solution of the drying process in porous media by using a continuous model.* International Journal of Chemical Engineering (2019) doi.org/10.1155/2019/9043670.

[117] Purcell W.R. *Capillary pressures -their measurement using mercury and the calculation of permeability therefrom.* Journal of Petroleum Technology 1 (1949) 39-48.

[118] Dernaika M.R., Kalam M.Z., Basioni M., Dawoud A., Skjaveland S.M. *Hysteresis of capillary pressure, resistivity index and relative permeability in different carbonate rock types.* Society of Petrophysicists and Well-Log Analysts 53(5) (2012) 316-332.

[119] Brooks R.H., Corey A.T. *Hydraulic properties of porous media.* Hydrology Papers, Colorado State University, 1964.

[120] van Genuchten M.T. *A closed-form equation for predicting the hydraulic conductivity of unsaturated soils.* Soil Science Society of American Journal 44 (1980) 892-898.

[121] Landeryou M., Eames I., Cottenden A. *Infiltration into inclined fibrous sheets.* Journal of Fluid Mechanics 529 (2005) 173-193.

[122] Aslannejad H., Hassanizadeh S.M., Raoof A., de Winter D.A.M., Tomozeiu N., van Genuchten M.T. *Characterizing the hydraulic properties of paper coating layer using FIB-SEM tomography and 3D pore-scale modeling.* Chemical Engineering Science 160 (2017) 275-280.

[123] Blunt M., King P. *Macroscopic parameters from simulations of pore scale flow.* Physical Review A 42(8) (1990) 4780-4787.

[124] Blunt M., King P. *Relative permeability from two- and three-dimensional pore-scale modeling.* Transport in Porous Media 6 (1991) 407-433.

[125] Reeves P.C., Celia M.A. *A functional Relationship between capillary pressure, saturation, and interfacial areas as revealed by a pore-scale network model.* Water Resource Research 32(8) (1996) 2345-2358.

[126] Joekar-Niasar V., Hassanizadeh S.M., Dahle H.K. *Non-equilibrium effects in capillarity and interfacial area in two-phase flow: Dynamic pore-network modelling.* Journal of Fluid Mechanics 655 (2010) 38-71.

[127] Li J., McDougall S.R., Sorbie K.S. *Dynamic pore-scale network model (PNM) of water imbibition in porous media.* Advances in Water Resources 107 (2017) 191-211.

[128] Umer M. *One-dimensional moisture transport coefficient of drying porous media obtained from inverse method.* MSc thesis, Otto-von-Guericke-Universität Magdeburg, Germany, 2016.

[129] Fries N. *Capillary transport processes in porous materials – experiment and model.* PhD thesis, University of Bremen, Germany, 2010.

[130] Prat M. *Recent advances in pore-scale models for drying of porous media.* Chemical Engineering Journal 86 (2002) 153-164.

[131] Huinink H.P., Pel L., Michels M.A.J. *How ions distribute in a drying porous medium: A simple model* Physics of Fluids 14(4) (2002) 1389-1395.

[132] Armstrong R.T., Berg S. *Interfacial velocities and capillary pressure gradients during Haines jumps.* Physical Review E 88 (2013) 043010.

[133] Ferrari A., Lunati I. *Inertial effects during irreversible meniscus reconfiguration in angular pores.* Advances in Water Resources 74 (2014) 1-13.

[134] Moghaddam A.A. *Parameter estimation and assessment of continuum models of drying on the basis of pore network simulations.* PhD thesis, Otto-von-Guericke-Universität Magdeburg, Germany, 2017.

[135] Valadian R. *Macroscopic parameters of drying porous media in gravity-capillary regime obtained from pore network simulations.* MSc thesis, Otto-von-Guericke-Universität Magdeburg, Germany, 2016.

[136] Guglielmini L., Gontcharov A., Aldykiewicz A.J., Stone H.A. *Drying of salt solutions in porous materials: Intermediate-time dynamics and efflorescence.* Physics of Fluids 20 (2008) 077101.

[137] Rad M.N., Shokri N., Sahimi M. *Pore-scale dynamics of salt precipitation in drying porous media.* Physical Review E 88 (2013) 032404.

[138] Desarnaud J., Derluyn H., Molari L., de Miranda S., Cnudde V., Shahidzadeh N. *Drying of salt contaminated porous media: Effect of primary and secondary nucleation.* Journal of Applied Physics 118(11) (2015) 114901.

[139] Keita E., Kodger T.E., Faure P., Rodts S., Weitz D.A., Coussot P. *Water retention against drying with soft-particle suspensions in porous media.* Physical Review E 94 (2016) 033104.

[140] Hidri F., Sghaier N., Eloukabi H., Prat M., Ben Nasrallah S. *Porous medium coffee ring effect and other factors affecting the first crystallisation time of sodium chloride at the surface of a drying porous medium.* Physics of Fluids 25(12) (2013) 127101.

[141] Lehmann P, Assouline S, Or D. *Characteristic lengths affecting evaporative drying of porous media.* Physical Review E 77(5) (2008) 056309.

[142] Shokri N., Or D. *What determines drying rates at the onset of diffusion controlled stage-2 evaporation from porous media?.* Water Resources Research 47(9) (2011) W09513.

[143] Suzuki M., Maeda S. *On the mechanism of drying of granular beds.* Journal of Chemical Engineering of Japan 1 (1968) 26-31.

[144] Schlünder, E.-U. *On the mechanism of the constant rate period and its relavance to diffusion controlled catalytic gas phase reactions.* Chemical Engineering Science 43(5) (1988) 2685-2688.

[145] Schlünder, E.-U. *Drying of porous material during the constant and the falling rate period: A critical review of existing hypotheses.* Drying Technology 22 (2004) 1517-1532.

[146] Lehmann P., Or D. *Effect of wetness patchiness on evaporation dynamics from drying porous surfaces.* Water Resources Research 49 (2013) 8250-8262.

[147] Shahraeeni E., Lehmann P., Or D. *Coupling of evaporative fluxes from drying porous surfaces with air boundary layer: Characteristics of evaporation from discrete pores.* Water Resources Research 48 (2012) W09525.

[148] Haghighi E., Shahraeeni E., Lehmann P., Or D. *Evaporation rates across a convective air boundary layer are dominated by diffusion.* Water Resources Research 49 (2013) 1602-1610.

[149] Talbi M., Prat M. *About Schlünder's model: A numerical study of evaporation from partially wet surfaces.* Drying Technology (2018).

[150] Chen P, Pei D.C.T. *A mathematical model of drying processes.* International Journal of Heat and Mass Transfer 32 (1989) 297-310.

[151] Bird R.B., Stewart W.E., Lightfoot E.N. *Transport phenomena.* John Wiley & Sons, New York, 2002.

[152] Masmoudi W., Prat M. *Heat and mass transfer between a porous medium and a parallel external flow: Application to drying of capillary porous materials.* International Journal of Heat and Mass Transfer 34 (1991) 1975-1989.

[153] Jambhekar V.A., Helmig R., Schröder N., Shokri N. *Free-flow-porous-media coupling for evaporation-driven transport and precipitation of salt.* Transport in Porous Media 110 (2015) 251-280.

[154] Xu Z., Pillai K.M. *Analyzing slow drying in a porous medium placed adjacent to laminar airflow using a pore-network model.* Numerical Heat Transfer, Part A: Applications 70 (2016) 1213-1231.